OPTICAL PROPERTIES AND ENSEMBLE CHARACTERISTICS OF SIZE PURIFIED SILICON NANOCRYSTALS

A Dissertation
Submitted to the Graduate Faculty
of the
North Dakota State University
of Agriculture and Applied Science

By

Joseph Bradley Miller

In Partial Fulfillment of the Requirements
for the Degree of
DOCTOR OF PHILOSOPHY

Major Department:
Materials and Nanotechnology

April 2014

Fargo, North Dakota

North Dakota State University
Graduate School

Title

Optical Properties and Ensemble Characteristics of Size Purified Silicon Nanocrystals

By

Joseph Bradley Miller

The Supervisory Committee certifies that this ***disquisition*** complies with North Dakota State University's regulations and meets the accepted standards for the degree of

DOCTOR OF PHILOSOPHY

SUPERVISORY COMMITTEE:

Erik Hobbie
Chair

Stuart Croll

Orven Swenson

Xinnan Wang

Approved:

4/2/2014	Erik Hobbie
Date	Department Chair

ABSTRACT

Nanotechnology is at the forefront of current scientific research and nanocrystals are being hailed as the 'artificial' atoms of the 21st century. Semiconducting silicon nanocrystals (SiNCs) are prime candidates for potential commercial applications because of silicon's already ubiquitous presence in the semiconductor industry, nontoxicity and abundance in nature. For realization of these potential applications, the properties and behavior of SiNCs need to be understood and enhanced.

In this report, some of the main SiNC synthesis schemes are discussed, including those we are currently experimenting with to create our own SiNCs and the one utilized to create the SiNCs used in this study. The underlying physics that governs the unique behavior of SiNCs is then presented. The properties of the as-produced SiNCs are determined to depend strongly on surface passivation and environment. Size purification, an important aspect of nanomaterial utilization, was successfully performed on our SiNCs though density gradient ultracentrifugation. We demonstrate that the size-purified fractions exhibit an enhanced ability for colloidal self-assembly, with better aligned nanocrystal energy levels which promotes greater photostability in close-packed films and produces a slight increase in photoluminescence (PL) quantum yield. The qualities displayed by the fractions are exploited to form SiNC clusters that exhibit photostable PL. An analysis of SiNC cluster (from individual nanocrystals to collections of more than one thousand) blinking and PL shows an improvement in their PL emitting 'on' times. Pure SiNC films and SiNC-polymer nanocomposites are created and the dependence of their PL on temperature is measured. For such nanocomposites, the coupling between the 'coffee-ring' effect and liquid-liquid phase separation is also examined for ternary mixtures of solvent, polymer and semiconducting nanocrystal. We discover that with the right SiNC-polymer concentration and polymer molecular weight, phase

separation can be supressed; we use this to build a prototype nanocomposite printing device. Finally, the nanocrystals are PEGylated and introduced into an aqueous biological environment to demonstrate their potential for use in biological labelling and sensing devices. The development of superlattice structures from monodisperse SiNC fractions and their use in solid-state lighting and solar cell applications are also explored.

ACKNOWLEDGMENTS

I would like to start by thanking Erik Hobbie. I remember first meeting Erik in the previous physics chair's office and thinking what an enthusiastic person he was. This initial impression was very accurate. Over the years of working with the Materials and Nanotechnology program head and my advisor, I have learned to appreciate his enthusiasm, motivation and extreme care for his students. His traits have been very beneficial to my studies and research, especially in those frustrating times when I just couldn't seem to get the experiment to work. It is also nice to have someone like Erik who not only wants me to be successful and happy in my research but in my personal life as well. Thanks for helping me along this journey.

I also want to thank the many people whom I have worked closely with. The first guy is Austin van Sickle or as he would say, "My partner in SiNCrime." Austin and I would often sit on opposite sides of an optical table bantering back and forth. This conversation helped the time go by and added excitement to the experimental data collection process. Oh, and Austin, my car is still as you remember it, a graveyard of McDonald's^{TM} and Burger King^{TM} bags. I want to thank Chris Moore for the many summers of lab fun together. Chris and I had many exciting Minnesota Public Radio debates while conducting research. Thanks to the other member of the group, John Harris and Matt Semler. John, you performed conductivity and etching experiments to help with my research as well as turned our lab into a quasi-garden which helped provide the oxygen I needed to write this report. Matt, you helped with blinking data measurements and silicon laser ablation. You also allowed me to join your basketball team where we proved that the 'Quantum Dots' basketball team is a legitimate threat. Lastly, I want to thank my newest co-researchers, Ahmed Elbaradei and Sam Brown. Ahmed, thanks for putting up with my 'fastidiousness' and I think it is fair to say that we are officially quantum yield masters. And Sam, thanks for teaching me some

chemistry and about the nutritiousness of Cheez-It^{TM} brand crackers.

Finally, I want to thank Loren Vanderhoff, Swathi Iyer and Scott Payne for helping with my research, Stuart Croll, Orven Swenson, Daniel Kroll, Xinnan Wang and all staff in the Physics Department for advising me on my research and career path, Damith Rosario and Bekele Gurmessa for helping make graduate school a fun experience and Rebecca Anthony and Uwe Kortshagen for supplying the nanocrystals used in this study.

DEDICATION

To my grandparents,

Bernadine Sophie Pieper

(1925-)

Eugene Henry Pieper

(1924-2007)

Gwendolyn Lorraine Miller

(1934-2010)

and

Robert Michael Miller

(1933-2013)

TABLE OF CONTENTS

LIST OF TABLES

LIST OF FIGURES

CHAPTER 1. INTRODUCTION

The unique optical and electronic properties of semiconducting nanocrystals, or zero-dimensional "quantum dots" as coined by Reed, et al. [1], have generated much intrigue and excitement since their discovery. The first evidence of these nanocrystals was published in 1981 on copper chloride (CuCl) crystals grown in a glass matrix [2]. Then in 1983, Louis Brus and others at Bell Laboratories published new findings on quantum size effects for colloidal cadmium sulfide (CdS) crystallites [3]. Nanocrystals, as their name implies, are crystals with diameters between 1-100 nanometers. The size of an individual 1-dodecene passivated SiNC is compared to a human hair, a red blood cell and a water molecule in Figure 1.

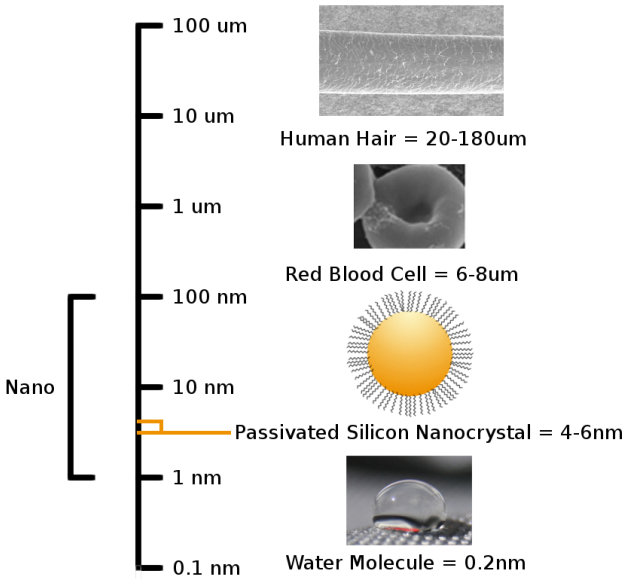

Figure 1: Comparison of the nanoscale [4–6].

The small dimensions of these nanocrystals approach the natural exciton-Bohr radius, which is the average distance from an excited electron to its corresponding hole in the bulk material. This confinement leads to an increase in the energy band gap of the material therefore modifying its optical and electronic properties which allows for visible PL (Figure 2).

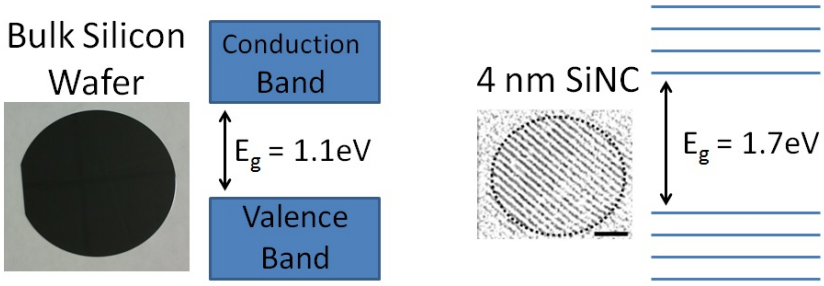

Figure 2: Band gap of a bulk silicon wafer compared to a 4 nm SiNC.

Modification of a nanocrystal's properties can be fine-tuned by simply changing its diameter and, thus, over the past decades there have been an increasing number of studies on their properties, behaviors and potential applications: particularly the metal chalcogenides [7–12]. In recent years there has been growing interest toward the use of silicon because of its abundance in nature, low toxicity [13], chemical stability [14], high mobility [15], solubility [16, 17] and ubiquity in the semiconductor industry. Figure 3 shows the increasing number of published articles related to SiNCs: from the discovery of fluorescence from porous silicon in 1990 through 2012 where the number of articles surpasses 1100.

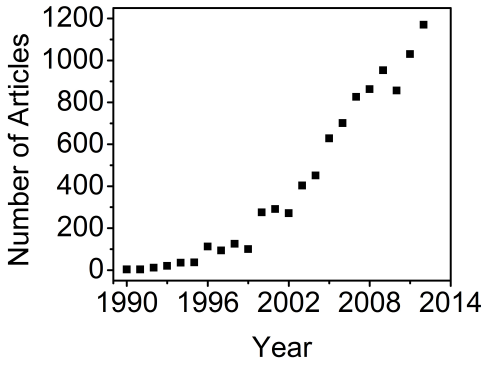

Figure 3: Number of published articles per year containing 'SiNC(s)' according to Google™ Scholar on October 10, 2013.

In many regards it appears that the 21st century is dawning as the age of nanotechnology [18]. Nanotechnology is a relatively new field which has caused an abundance of excitement in the areas of academia and research. This excitement is

spilling over into commercial industry and the general populace where nanotechnology is being portrayed in movies, television and video games. Nanotechnology and nanocrystals are not only being explored and investigated for biological purposes but have found potential application in solar panels and solid-state lighting devices such as televisions and mobile phone displays. Because of this, studying SiNCs in any form is very exciting and beneficial. One particular interest involves the relatively novel study of SiNCs for employment as a biological sensing device. The most important benefit of using silicon is its nontoxic nature. This biocompatibility coupled with the variable electronic and optical properties make SiNCs leading contenders to replace the potentiallly toxic and environmentally harmful metal chalcogenide nanocrystals.

Another essential element of biological utilization is the successful detection of light. Silicon nanocrystals can easily be produced to emit near-infrared radiation (NIR). This radiation is in an area of the electromagnetic spectrum (λ = 700-1000 nm) that is considered the 'biological window' due to the low autofluorescence and scattering by biological tissue resulting in a high signal to noise ratio. Radiation in this range can penetrate 2-5 cm into a sample [19], and Cheng et al. pointed out that "It is expected that NIR optical imaging will make a significant impact in disease detection and staging, drug development, and treatment assessment" [20]. Because two nanocrystals with unlike diameters can have different emission but overlapping absorption, it is also possible to image multiple targets at different colors with a single excitation wavelength [21]. Another advantage over the competing current use of molecular dyes is that there is limited to no crossover between excitation and emission wavelengths which helps distinguish samples more clearly. Silicon nanocrystals also have long-lived excited states which suppress the interference signal from short-lived tissue autofluorescence. This feature, combined with those previously mentioned, allows for impressive time-gated fluorescence imaging of biological species such as the

example shown in Figure 4.

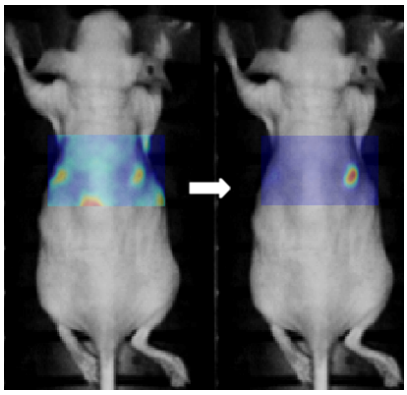

Figure 4: A mouse injected with a conventional molecular dye (left shoulder) and silicon nanoparticles (right shoulder). Time-gated fluorescence imaging was performed to show an advantage of the extended lifetime of silicon nanoparticles. The right image (18 ns after excitation pulse) shows no signal from the fast-decaying dye nor from the tissue autofluorescence near the abdomen [22].

Nanocrystals also demonstrate complex and interesting behavior including fluorescence intermittency, PL enhancement and PL activation. The usefulness of nanocrystals is highly dependent on understanding these dynamic behaviors. Modification, mitigation and enhancement of nanocrystal properties will lead to new synthesis and functionalization schemes which can then be further tuned to target specific needs [23, 24].

CHAPTER 2. NANOCRYSTAL SYNTHESIS

Since the first discovery of PL from nano-sized semiconducting crystals, many schemes have been developed to produce nanocrystals of varying size, geometries and intrinsic composition. This is all in an effort to fully realize their potential applications. Although many methods have been developed, the focus here will be on synthesis of SiNCs which has carry-over into nanocrystals made from other materials, especially carbon and germanium. Laser pyrolysis and solution based methods are currently being employed and experimented with to create SiNCs here at North Dakota State University. A plasma based synthesis scheme carried out at the University of Minnesota, however, was used to create the SiNCs used in this study.

2.1. Chemical Etching

SiNCs were first observed in porous silicon in the early 1990s. Although there are other techniques such as electroless and galvanic etching, porous silicon is often created by chemical or electrochemical etching of silicon wafers. Generally, a silicon wafer is polarized in an electrolyte containing hydrofluoric acid. The wafer begins to slowly dissolve, forming cavities that percolate the sample to produce porous silicon. The method is quite sensitive to doping, temperature, electrolyte composition and current density in the case of electroetching [25]. The formed nanocrystals can then by removed by sonication in a solvent bath or left for further study.

2.2. Plasma Enhanced Chemical Vapor Deposition

Currently, the most well established and commonly used practice of creating SiNCs is by growth of pure silicon clusters in a SiO_x matrix. This can and has been achieved through numerous different synthesis schemes including electron beam evaporation, magnetron sputtering, chemical vapor deposition (CVD) and plasma

enhanced chemical vapor deposition (PECVD). Though each scheme has its advantages, the PECVD method is fully compatible with standard silicon technology [26]. In a typical PECVD setup, silane SiH_4 and nitrous oxide N_2O are flowed through a chamber containing two parallel plate electrodes. The top electrode is attached to a supplied radio frequency power source which turns the gases into a plasma that undergoes the following reaction

$$SiH_x + N_2O \longrightarrow SiO_x + H_2 + N_2. \tag{2.1}$$

The bottom electrode is heated. By changing the source gas, radio frequency power, bottom electrode temperature and flow rate, the deposited silicon oxide film properties can be controlled. Further thermal annealing of these films allows for controlled nucleation of SiNCs.

2.3. Ion Implantation

Ion implantation is another viable method for forming SiNCs. Ion implantation requires a quite complex setup but is governed by rather simple physics. A silicon ion source is accelerated through a fixed electrostatic potential towards a magnetic mass-spectrometer which filters undesired ion species. A beam or sample scanning system then allows uniform irradiation of the sample which is contained in a special chamber. This chamber allows control of the sample position, temperature and vacuum conditions which are all essential variable parameters. Once the ions hit the sample substrate, they will penetrate a certain depth depending on their energy and the substrate composition. For silicon, the substrate is often silicon dioxide. As the ions begin to approach the supersaturation limit of the solid, they will nucleate and eventually form SiNCs [27].

2.4. Sol-Gel Pyrolysis

Optical gain in SiNCs embedded in silicon dioxide matrices has been observed and has been a hot topic since the first report of such behavior. However, many methods including ion implantation are not particularly good at making optimized Si/SiO_2 matrices for improved optical gain. These methods can be expensive, lead to broad size distributions and produce low-density Si/SiO_2 films. Another synthesis scheme that may offer a solution to some of these problems is SiNC formation by pyrolysis of sol-gel-derived precursors. This method uses one of the commercially available hybrid silicon alkoxides such as tetraethylorthosilicate with the formula $HSi(OCH_2CH_3)_3$ or $HSi(OR)_3$. In order to make the SiNC embedded ceramic material, a three step process is followed. First, the hybrid silicon alkoxide is hydrolyzed with water which substitutes the OR group with a silanol Si-OH group. Second, these species undergo condensation where they react together to form a siloxane (Si-O-Si) bonded network. Finally, pyrolysis is performed at temperatures above 1000 °C where the Si-H moieties present react to produce H_2 and Si-Si bonds. The Si-Si bonds reorganize and form SiNCs [28].

2.5. SiO_x/SiO_2 Stoichiometric Annealing

Creating monodisperse size distributions has been an up-hill battle in the case of SiNCs. One of the first synthesis methods performed to try and control SiNC size was a SiO/SiO_2 superlattice approach. This approach used molecular beam epitaxy and UV-ozone oxidation to sequentially grow precise nanometer-sized amorphous silicon layers between SiO_2 layers. However, the new standard method developed in 2002 evaporates alternating layers of SiO_x/SiO_2 where $1 \leq x \leq 2$. This is done by thermal evaporation of SiO powder at 1000 °C under high vacuum. Oxygen is added during growth to control the stoichiometry. The layers are then annealed at 1100 °C under

a nitrogen atmosphere. Nonstoichiometric oxides such as SiO_x are not stable at high temperature and decompose by a phase separation into the two stable components Si and SiO_2 [29]:

$$SiO_x \longrightarrow \frac{x}{2}SiO_2 + \left(1 - \frac{x}{2}\right) Si. \tag{2.2}$$

2.6. Laser Pyrolysis

Laser pyrolysis of silicon wafers is a procedure that has recently been explored to create SiNCs. It is a fast way to form SiNCs when size polydispersity is not a concern. We are currently conducting experiments which involve the incorporation of doped, oxide passivated SiNCs in a carbon nanotube - silicon composite solar cell in order to improve absorption and efficiency. These SiNCs are created here at North Dakota State University by ablation of a p-doped silicon wafer in ethanol or chloroform.

Another laser pyrolysis synthesis method which can be used to achieve higher size selectivity of nanocrystals was performed by Ehbrecht et al. [30]. They designed an *in-situ* way of creating SiNCs, separating them according to mass and measuring their size. A silane gas precursor with an inert carrier gas (helium) was flowed through the reaction chamber of a molecular beam machine under vacuum. A perpendicular pulsed CO_2 laser was focused on the incoming gas flow. A 0.3 mm conical nozzle perpendicular to both the radiation beam and gas flow allowed silicon clusters to flow into a lower pressure differential chamber. This differential chamber was also fitted with a chopper disk which, once synchronized with the pulsed laser, was able to control the cluster size of the silicon deposited on a substrate behind it. This is due to the variable velocity and kinetic energy of different sized silicon particles. If the sample substrate is removed, the silicon particles can travel until they reach a time-of-flight mass spectrometer (TOFMS) located after the differential chamber (Figure 5). Here the particles are ionized with a Wiley-McLaren-type ion source by

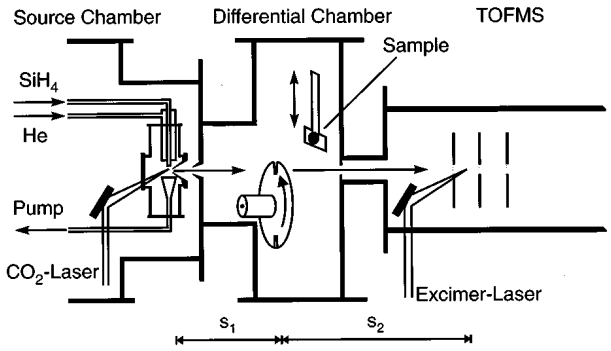

Figure 5: An experimental setup of laser pyrolysis. Reprinted figure with permission from [30]. Copyright (1997) by the American Physical Society.

radiation from an ArF excimer laser and further analyzed to determine the variance in their size distribution which ranged from 7-28 % [30].

2.7. Solution Based

Solution based methods are probably the most commercially favorable as they often cost less and are relatively easy to perform. For this study, we relied on another research group for SiNCs. However, we are now working at becoming self-reliant and creating our own nanoparticles. The first experiments were just performed at the time of writing and used a solution based method similar to the one proposed by Hessel et al. [31]. In this method, solid white hydrogen silsesquioxan (HSQ) is placed in a quartz crucible and heated under a flow of noble gas between 1100 °C and 1400 °C depending of the desired nanocrystal size. The sample is held at peak temperature for 1 hour and then cooled to room temperature. This brown/black glassy product is then ground for 20 minutes in an agate mortar and pestle until grains of 2 μm are obtained. Subsequent particle size reduction is performed by shaking for 9 hours with borosilicate glass beads in a wrist-action shaker. The $\sim$200 nm particles are then etched in a hydrofluoric and hydrochloric acid solution to liberate the SiNCs. The resulting SiNCs have a standard deviation between 10 % and 19 %.

2.8. Non-thermal Low-pressure Plasma

The SiNCs that were utilized in this study are made by plasma synthesis. This non-thermal low-pressure plasma reaction is unique when compared to previously described methods. It is a scalable process that can create SiNCs with relatively high mass yield, narrow size distributions, high purity and quantum yields near 50 %. High quantum yield is a key quality that must be achieved by SiNCs in order to make them competitive for use in optical sensing devices, solid-state lighting devices and as solar panel components. An image of the setup involved is shown in Figure 6.

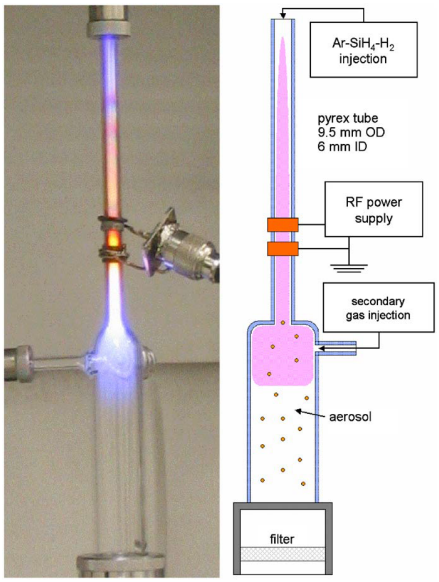

Figure 6: The non-thermal low-pressure setup from [32].

The reactor consists of a 6.3 mm inner diameter Pyrex tube which expands to a wider bottom downward from the reaction where the pressure is approximately 1.4 Torr. There is a top gas inlet which flows a mixture of argon, silane and hydrogen into the reaction chamber at rates of 50, 5-10 and 1-5 sccm, respectively. The mixture is exposed to radio frequency (13.56 MHz) power at 50 W supplied by an electrode pair which breaks down the gas into a plasma. This leads to the chemical clustering of silicon. The clusters travel through the most intense plasma zone for 2-5 ms where

they grow to a few nanometers in diameter. The newly formed SiNCs flow through the expanded region of the quartz tube and are deposited on a stainless steel mesh filter near the bottom [32]. This process usually leads to SiNCs with diameters from 3 nm (yellow emitting) to 4.5 nm (deep-red emitting) depending on the flow rate. However, adding a secondary gas mixture such as tetrafluoromethane and hydrogen in the second, bottom left inlet seen in Figure 6 will tend to etch the SiNCs allowing for green PL. Oxidizing these smallest SiNCs has the effect of creating a surface silicon dioxide layer thereby reducing the intrinsic size of the SiNCs as well as introducing oxide defect states. These two effects will create SiNCs that will exhibit very inefficient ($\sim$1 %) PL in the blue. In Figure 7, the PL of large ($\sim$4 nm) red-emitting SiNCs down to the smallest ($\sim$2-2.5 nm) blue-emitting SiNCs can be seen.

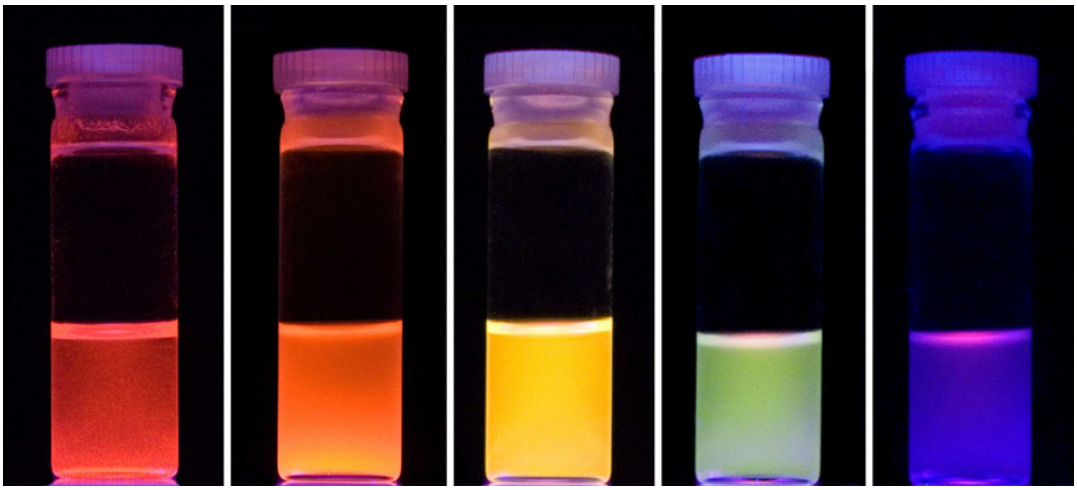

Figure 7: Image of SiNCs in methanol and emitting colors across the visible spectrum [33]. The samples were excited with a UV lamp at 365 nm.

In order to work with the SiNCs in various solvents, a passivation process is executed. The steel mesh filter containing the SiNC powder is transferred to a sealed nitrogen atmosphere where it is brought into an ethanol bath and then sonicated to release the SiNCs. These initial SiNCs do not form a stable colloid and appear cloudy and dark in solution. This solution is transferred to another flask containing

mesitylene and the passivating ligand such as 1-dodecene. Heating this solution at 165 °C for a few hours produces a hydrosilylation reaction and the solution turns clear. This clear solution contains well dispersed SiNCs covalently bonded with the ligand [32]. Further X-ray diffraction (XRD) and transmission electron microscopy (TEM) analysis verifies the crystallinity of the newly created SiNCs. Figure 8 shows the intensity versus 2θ profile of two different sized samples where the vertical lines indicate the intensity peaks of the given Miller indices of bulk silicon. The peaks match nearly perfectly indicating the strong crystalline nature of the SiNCs. Using the Scherrer equation (2.3) and the linewidth broadening of the XRD peaks, the approximate size of the as-produced (AP) SiNCs was able to be determined which was later confirmed through TEM and atomic force microscopy (AFM). Specifically,

$$L = \frac{K\lambda}{\beta \cos\theta} \tag{2.3}$$

where K is the dimensionless shape factor ($\sim$0.89 for spherical particles), λ is the X-ray wavelength, β is the line broadening or the full width at half maximum (FWHM) in radians and θ is the Bragg angle. Analyte A has a mean diameter of 3.2 nm while analyte B has a mean diameter of 4.1 nm. The inset in Figure 8 shows a TEM image of a typical SiNC with a dotted boundary to aid the eye and a 1 nm scale bar. The crystalline planes of silicon atoms show up as dark parallel lines.

2.9. Conclusion

A brief description of how the SiNCs used in this study were made has been given. These synthesis schemes, along with other common methods including those which we are currently using to create our own SiNCs, demonstrate the variety of ways SiNCs can be created. It should be noted that there are other methods and variants of those already described that can be used to create SiNCs. Each method

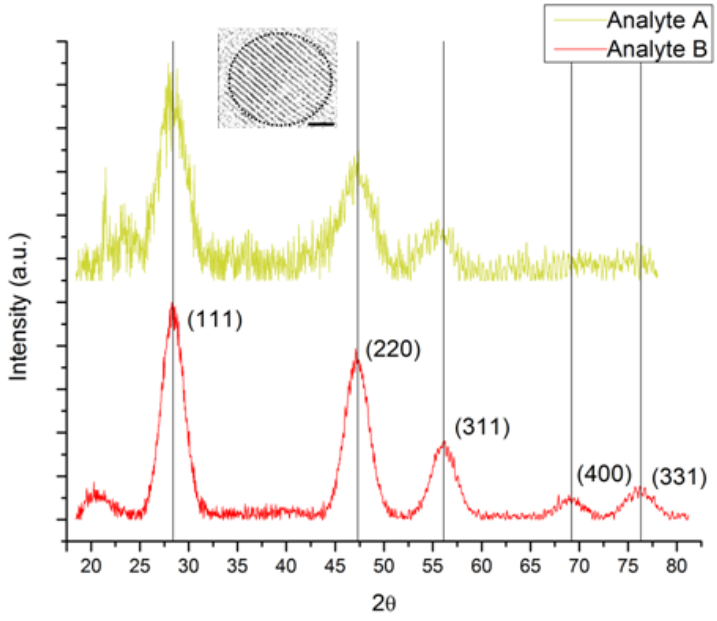

Figure 8: XRD graph of two SiNC samples. Analyte A has a mean diameter of 3.2 nm and analyte B has a mean diameter of 4.1 nm. The peak intensities of bulk scattering corresponding to the Miller indices given in parentheses are shown. Inset is a TEM micrograph with a dotted boundary to aid the eye and 1 nm scale bar. XRD data courtesy of Rebecca Anthony [34].

has its own advantages and disadvantages related to the crystalline structure, size uniformity and surface defects and passivation. As with most processes, the long term goal is the commercialization of SiNCs and composite systems and so the given advantages and disadvantages must be weighed with the cost of production and ease of fabrication that goes with each synthesis method.

Although it is debatable, the solution and plasma based methods appear to offer the best routes to create efficient, stable SiNCs with relatively high output and low cost. However, for this study, the main goal is to understand the properties of the plasma synthesized SiNCs and then determine the best way to enhance these properties for the realization of potential commercial applications.

CHAPTER 3. THE PHYSICS OF NANOCRYSTALS

For most bulk semiconductor materials, solid-state physics is able to describe systems with relatively high accuracy. In these macroscopic systems, the 'Bloch' description of an infinite extension of atoms on a periodic lattice is a sufficient model that can account for the majority of the bulk material properties, excluding some minor, yet important, surface effects. This description of materials is applicable to very small dimensions: all the way down to a few micrometers. However, for nanomaterials, specifically nanocrystals, this simple description begins to break down and the energy levels start to vary. For semiconducting nanocrystals, both the energy and density of states become discretized.

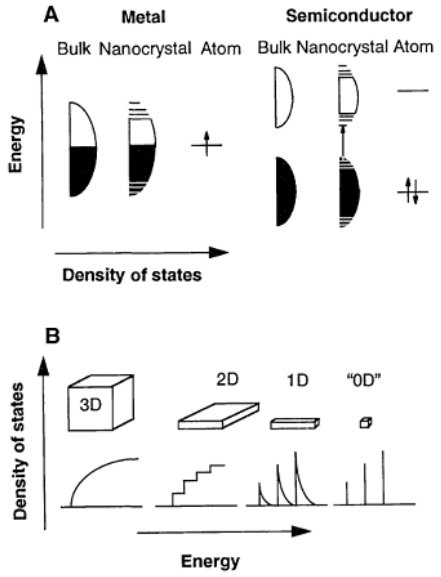

Figure 9: (A) A comparison of the density of states in metals and semiconductors. (B) Comparison of the density of states of one band for materials of different dimensions [35].

So at what threshold length scale does the general 'Bloch' description break down and the energy states become discretized? This is an interesting and important question to consider. According to Bragg X-ray scattering measurements and TEM micrographs, nanocrystals tend to have both the same lattice spacing and structure

as the macroscopic bulk materials [36]. So it seems odd that nanomaterial with the same structure and underlying unit cell length would have different and varying energy levels compared to its bulk nature. However, at a characteristic length the 'quantum phenomena' begin to appear. For a charge carrier, such as an electron, this characteristic length can be described by the de Broglie length $l_B = h/p$. It can generally be said that if $l_B/a \geq 1$, where a is the lattice length constant (physical dimension of the crystal lattice unit cell), the quantum mechanical properties of the materials will become important [35].

3.1. Simple Spherical Model

Modeling the electronic properties of materials smaller than the characteristic length can be quite difficult. We will start here with the simplest model for a spherical nanocrystal. This model assumes there is a constant spherical potential within a nanocrystal of radius a and an infinite potential outside:

$$V(r) = \begin{cases} 0, & r < a \\ \infty, & r > a \end{cases}. \tag{3.1}$$

Considering a particle of mass m and following [37], the solutions to the Schrödinger equation are

$$\Psi_{n,l,m}(r,\theta,\phi) = C\frac{j_l(k_{n,l}r)Y_l^m(\theta,\phi)}{r} \tag{3.2}$$

where C is a normalization constant, $j_l(k_{n,l}r)$ is the lth order spherical Bessel function, $Y_l^m(\theta,\phi)$ is a spherical harmonic and

$$k_{n,l} = \frac{\alpha_{n,l}}{a} \tag{3.3}$$

with $\alpha_{n,l}$ the nth zero of j_l. Substituting the solutions back into the Schrödinger

equation yields the discrete energy values of the particle:

$$E_{n,l} = \frac{\hbar^2 k_{n,l}^2}{2m} = \frac{\hbar^2 \alpha_{n,l}^2}{2ma^2}. \tag{3.4}$$

These energies are identical to that of a free particle except for the spherical quantization imposed by the boundary condition [38]. It is important to note that the energy dependence goes as $1/a^2$ which creates a dramatic increase in energy as the nanocrystal size decreases.

In general this 'quantum confinement' energy can be added to the bulk band gap energy E_0 (usually calculated with a Bloch analysis for solid-state materials) to give a decent description of the nanocrystals band gap energy E_g:

$$E_g = E_0 + \frac{\hbar^2 \alpha^2}{2ma^2}. \tag{3.5}$$

However, this is not a complete nor perfectly accurate description of nanocrystals. The correlation energy, spin-orbit coupling and Coulomb attraction of the electron-hole pair (i.e. the exciton) can be important within nanocrystals and nanoscale systems. Thus, in order to get a more accurate description we need to expand upon the simple Bloch description. Many models have been employed to do this such as density functional theory, the effective mass approximation and the tight-binding approximation [linear combination of orbitals (LCAO) approximation]. The tight-binding method is very useful when electrons move slowly around lattice points and is quite successful in describing indirect band gap nanoscale materials, particularly SiNCs.

3.2. Tight-Binding Approximation

The tight-binding approximation method gets its name from the situation where electrons or holes are 'tightly' bound to the atomic lattice points. It is assumed that in the vicinity of each lattice point the full period crystal Hamiltonian (H) can be approximated by the Hamiltonian (H_{at}) of a single atom on the lattice:

$$H_{at}\Psi_n = \left(\frac{-\hbar^2}{2m}\nabla^2 + V_{at}\right)\Psi_n = E_n\Psi_n. \tag{3.6}$$

This is true if the charge carrier's wavefunction $\Psi_n(\mathbf{r})$ becomes very small when r exceeds a distance on the order of the lattice constant [39]. Assuming the charge carrier's wavefunction is related to the atomic orbitals, it can now be written as a linear combination of atomic orbitals to give a new approximation:

$$\Psi_n(\mathbf{r}) = \sum_{\mathbf{R}} \psi_n(\mathbf{r} - \mathbf{R}). \tag{3.7}$$

Here the sum is over all lattice vectors $\mathbf{R}$. However, it can be shown that equation (3.7) only satisfies the Bloch condition,

$$\Psi(\mathbf{r} + \mathbf{R}) = e^{i\mathbf{k}\cdot\mathbf{R}}\Psi(\mathbf{r}), \tag{3.8}$$

when $\mathbf{k} = 0$. It then makes sense to conjecture a new wavefunction which will satisfy this condition for all $\mathbf{k}$ within the first Brilliouin zone:

$$\Psi_{n,\mathbf{k}}(\mathbf{r}) = \sum_{\mathbf{R}} e^{i\mathbf{k}\cdot\mathbf{R}}\psi_n(\mathbf{r} - \mathbf{R}). \tag{3.9}$$

This new function does indeed adhere to the Bloch condition given in equation (3.8)

because

$$\begin{aligned}
\Psi_{n,\mathbf{k}}(\mathbf{r}+\mathbf{R}_0) &= \sum_{\mathbf{R}} e^{i\mathbf{k}\cdot\mathbf{R}}\psi_n(\mathbf{r}+\mathbf{R}_0-\mathbf{R}) \\
&= \sum_{\mathbf{R}} e^{i\mathbf{k}\cdot\mathbf{R}}\psi_n(\mathbf{r}-(\mathbf{R}-\mathbf{R}_0)) \\
&= \sum_{\mathbf{R}'} e^{i\mathbf{k}\cdot(\mathbf{R}'+\mathbf{R}_0)}\psi_n(\mathbf{r}-\mathbf{R}') \\
&= e^{i\mathbf{k}\cdot\mathbf{R}_0}\sum_{\mathbf{R}'} e^{i\mathbf{k}\cdot\mathbf{R}'}\psi_n(\mathbf{r}-\mathbf{R}') \\
&= e^{i\mathbf{k}\cdot\mathbf{R}_0}\Psi_{n,\mathbf{k}}(\mathbf{r})
\end{aligned} \tag{3.10}$$

where $\mathbf{R}' = \mathbf{R} - \mathbf{R}_0$. The wavevector $\mathbf{k}$ can be confined to the first Brilliouin zone because

$$e^{i\mathbf{k}\cdot\mathbf{R}} = e^{(i\mathbf{k}+\mathbf{K})\cdot\mathbf{R}} \tag{3.11}$$

for any and all lattice vectors $\mathbf{R}$ [40]. Considering that solids contain many types of orbitals in their valence shell, these states will tend to overlap, interact and mix with neighboring orbitals. Thus, the linear combination of stationary state wavefunctions given in equation (3.9) cannot be the actual Eigenfunction of the charge carrier in the crystal [40]. Instead, we must let the valence electron's wavefunction be a weighted part of all atomic orbitals with most of the weight being placed on a few localized orbitals. The true wavefunction of the electron will be expressed as a part $[b_n(\mathbf{k})]$ of each stationary wavefunction,

$$\Phi_{\mathbf{k}}(\mathbf{r}) = \sum_n b_n(\mathbf{k})\Psi_{n,\mathbf{k}}(\mathbf{r}), \tag{3.12}$$

where the coefficient b gives the amount of Ψ_n in the final wavefunction. So $\Psi_{n,\mathbf{k}}$ can be thought of as the basis functions on which the electron wavefunction is composed.

It is now possible to find the final wavefunction by solving the Schrödinger equation,

$$H\Phi_{\mathbf{k}} = \epsilon_{\mathbf{k}}\Phi_{\mathbf{k}} \tag{3.13}$$

where $\epsilon_{\mathbf{k}}$ are the energy bands of the nanocrystal. It is only a matter of finding $\epsilon_{\mathbf{k}}$ and the coefficients $b_n(\mathbf{k})$. Following Pickett et al. [40], we multiply the Schrödinger equation on the left by $\Psi_{n,\mathbf{k}}(\mathbf{r})$ and integrate over all $\mathbf{r}$ which yields the following result:

$$\sum_n H_{m,n}(\mathbf{k})b_n(\mathbf{k}) = \epsilon_{\mathbf{k}} \sum_n S_{m,n}(\mathbf{k})b_n(\mathbf{k}). \tag{3.14}$$

The Hamiltonian matrix (H) and overlap matrix (S) are given by

$$H_{m,n}(\mathbf{k}) \equiv \int \Psi^*_{m,\mathbf{k}}(\mathbf{r})H\Psi_{n,\mathbf{k}}(\mathbf{r}) \tag{3.15}$$

and

$$S_{m,n}(\mathbf{k}) \equiv \int \Psi^*_{m,\mathbf{k}}(\mathbf{r})\Psi_{n,\mathbf{k}}(\mathbf{r}). \tag{3.16}$$

After determination of the H and S matrix values, the electron wavefunction and energy Eigenvalues can be found by solving

$$H(\mathbf{k})b(\mathbf{k}) = \epsilon_{\mathbf{k}}S(\mathbf{k})b(\mathbf{k}) \tag{3.17}$$

or, correspondingly, the secular equation

$$[H(\mathbf{k}) - \epsilon_{\mathbf{k}}S(\mathbf{k})]b(\mathbf{k}) = 0, \tag{3.18}$$

which is a general Eigenvalue problem to be solved using linear algebra [39, 40].

3.2.1. Simulation

There have been numerous attempts to apply theoretical models to nanocrystals in an effort to better understand the physics that is behind the nanocrystals' optical and electronic behavior. Because of the extreme amount of computational bandwidth required to do these simulations, many model approximations have been applied and each has its own usefulness to certain types of materials. For indirect band gap semiconductors such as SiNCs, it appears the tight-binding approximation is a great match. Delerue et al. [41] have used the linear combination of atomic orbitals method to model the luminescence of porous SiNCs. The spherical crystallites were modeled to have the same lattice structure as bulk which allows for symmetry operation of the T_d group and a reduction in calculations. Small variations near the crystal surface have been reported [42]; however, these variations are minute and should not substantially contribute to the crystal's band gap energy. Spin-orbit coupling is also neglected as its effect in silicon is negligible (as a side note, this negligible spin-orbit coupling is crucial in obtaining long spin coherence times that may be very valuable in creating SiNC qubits used for quantum computing). Hydrogen was used to simulate surface bonds with self-interactions excluded. This approach represents a hydrogen atom as one s orbital and a silicon atom by one s and three p orbitals. The Hamiltonian matrix (H) and overlap matrix (S) are constructed from the atomic orbital basis and the secular equation given in equation (3.18) is solved to find the one-electron wavefunctions and energies. The H and S matrices were built from empirical parameters which included interaction and overlap for the three nearest neighbors [41]. Fitting of the simulated band gap energy versus crystal diameter d for these calculations resulted in an approximate $d^{-1.39}$ curve. This curve is quite different from both the simple, idealistic 'particle in a sphere' calculation given at the beginning of the section as well as the effective-mass approximation which both

predict a d^{-2} curve. It is important to note that this LCOA method does appear to approach an exponent of -2 as d tends towards infinity [41]. It will later be shown that this description of the band gap energy works extremely well with our experimentally determined values (Figure 19). But first, the approach taken to produce size specific SiNCs and measure their band gap energies must be explained.

3.3. Absorption and Emission: from Bulk to Quanta

Bulk silicon is an indirect semiconductor. An electron cannot be excited across the band gap with pure incoming radiation energy but instead needs an ∼1 eV photon along with a corresponding phonon. This can be seen in Figure 10 where the apex of the valence band at Γ is shifted by some momentum Δp from the minimum of the conduction band located near X. This indirect nature of silicon makes it a very inefficient emitter and most of the radiation energy will be lost through nonradiative heating processes (Auger recombination, etc.). The energy band gap of bulk silicon can be extracted from the right graph in Figure 10. At 300 °K, the band gap is 1.18 eV. At energies greater than 1.18 eV, bulk silicon's absorption coefficient increases monotonically. Although the absorption of SiNCs follows a similar trend, the band gap structure begins to change at diameters less than 5 nm. The indirect minima located at X begin to flatten and increase in energy. At the same time, the energy level of a direct transition at Γ decreases in energy. As the diameter of the SiNCs decrease below the exciton-Bohr radius of bulk silicon (∼5 nm), the positions of the electrons become spatially confined. The confinement leads to a spread in the electrons' momenta due to the Heisenberg uncertainty principle $\Delta x \Delta p \geq \frac{\hbar}{2}$. These two effects allow for a higher probability of overlap between the electron and hole wavefunctions in both position and momentum space. This, in turn, leads to a higher radiative recombination rate and PL quantum efficiency. The process is illustrated in Figure 11.

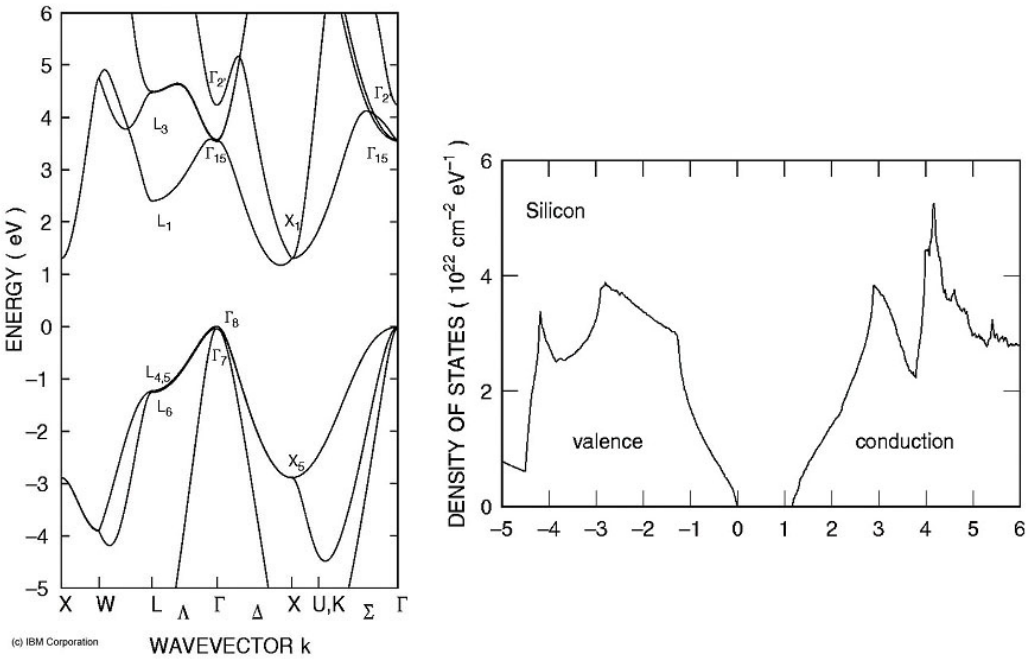

Figure 10: The band structure and density of states of bulk silicon [43, 44].

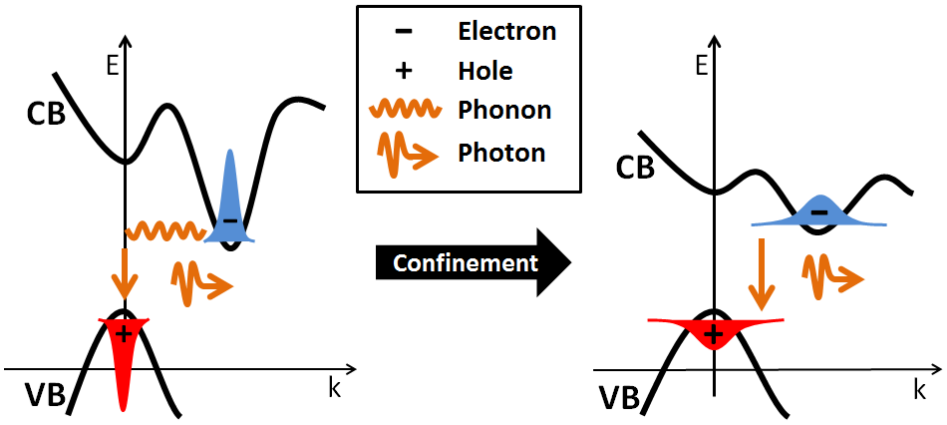

Figure 11: Modification to wavefunctions and band gap structure of bulk silicon due to confinement. The indirect band gap of bulk silicon requires a phonon to assist in the emission of a photon as illustrated in the left graph. SiNCs confine the exciton and spread out its momentum distribution giving a probability of direct radiative recombination as shown on the right. A flattening and change in energy of the band structure can be seen.

It will be shown later that this confinement has improved the PL quantum

yield of our passivated SiNCs to near 50 %. This is quite an astonishing improvement resulting mostly from a simple reduction in dimensional size.

The consequences of this enhanced PL efficiency and confinement prove to be quite exciting. As shown in Figure 7, a simple reduction in SiNC size can produce radiation across the visible color spectrum: from deep red to blue. It is this property of nanocrystals that make them exciting new prospects for a whole range of applications from visual displays (such as the computer monitor that you are most likely reading this dissertation on) to biomedical applications that rely on optical sensing.

3.4. Density Gradient Ultracentrifugation

As previously mentioned in the synthesis section, the SiNCs used in this study were synthesized using a non-thermal low-pressure plasma and ligand passivated though hydrosilylation. The SiNCs of analyte B (Figure 8) have a mean diameter of 4.1 nm with a standard deviation of 0.7 nm (17 %). Although this is quite good for SiNC synthesis schemes, it does not approach the size uniformity produced by synthesis of direct band gap semiconducting nanocrystals, such as cadmium selenide (CdSe), where a standard deviation of less than 5 % can be achieved. Size uniform SiNCs have many benefits that will be discussed throughout this dissertation but probably the most important is related to the self-assembly of films. The morphology of films is strongly influenced by the size distribution. Previous studies of entropic self-assembly in CdSe nanocrystal suspensions highlight the importance of size uniformity for the growth of ordered superstructures [45], while kinetic Monte Carlo simulations of colloidal crystallization suggest that the free energy of the solid-liquid interface increases strongly with supersaturation in polydisperse suspensions [46]. According to Auer et al. [46], the size polydispersity of a population must be less than 1.02 or $P_i < \frac{<x^2>}{<x>^2} < 1.02$ for entropic crystallization of the sample to occur. Since the plasma

synthesized as-produced (AP) SiNCs have a $P_i = 1.05$, it is necessary to size purify them into monodisperse fractions to allow for entropic crystallization.

Density gradient ultracentrifugation (DGU) is a tried and tested technique used heavily in biological and pharmaceutical sciences but is relatively new to the nanotechnology field. Density gradient ultracentrifugation can be used in a variety of situations but is often employed for material purification. The ultracentrifuge rotates the sample from hundreds to thousands of revolutions per minute. This rotation results in an apparent outward force on the sample that is actually a result of the change in inertial reference frame. The acceleration can be quite strong ($\sim$100,000g) and hence the centrifuge provides a nice tool to separate particles with such small mass. Figure 12 illustrates a typical centrifuge process where two samples of equal mass are placed in tubes on opposite sides of a spinning rotor which generates a force that is proportional to the distance from the center of the rotating shaft. The most influential determinant in the applied force is the rotational speed which causes a quadratic increase in the centrifugal force.

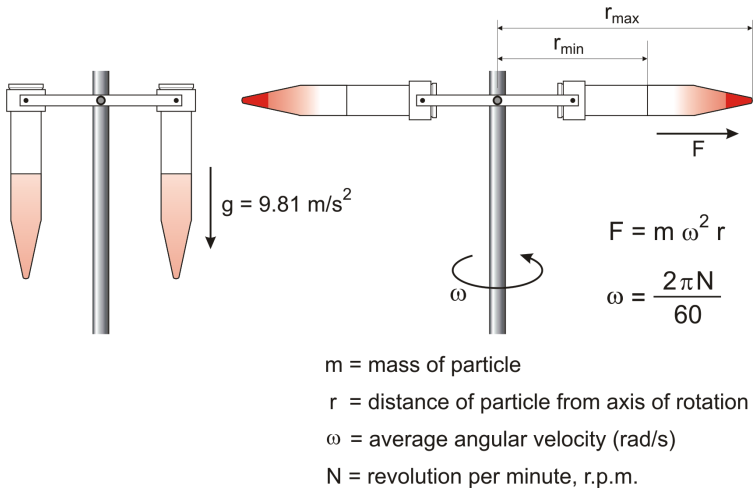

Figure 12: Illustration of the force applied to samples under normal gravity (left) and under the horizontal rotation produced by a centrifuge [47].

So far, the discussion has only involved the centrifugal force. However, spinning

SiNCs in a colloid solution are subject to two other forces. The first is common to any particle moving in a fluid. This drag force is very dependent on the object's shape, density and velocity as well as the type of fluid it is moving in. For objects with a large Reynolds number and relative velocity, the drag force is usually proportional to the velocity squared. This is different for a SiNC which has a very small Reynolds number. In this regime, the force is known as Stokes' drag and is proportional to velocity v, particle radius R and dynamic viscosity η [48]:

$$F_d = -6\pi\eta R v. \tag{3.19}$$

The second force is particularly important in DGU. The buoyancy force is given by Archimedes' principle and equal to the negative of the weight of the liquid displaced. When combined with the centrifugal force, this can be written as

$$F_b = a[m_p - m_f] = a[V(\rho_p - \rho_f)] = \omega^2 r[V(\Delta\rho)], \tag{3.20}$$

where ω is the rotational speed, r is the distance from the rotational axis, V is the volume of the particle (p) and displaced fluid (f) and ρ is the density. When the particles are in equilibrium, they will have a constant velocity; thus, the net force will be zero:

$$F_{net} = 0 = F_b + F_d = \omega^2 r[V(\Delta\rho)] - 6\pi\eta R v. \tag{3.21}$$

Rearranging and noting the volume V is that of a sphere, the terminal velocity is given by

$$v_t = \frac{2(\Delta\rho) r \omega^2 R^2}{9\eta}. \tag{3.22}$$

Given the appropriate density gradient (Section 3.4.1), the separation of different size SiNCs can be performed due to their different radii and the R^2 dependence of the

terminal velocity.

3.4.1. Experimental DGU Procedure

As-produced SiNCs were introduced into the solvent m-xylene. The separations were performed using a five-layer step gradient of 90 %, 80 %, 70 %, 60 % and 50 % chloroform by volume in m-xylene. All solvents were purchased from Sigma-Aldrich and used without further purification. Initial separations performed in commercial polyallomer tubes showed solvent-induced tube degradation that resulted in significant sample contamination. To prevent this, custom-made polyvinylidene fluoride (Kynar®) ultracentrifuge tubes, which show superior resistance to organic solvents, were obtained from Seton Scientific. Similarly, glass was used for all sample transportation and storage, which necessitated designing custom glass tips for Eppendorf micropipettes. The step gradient was layered into an 8 mL ultracentrifuge tube. This was done by pipetting 1.4 mL of the 90 % solution on the bottom of the tube, with subsequent layers deposited in order of decreasing density. A 300 μL solution of SiNCs in m-xylene (1 mg/mL) was then layered on top of the gradient. These solvents were chosen because of their similar viscosities and large density disparity. This allowed for a density range of $\sim$1.4 g/L to $\sim$0.8 g/L. It should be noted that the reason for the gradient is two-fold. First, it prevents run-away separation (or a more even separation) of the largest dots from the smallest dots because of the R^2 term in equation (3.22). Second, it mitigates the small eddies along the edge of the centrifuge tube associated with friction along the side wall [49, 50]. The completed sample was then immediately transferred to a SW-41 Ti swinging-bucket rotor and the separation was started.

A normal spin was done in a Beckman Coulter Optima L-80 XP ultracentrifuge at 30,000 revolutions per minute (rpm) for 10 hours at 1 °C. Given the need for special (Kynar®) tubes to resist decomposition from organic solvent coupled with the high

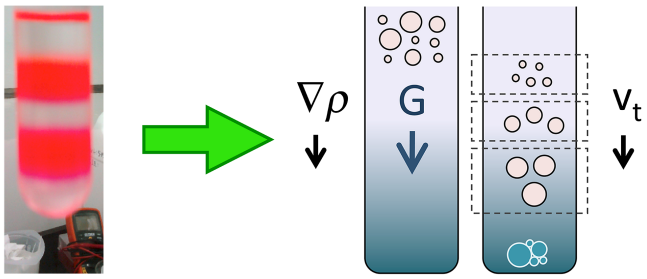

Figure 13: The separation of AP SiNCs in a DGU procedure. Left is an actual image of the chloroform/m-xylene gradient with dye added to help visualize the layers. Right is an illustration of the separation process: density and terminal velocity increase down the tube.

density of chloroform, 30,000 rpm was the highest safe rate at which we could spin the sample. Ten hours was needed for the largest SiNCs to reach the bottom of the centrifuge tube. The sample was spun at 1 °C to reduce fraction separation smearing from thermal diffusion.

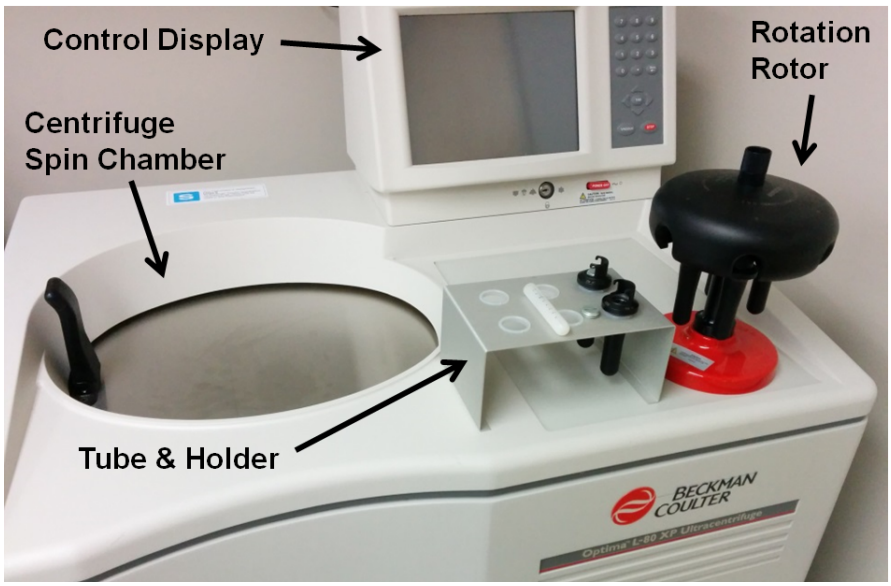

Figure 14: The ultracentrifuge setup.

After the centrifuge run was complete, the glass-tipped micropipettes were used to manually collect 200 μL fractions along the entire depth of the tube for analysis and characterization. The fractions were pipetted out starting at the top (fraction 1)

and continuing downward until we reached the largest SiNCs at the bottom. When necessary, identical fractions from multiple runs were combined to improve sample yield. To change solvents, samples were dried under vacuum and the solvent collected in a solvent trap. The fractions were handled and redispersed under an atmosphere of purified nitrogen gas. Nanocrystal films were cast on quartz and glass cover slips that had been cleaned with solvents and a UV-O plasma.

Transmission electron microscopy images of the SiNC fractions were taken with a JEOL JEM-2100 analytical TEM operated at 200 kV and collected using a GATAN Orius SC1000 bottom-mount CCD. Quantifoil grids (Ted Pella) with an orthogonal array of 1 μm diameter holes on 200 mesh copper were cleaned with chloroform and toluene, dried under vacuum, and placed on a UV-O cleaned glass cover slip. In order to deposit thin films on top of the TEM grids, the method illustrated in Figure 15 was employed.

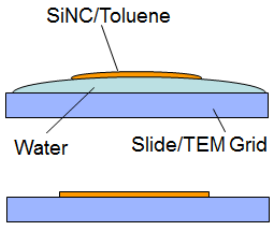

Figure 15: Thin film procedure for TEM analysis.

A small volume of water (10 μL) was dropped onto the grid, followed by 20 μL of a purified SiNC-toluene solution. The toluene quickly evaporates, eventually followed by the water, leaving the thin SiNC film (1-3 nanocrystals thick) draped over the holes in the grid. A typical TEM micrograph can be seen in Figure 16 along with the calculated size distribution for select fractions.

Using the TEM images, the average size and polydispersity index were determined. The average polydispersity index dropped from $\sim$1.05 to 1.01 after the DGU.

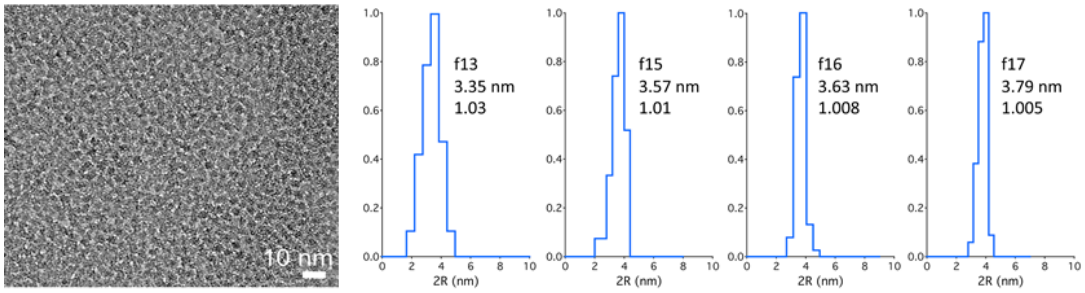

Figure 16: (left) Typical TEM micrograph of centrifuged fraction. (right) Size distribution graphs of several fractions and their average size and polydispersity index calculated from TEM micrographs.

This is exactly what we had hoped for as it decreased the polydispersity below that needed for entropic crystallization ($P_i = 1.02$).

3.4.2. Experimental Optical Characterization Procedure

These same fractions were then optically characterized with an inverted fluorescence microscope. An illustration of the generalized setup of an inverted microscope can be seen in Figure 17.

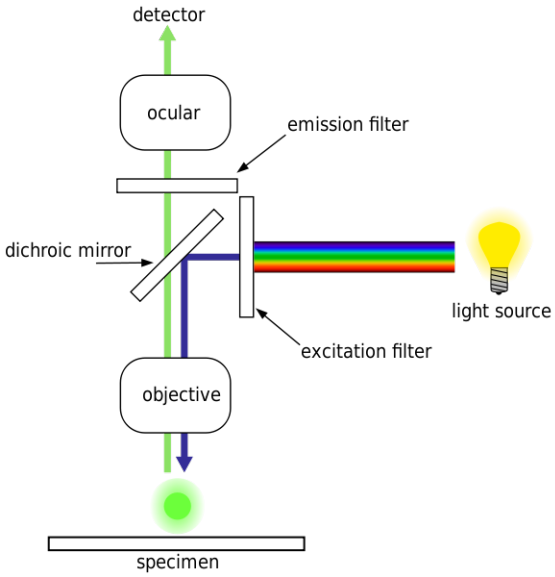

Figure 17: Illustrated setup of the inverted microscope and the epifluorescence technique used to collect optical data from samples. Image provided by [51].

Although different excitation light sources were used, generally the incoming

light had a wavelength peaked at 365 nm. The top of Figure 17 shows an arrow of the collected light going to a detector which in our case was either a spectrometer, high-sensitivity CCD camera or photomultiplier tube.

An actual image of our setup is shown in Figure 18. Optical measurements were generated using nearly simultaneous visible/NIR fluorescence imaging and NIR fluorescence and lifetime spectroscopy on a customized inverted Olympus microscope. Collimated variable-power fiber-coupled LEDs (365 and 395 nm), a fiber-coupled 20 mW Omicron PhoxX 375 nm laser and a fiber-coupled 15 mW ThorLabs 473 nm laser were used for continuous-wave (CW) excitation. Modulated pulsed excitation was delivered with a fiber-coupled pulsed UV laser (Advanced Laser Diode Systems, PiL037, 375 nm, 30 ps pulse width, 140 mW peak power, 1 kHz modulation) fiber coupled to a photomultiplier tube (Hamamatsu H10721-20) and read with a digital oscilloscope using Labview. UV-vis-NIR absorption/extinction was measured with a commercial spectrometer for both solutions and thin films. In later discussion, optical measurements in a nitrogen atmosphere were performed. These measurements were taken using a custom-made optical cell with an exhaust valve and an intake port connected through a pressure valve to a tank of purified nitrogen (N_2).

In Figure 19 the results from an ultracentrifuge run can be seen. Graph (a) shows the PL spectra from size specific fractions collected from the ultracentrifuge tube. The PL peaks are nicely separated from each other and produce a larger than 100 nm spread in emitted radiation wavelength. The AP spectrum is given for comparison in the black. The average size versus peak PL emission or energy band gap of each fraction can be seen in graph (b). The data was fitted to the computational calculated band gap of Delerue et al. following the LCAO method given in the previous Simulation Subsection.

The data fit well to the theoretical calculations with $E_0 = 1.12$ eV and $\alpha =$

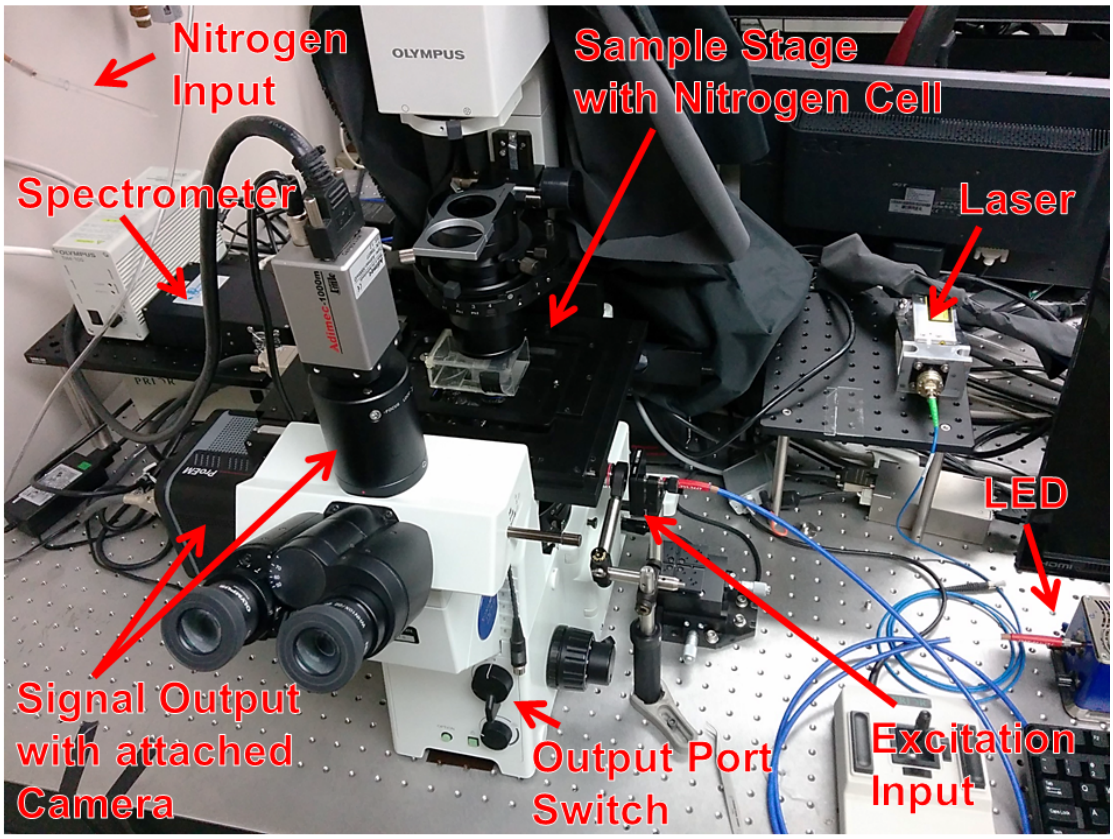

Figure 18: Actual setup of the inverted microscope and epifluorescence method used to collect optical data from samples.

4.02. Here E_0 is the band gap energy of bulk silicon at room temperature.

Comparison of the linewidth of a SiNC fraction, parent material (AP) and commercially available cadmium selenide (CdSe) nanocrystals can be seen in Figure 20(a). There is a substantial (30 %) reduction in the FWHM of the fraction compared to the parent material. The FWHM is still larger than the CdSe sample which can be attributed to the indirect band gap nature of silicon and the thermally coupled PL emission. Graph (b) shows the absorption and emission spectra of a select number of fractions and the parent material. Excitation wavelengths used in this study are given by the vertical blue lines.

To complement the TEM and optical data, tapping-mode atomic force mi-

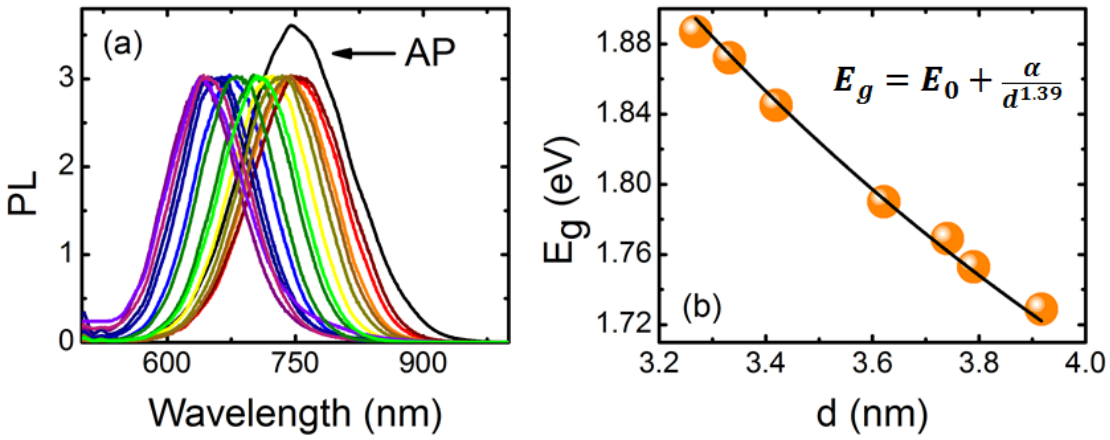

Figure 19: (a) PL spectra of centrifuged fractions excited at 365 nm. (b) The peak energy emission versus SiNC size determined through TEM measurements.

croscopy (AFM) was performed on SiNC samples before and after DGU. The explicit differences between films cast from these two samples are shown in Figure 21. The film made from a fraction (a) is flat, dense and homogeneous. However, the film made from the parent AP material displays large morphology and height differences as well as random voids in the film. This is a result of the DGU size purification coupled to the removal of excess 1-dodecene from the passivation process. It appears evident that DGU provides an efficient method for purification of SiNCs.

3.5. Conclusion

This section provided insight into the cause of the intense PL emission exhibited by SiNCs. A simple theoretical model was proposed where a SiNC was modeled as a spherical well with infinite potential. The results of this model are relatively accurate in explaining the band gap energies of spherical nanoparticles. However, a more precise method was needed to explain the deviation from the $1/R^2$ energy gap dependence in SiNCs. Therefore, the tight-binding method and calculations by Delerue et al. were described. Density gradient ultracentrifugation was performed on the AP SiNCs. This process allowed for the collection of monodisperse SiNCs of

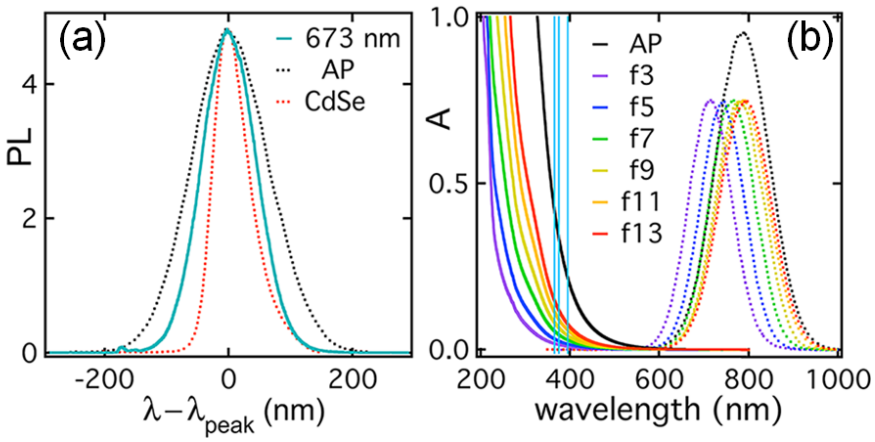

Figure 20: (a) PL emission from centrifuged fraction, parent material and commercially available CdSe nanocrystals. (b) The attenuance (solid) and emission (dotted) spectra of select fractions along with the parent material. Excitation wavelengths are given by the blue vertical lines.

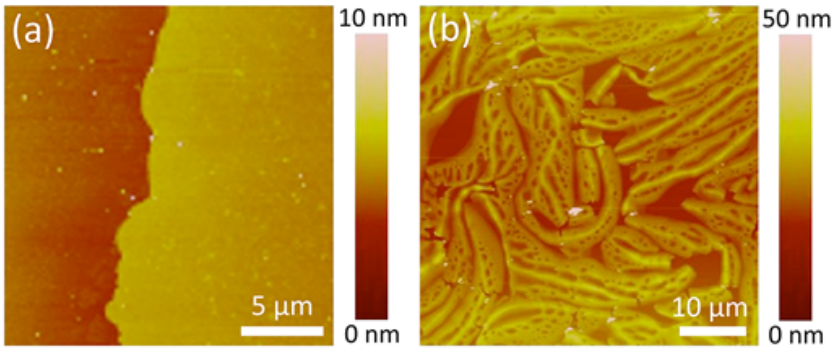

Figure 21: Tapping-mode AFM images of (a) fraction and (b) AP material. Films were cast from toluene on water, allowed to dry, and then deposited on a silicon wafer [34].

different sizes. Further analysis demonstrated agreement between the experimental and computational values for the band gap energy of SiNCs with size. It also demonstrated the usefulness of DGU for the purification of SiNCs.

CHAPTER 4. PHOTOLUMINESCENCE PROPERTIES

Silicon nanocrystals have many exciting potential applications. However, nearly every application requires the SiNCs to be monodisperse, stable and efficient. The previous section discussed the importance and creation of monodisperse SiNC fractions. This section will focus on the latter two qualities: stability and efficiency.

The stability of SiNCs can be disseminated into three separate regimes. The first is related to the stability of the SiNCs in solution. The most common way to work with nanocrystals is in solution; therefore, it is pertinent that SiNCs are stable and soluble in solution so that they can be easily handled and processed. The second regime is based on compositional stability. Silicon is very reactive with oxygen; thus, SiNCs will rapidly form a silicon oxide layer on their surface that can often be detrimental to their PL properties. The third stability regime is related to PL emission. Blinking, a time dependent cycling between the 'on' (emitting) and 'off' (non-emitting) states, is characteristic of all fluorescing materials, with SiNCs being no exception. This leads to unstable PL emission and a decrease in intensity over time (bleaching). Promoting long stable 'on' states for the use of SiNCs in fluorescence labeling applications is thus very important.

The efficiency of SiNCs can be defined as $E_{\mathrm{SiNC}} = \frac{E_{\mathrm{in}}}{E_{\mathrm{out}}}$. However, in most fluorophores the efficiency is measured in optical terms as the quantum yield: $QY = \frac{\#\text{ of photons emitted}}{\#\text{ of photons absorbed}}$. The efficiency of SiNCs is strongly coupled to both the compositional and emission stability. For instance, using SiNCs as a biological optical sensor requires that the nanocrystals do not decompose or react with excess oxygen in the body, exhibit continuous stable emission and have a high energy conversion efficiency. It would not be advantageous to require a high power excitation light source in order to successfully use the SiNC sensor. Consequently, SiNCs with high quantum yields are favorable.

4.1. Stability

In order to achieve highly stable SiNCs, surface passivation is key. The SiNCs used here are passivated through a thermal liquid hydrosilylation reaction with an alkene. Although multiple length alkenes can be used, 1-dodecene was the primary passivating ligand for this work. This ligand allows SiNCs to be dispersed and worked with in nearly any organic solvent, which is ideal for liquid phase processing routes. It is important to note that although this passivation leads to high solubility and homogeneously dispersed solutions, it is not 100 % complete. Even after performing hydrosilylation under reflux for hours, surface coverage is significantly below 100 % as a result of steric hindrance and other inhibiting factors; there will always be some dangling bonds. These unpassivated sites allow for potential reactions, most notably the reaction with oxygen. Oxygen can react and change the surface composition of the SiNCs which, in turn, can lead to a change in their effective size. Figure 22 shows an example of a SiNC passivated with 1-dodecene. Incomplete passivation can lead to an insulating silicon oxide layer indicated in blue. The oxidation reduces the effective diameter of the SiNC and can result in a more than 200 nm blue shift in the PL spectral emission [52].

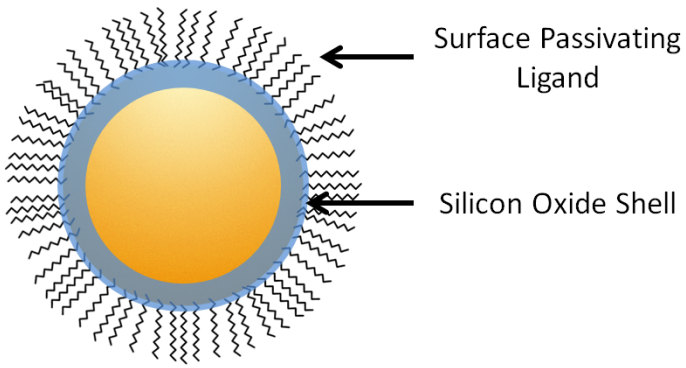

Figure 22: Illustration of a SiNC passivated with 1-dodecene. The blue interface represents the possible surface reaction with oxygen. A silicon oxide layer can form when passivation is not 100 % complete.

Molecular O_2 physisorbed on the surface of SiNCs can also alter their PL emission. Molecular oxygen has two excited singlet states above the triplet ground state. The second excited state ($^1\Sigma$) has an energy of 1.63 eV relative to the ground state. This energy matches up quite well with the peak energy emission of the SiNCs used in this study (∼1.7 eV). Since the energy transfer rate can be faster than the exciton relaxation rate, molecular oxygen can efficiently quench the PL of the SiNCs [53]. An explicit example of such quenching can be seen in the time step image in Figure 23.

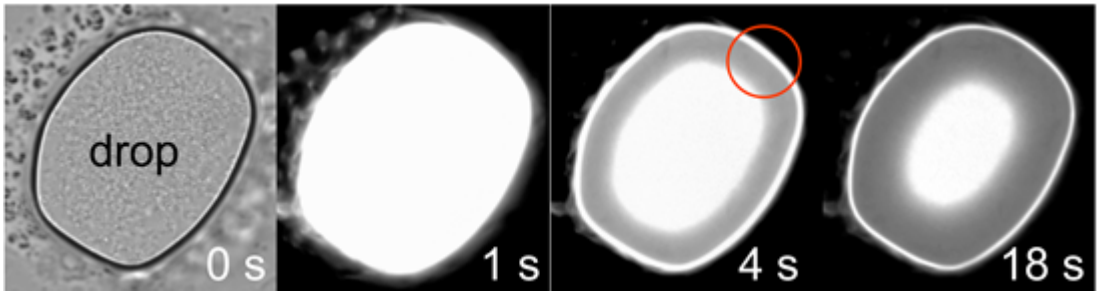

Figure 23: Efficient interfacial PL quenching by molecular oxygen. A bright field image of a SiNC cluster between two glass coverslips can be seen at $t = 0$ s on the left. The three right images show the quenching of PL by O_2 diffusing from the interface into the center of the sample. The sample was excited with 365 nm radiation and the images are grayscale.

The evolution of PL from a SiNC cluster between two coverslips in ambient conditions can be seen in Figure 23. The left image is the grayscale bright field image of the cluster. Immediately after $t = 0$ s, the 365 nm excitation source is supplied and the whole cluster fluoresces red. The three rightmost images are grayscale PL images. As time progresses, oxygen near the surface diffuses into the cluster where it quenches the PL emission. Hence, it is important to protect the SiNC surface from environmental oxygen which can be most effectively done by prudent surface passivation or working in a nitrogen atmosphere.

Figure 24 clearly demonstrates the benefits of having a nitrogen atmosphere. Not only is the PL intensity more stable over time (a-b) but the peak PL emission

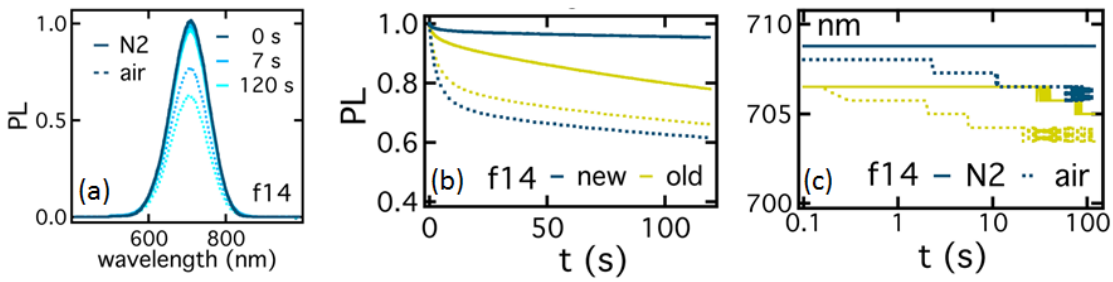

Figure 24: (a) The normalized PL intensity spectra of a SiNC fraction in nitrogen (solid) and air (dotted) at three different times. (b) The PL intensity trace of a freshly centrifuged SiNC fraction in nitrogen (solid blue) and air (solid yellow) and then again after 2 weeks of exposure to air (dotted lines). (c) The same sample as (b) but instead the peak PL wavelength plotted.

wavelength (c) also becomes more stable. Using SiNC-polymer nanocomposites is an alternative method for protecting the PL and will be investigated in future sections.

The passivation and compositional stability play a large role in the overall stability of the SiNC's PL. The phenomenon of blinking by fluorophores still lacks a clear agreed-upon description. It is believed that either the electron or hole of an exciton becomes trapped. These trap states are results of crystal and surface defects as well as surface-environment interactions. The trapping can be long lived and often leads to nonradiative recombination through Auger recombination and thermal relaxation. On the left of Figure 25, a PL still frame of a collected video of several different sized SiNC clusters can be seen. The right shows the PL intensity time trace of a cluster of 3 SiNCs. The fluorescence is seen to cycle between emitting on states and nonemitting off states.

Figure 26 shows the PL intensity time trace of a larger ∼100 SiNC cluster. The intensity varies but not in discrete steps as shown in Figure 25.

Investigation of SiNC cluster PL requires knowledge of both the peak PL wavelength and its intensity. Using Matlab, a program was coded to fit the PL near-Gaussian profile and collect both the peak PL wavelength and intensity with time. Using this Matlab program on the collected data of a large cluster of more than 10,000

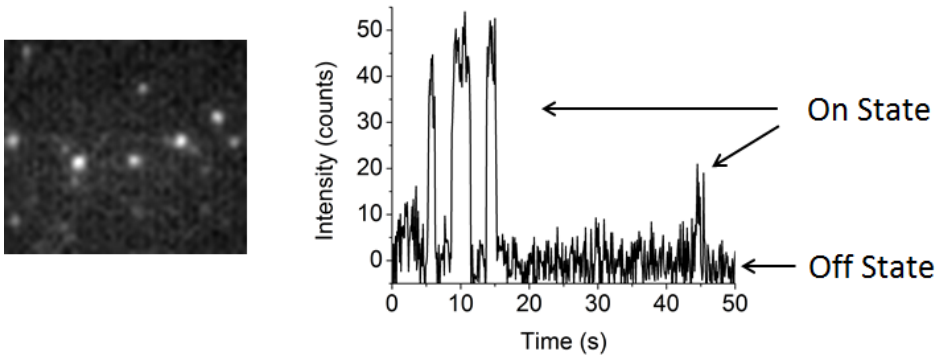

Figure 25: (left) PL still frame of one of the many collected videos of SiNC cluster blinking. Many clusters of varying size can be seen. (right) The PL intensity versus time trace of a cluster with 3 SiNCs. The combined cluster intensity shows times when no dots are emitting (off state) and times when 1 to 3 dots are emitting (on state).

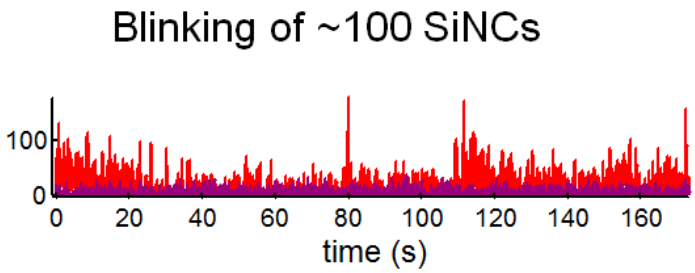

Figure 26: PL intensity time trace of a cluster of ∼100 SiNCs (red) against background noise (purple).

SiNCs produces the graph in Figure 27.

It is immediately evident that the blinking behavior of this large ensemble is no longer present. The accumulation of the trap states that produces the blinking in individual SiNCs leads to bleaching in larger ensembles. However, the decrease in intensity that is seen in Figure 27 is recoverable. In a one dimensional static trap model [54], the recovery rate from a trap state at distance x is given by

$$p_R(x) = B\exp(-\beta x), \tag{4.1}$$

which leads to a power law probability of the recovery time distribution (see Chapter

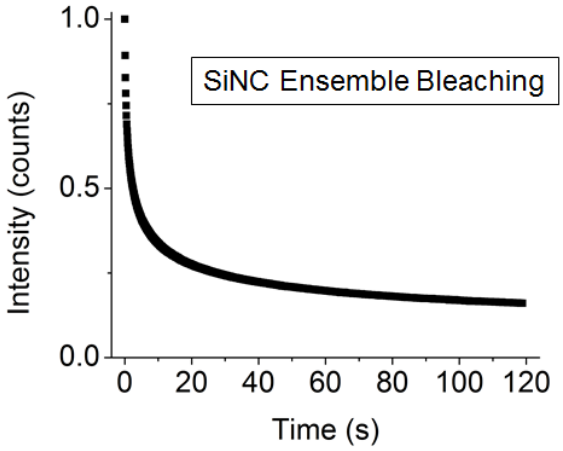

Figure 27: Normalized PL intensity versus time graph of a large SiNC ensemble. The ensemble contains more than 10,000 SiNCs. The collective blinking of this large cluster produces a decrease in PL intensity over time or 'bleaching.'

6). Leaving the SiNC cluster in the dark over several hours will allow the exciton to relax and upon further UV excitation, the initial PL intensity of the cluster will be observed.

4.2. Quantum Yields

Once stable SiNCs have been achieved, their efficiency must be addressed. The quantum efficiency or quantum yield (depending on the application) must be sufficiently high if there is to be a hope of using SiNCs in any commercial application. The average quantum yield of these AP plasma synthesized SiNCs is quite high at around 45 % - 50 %. The quantum yield is determined by recording the absorption and emission spectra of a SiNC solution. The SiNC solutions were placed in a Labsphere integrating sphere which was coupled through an optical fiber to an Ocean Optics USB2000 spectrometer. The spectrometer's spectral response was calibrated with a NIST traceable calibration lamp (Ocean Optics LS-450) [55]. A baseline was first collected using a vial with pure solvent and a 395 nm light-emitting diode (LED) source. Then, the PL spectra (with a reference baseline subtracted) of SiNCs

dispersed in hexane and sealed under a nitrogen atmosphere was collected. Each quantum yield calculation takes an average of three separate spectral measurements from both sample and reference, and each value is an average of at least two such measurements. A typical spectrum can be seen in Figure 28. Since the quantum yield is defined as the ratio of photons emitted to photons absorbed, the value was calculated by first multiplying the PL spectrum by the respective wavelength and then taking the ratio of the integrated PL spectrum to the integrated absorption spectrum.

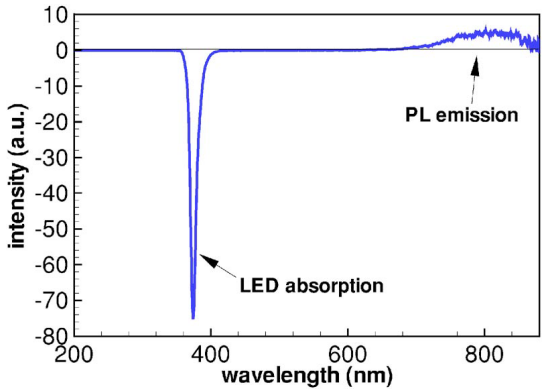

Figure 28: The absorption and emission of a typical quantum yield measurement from [55]. The LED absorption is negative because of the background subtraction.

A comparison of the AP quantum yield to that of the centrifuged fractions is presented in Figure 29. The fraction number on the horizontal axis refers to the distance down the centrifuge at which the sample was collected in the DGU process. Thus, as the fraction number increases so does the SiNC size. The quantum yields of the larger fractions (fraction 7-12) show a slight improvement over the AP but drop off quickly with the small fractions. This is similar to the results seen by Mastronardi et al. [56]. The quick drop in quantum yield can be attributed to the increase in surface effects. Since the surface to volume ratio (R^2/R^3) scales as $\sim 1/R$, these surface effects become magnified for smaller SiNCs. This enhances any nonradiative recombination resulting from surface trap states. Thus, the quantum yield is dramatically reduced.

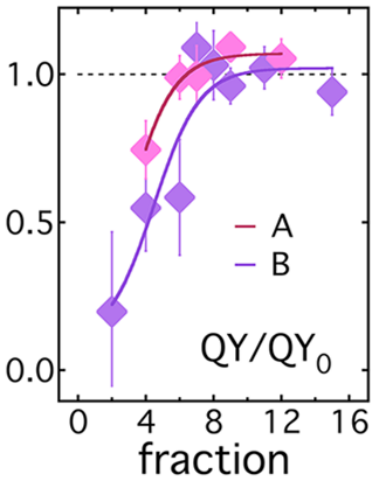

Figure 29: The quantum yield of centrifuged fractions normalized to the AP's quantum yield. The mean diameter of AP sample A and B are 3.2 nm and 4.1 nm, respectively. The fraction number on the vertical axis refers to the DGU collection process. The SiNCs increase in size as the fraction number increases.

It will be beneficial to use the larger fractions when making nanocrystal systems as this will remove the smaller, unfavorable SiNCs which would decrease the efficiency.

4.3. Fluorescence Lifetime

The entire process of fluorescence happens in three steps. The excitation light (usually UV) is absorbed by the sample, typically on the order of 10^{-15} seconds or one femtosecond (1 fs). This absorption excites an electron across the band gap to a higher energy level in the conduction band. This is followed by vibrational relaxation of the electron down to the lowest energy state in the conduction band which takes approximately 10^{-12} seconds or one picosecond (1 ps). The third and final step is the recombination of the excited electron with its hole across the band gap. In most fluorescent material, this final step is on the order of 10^{-9} seconds or one nanosecond (1 ns). Silicon is unusual in this way because having an indirect band gap lengthens the recombination time to microseconds (μs). It is important to note that this recombination can be both radiative and nonradiative and usually involves one of the three routes given in Figure 30.

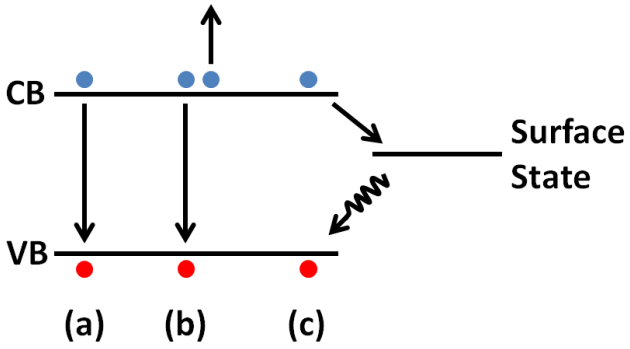

Figure 30: (a) Radiative recombination of electron (blue circle) in conduction band (CB) with its hole (red circle) in the valence band (VB). (b) Nonradiative Auger recombination where exciton energy is given to another electron in the conduction band. (c) This situation can result in both nonradiative and radiative recombination. Nonradiative recombination is a result of an excited electron becoming trapped in a surface defect state and recombining with its hole through thermal relaxation. Radiative recombination can happen when an excited electron recombines with a hole at a surface state site created from ligand passivation or environmental interactions.

In fluorescent materials, the population kinetics of the excited state can usually be given as

$$\frac{dN(t)}{dt} = -kN(t) = -(k_r + k_{nr})N(t) \tag{4.2}$$

where k_r and k_{nr} are the radiative and nonradiative rate constants and $N(t)$ is the number of excited SiNCs at time t. The nonradiative rate constant is the sum of all possible nonradiative rates. Integration of the equation leads to the following solution

$$N(t) = N_0 \exp^{\frac{-t}{\tau}} . \tag{4.3}$$

Here the fluorescence lifetime or characteristic time is

$$\tau = \frac{1}{k_r + k_{nr}}. \tag{4.4}$$

After an initial delta-function excitation, the population of excited SiNC decays

exponentially. The intensity from the population will be proportional to $N(t)$ and can be given as

$$I(t) = k_r N(t) = k_r N_0 \exp^{\frac{-t}{\tau}} = I_0 \exp^{\frac{-t}{\tau}} . \tag{4.5}$$

Hence, the fluorescence lifetime is the length of time it takes the emission intensity of the sample to reach $1/e$ or approximately $1/3$ the initial intensity [57].

Lifetime measurements of ensembles made from SiNC fractions were performed to determine the dependence on size. Figure 18 shows the setup used. The excitation source was a 375 nm pulsed laser (details in Section 3.4.2). The PL signal was output to a photomultiplier (PM) tube with variable intensity sensitivity. The PM tube was connected to an oscilloscope that output the data using Labview software (details in Section 3.4.2). Data were collected until a strong, smooth signal was observed and then the data were fit to a curve to extract the lifetimes.

As shown in Figure 31, the best fit to the lifetime data is not a pure exponential but what is known as a 'stretched' exponential. This is significant and provides insight into the relaxation behavior of the SiNCs. Stretched-exponential relaxation typically arises from a broad superposition of exponential decays, where for nanocrystalline silicon this distribution can reflect phonons, surface trap states, or recombination centers [58, 59]. It has recently been suggested that multiexponential relaxation is in fact intrinsic to indirect band gap semiconducting nanocrystals [60]. Direct band gap semiconducting nanocrystals and organic fluorophores have PL decays most often described by the pure exponential behavior that was just discussed. However, this is different in SiNC ensembles where the average decay is given by a stretched exponential.

The stretched exponential fit of the SiNCs suggest a slightly different dynamic behavior than was described above. In the presence of progressively depleted random sinks that capture excitations, the spontaneous decay kinetics given in equation (4.6)

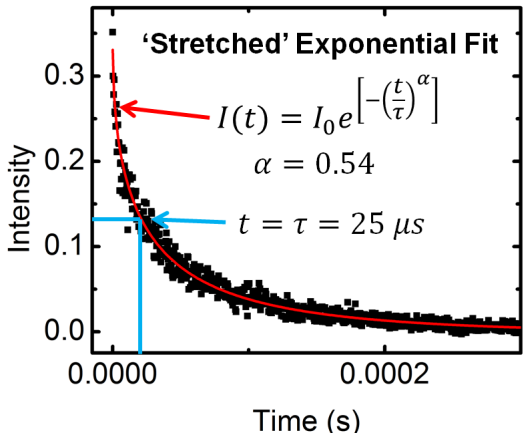

Figure 31: Typical stretched exponential fit (red) used to extract the lifetime (blue) of a SiNC ensemble.

can be such that the decay rate constants are dependent on time [61]:

$$\frac{dN(t)}{dt} = -K(t)N(t) = -\frac{k}{t^{\beta}}N(t), \tag{4.6}$$

where β is a characteristic constant [62]. Following the process described above, the emitted intensity of the SiNC system can now be given as

$$I(t) = I_0 e^{-\left(\frac{t}{\tau}\right)^{1-\beta}} = I_0 e^{-\left(\frac{t}{\tau}\right)^{\alpha}}, \tag{4.7}$$

where $\alpha = (1-\beta)$ is the stretching exponent. The reason for this 'stretching' behavior is not set in stone. There have been a number of different explanations such as exciton migration between interconnected nanocrystals, a hopping mechanism, variation of the atomic structure of SiNCs of different sizes, carriers out-tunneling from SiNCs to distributions of nonradiative recombination traps and varying carrier localization [63, 64]. A better understanding of the physical reasoning for this stretching may be made

by considering the mathematically equivalent definition for the intensity:

$$I(t) = \int_0^\infty e^{-\frac{t}{\tau}} \rho(\tau) d\tau, \tag{4.8}$$

where $\rho(\tau)$ is the continuous distribution of lifetimes [61]. The stretched exponential fit suggests that external fluctuations allow for numerous recombination routes that differ between nanocrystals and results in a nearly infinite sum of exponential decays from a SiNC ensemble.

Figure 32 plots the intensity versus time raised to the stretching exponent. This results in a straight line which clearly demonstrates the increase in lifetime with increasing peak PL wavelength (increasing SiNC size). The trend can be seen more easily in Figure 32(b) where the fluorescence lifetimes are plotted versus the peak emission energy. As the emission energy of the SiNCs increases, their size and fluorescence lifetime decrease. The lifetime is proportional to exp(-E/E^*) where E^* $\approx$ 0.2 eV [34].

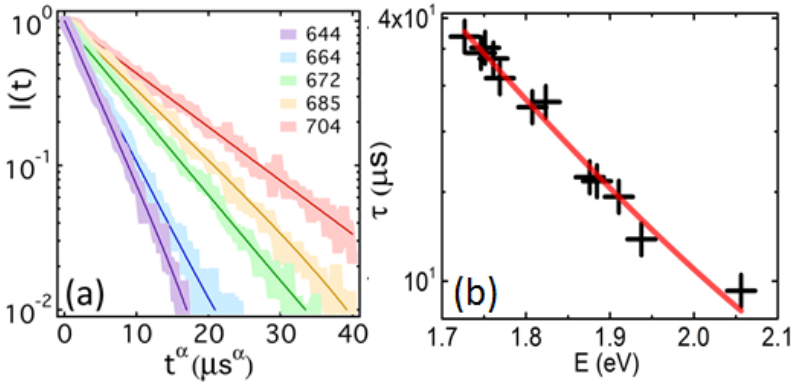

Figure 32: (a) Intensity versus t^α plots for SiNC fractions with PL peaks given. Typical fits used to extract the PL lifetime are shown where the stretching exponent $\alpha \approx 0.65$. (b) PL lifetime as a function of peak emission energy.

In the view of radiative recombination rates due to quantum confinement, the smaller the SiNC size, the greater probability of first-order direct radiative recombination because of the spread in the momentum distribution of the exciton [41].

This enhanced radiative recombination leads to a decrease in lifetime ($\tau_r = 1/k_r$). Although this contributes to the observed trend, there are likely other equally important reasons including greater electron-hole overlap and increased surface effects.

There have been reports in the literature [65–67] of a 'fast' decay rate associated with higher energies and possible direct recombination. Due to quantum confinement, the direct band gap energy is reduced, and the momentum vector of the exciton is spread out leading to higher probability of direct recombination and nanosecond decay. Recent developments to investigate this have been performed in our lab. Modifications to the PM tube and Labview signal collection software allow for short timescale PL collections down to a 200 picosecond time step. Due to the limitations of the setup, multiple collections need to be pieced together and the preliminary results for an AP sample at room temperature can be seen in Figure 33.

Although much weaker than the longer lifetime, the short decay appears to be real, and using a double exponential fit, the short lifetime is determined to be 1.9 ns with no stretching involved. The lack of stretching for the short lifetime has not yet been verified but may be due to the lack of environmental coupling as there is no phonon needed for this type of decay.

4.4. Power Dependence and More

Silicon nanocrystals have been shown to display PL dependencies on power. In the graphs in Figure 34 we can see two important dependencies that are demonstrated by the plasma-synthesized SiNCs used here. These graphs include both pure SiNCs and SiNC-polystyrene (PS) composites. The left graph in Figure 34 shows a clear linear dependence of the emitted intensity of both pure and composite samples with relative power. There is also a small blue-shift in the peak emission wavelength emitted as the excitation power increases. The reason for this is that large SiNCs have a higher absorption cross section compared to small SiNCs. This results in their

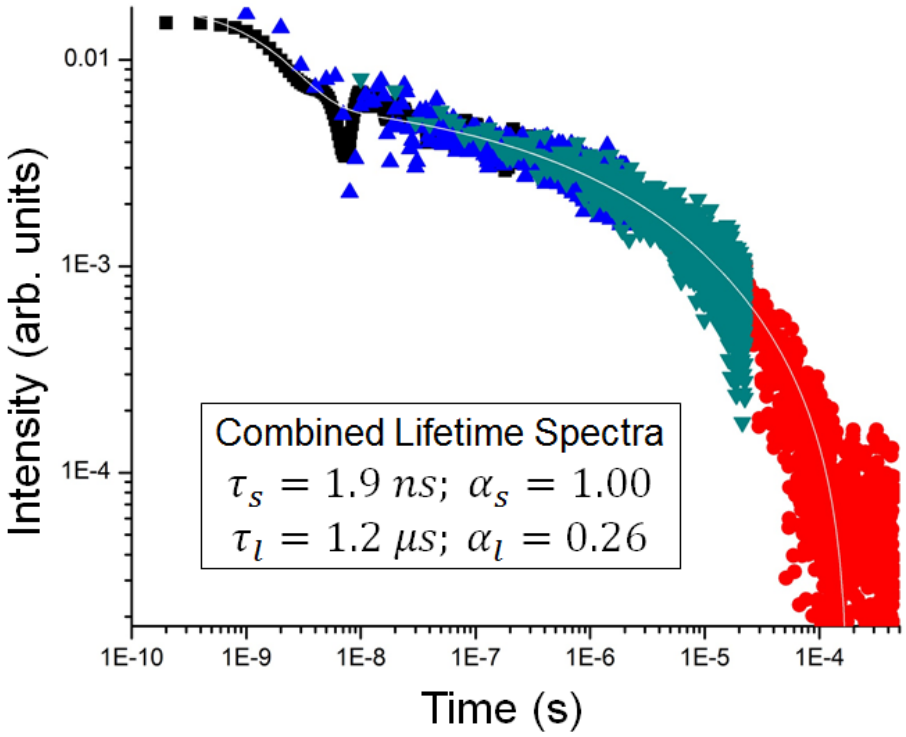

Figure 33: Four lifetime measurements (corresponding to the four colors) pieced together. A fit (white line) to the global data was perfomed and the lifetimes found are given on the graph where τ_s, τ_l are the short and long lifetime and α_s, α_l are the short and long stretching exponents.

emission being saturated at smaller excitation fluences while the small SiNCs are continuing to contribute to the total emission [68].

Further power dependent analysis led to an unexpected result. As the relative power increases, the half-life of both the pure and nanocomposite SiNC ensemble decreases substantially. The half-life is the time it takes for the emission intensity of the ensemble to reach half of the initial value [Figure 35(a)]. A long half-life means a more stable PL emission. Hence, it should be very beneficial to not use excess power. More insight and explanation into this phenomenon will be given in the next section.

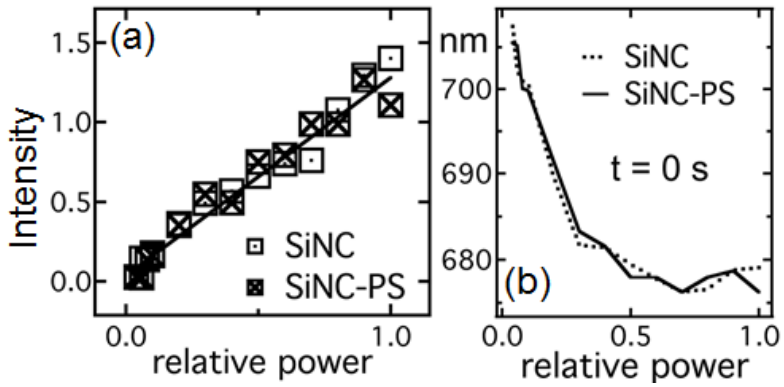

Figure 34: (a) Intensity and (b) peak PL emission wavelength versus the relative power from a 365 nm LED excitation source.

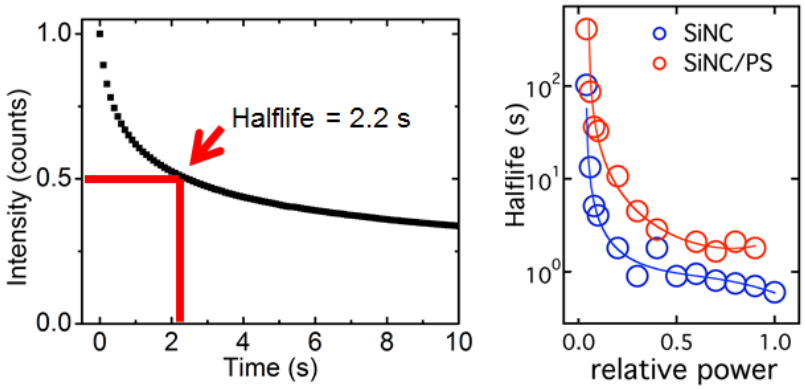

Figure 35: (left) Bleaching of a SiNC ensemble showing a calculated half-life of 2.2 s. (right) Half-life of pure SiNC and SiNC-polystyrene composite films versus relative excitation power.

4.5. Conclusion

In this section, the PL properties of SiNCs were examined using optical microscopy and fluorescence spectroscopy. The stability of SiNCs is highly dependent on their synthesis method and subsequent passivation process. However, the PL stability can also be dependent on environmental effects. Oxygen has a very negative effect on the PL stability, and it was shown that simply placing SiNC ensembles in a nitrogen rich atmosphere greatly improves their stability. Quantum yields of the parent material and centrifuged fractions were compared. The quantum yield shows a

slight improvement for large fractions but drops off drastically with decreasing SiNC size. The fluorescence lifetimes of fractions are calculated and shown to increase with SiNC size. Under pulsed excitation the intensity versus time profile of the SiNC PL is a stretched exponential. This stretching relates to the numerous routes of recombination and different decay rates for the individual SiNCs of an ensemble. With increasing relative power the SiNC emission intensity increases linearly while the peak wavelength blueshifts slightly for both pure SiNCs and SiNC-polystyrene composite films. An intriguing result is found where the half-life (essentially the PL stability) decreases as the excitation power increases.

CHAPTER 5. CLUSTER BRIGHTENING AND SILICON NANOCRYSTAL EFFICIENCY

There has been much discussion on different ways to improve the quantum yield of SiNCs beyond the improvements provided by quantum confinement. In recent papers [69, 70] an enhancement in nanocrystals arranged into clusters has been seen. This alteration in the PL emission cycle leads to an increase in the average time the nanocrystals remain in the emitting state. This effect, although still not completely understood, appears to be only from clusters and not from individuals. Therefore, it is fair reasoning to assume that analysis of the mechanics behind this enhancement might lead to improved quantum yield or at least improved stability.

5.1. Particle Packing Effect

According to a few recent articles [71, 72], there appears to be a correlation between the packing of nanocrytals and their PL. What we hypothesize is that as the nanocrystals become densely packed, their electron wavefunctions begin to overlap and interactions between two separate but very close nanocrystals become possible. Thus, if an excited electron is trapped in a dark surface state, it will feel an electronic repulsion from similar trapped electrons in neighboring nanocrystals as shown in Figure 36. A repulsion between these two electrons promotes the radiative recombination of the excited electron with its corresponding hole. It also reduces the likelihood that an electron will become trapped in a surface state defect by increasing the energy barrier required for this to occur. These two effects have the potential to increase PL efficiency and stability.

Some of the first data to suggest that there is some validity to this hypothesis was observed from the plot of ensemble PL half-life versus initial intensity shown in Figure 37. The log-log plot in Figure 37 suggests a substantial increase in the

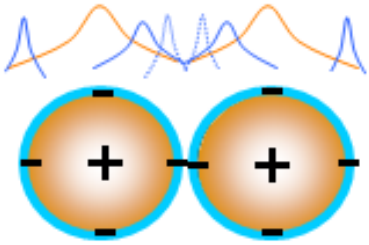

Figure 36: Repulsion between neighboring surface states increases overlap in electron-hole wavefunction, improving the rate of radiative recombination.

half-life of ensembles with larger initial intensity. Since PL is proportional to number of SiNCs, Figure 37 suggests that as the ensemble becomes larger in size, the half-life increases. An increase in half-life means an increase in PL stability and is very pertinent to achieving efficient SiNC ensembles. This exciting initial data encouraged further investigation into the reasoning behind the improved stability.

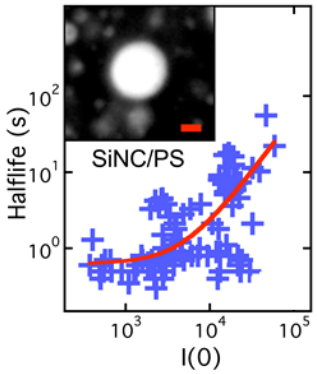

Figure 37: Half-life versus initial SiNC cluster intensity

Since the effects of particle packing were suspect, it was natural to first try to look at SiNC fractions because of their size uniformity, higher probability of self-assembly, high packing density and band gap homogeneity.

It was mentioned in chapter 3 that many beneficial effects can be attributed to creating monodisperse SiNCs. It was also explained that this was accomplished though DGU. The only remaining step required to test this suggestion of enhanced PL from close-packed nanocrystals was to design a method that encourages SiNCs

to self-assemble into densely packed structures. Although many methods were tried, one appeared to work the best and was actually quite simple. The SiNCs were first transferred to low-volatility (low vapor pressure) solvents such as m-xylene or toluene. A 5 μL drop of this solution was deposited on a cleaned glass coverslip (or a TEM grid on top of a cleaned glass coverslip). The coverslip had been annealed with 1H,1H,2H,2H-perfluorodecyltriethoxysilane which formed a fluorinated self-assembled monolayer (SAM). This surface fluorination caused beading and slower evaporation of the organic solvent. The sample was immediately covered with a plastic polytetrafluoroethylene (PTFE) cap. The low-volatility solvent and cap allowed for a crude but effective method for creating a close-packed SiNC cluster by controlled solvent evaporation. As noted previously, TEM measurements performed on thin films assembled from the fractions confirmed the tendency for close packing.

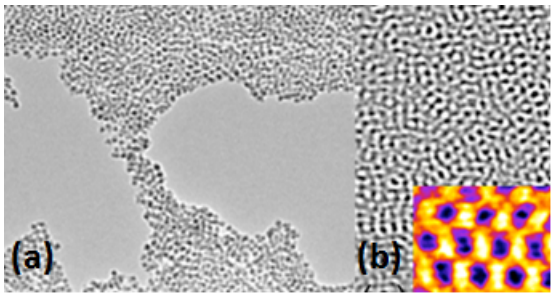

Figure 38: (a)-(b) Self-assembled films from a SiNC fraction. Densely packed SiNC thin films with short-range order are observed. The inset in (b) is a false color image of an area showing close packing and order.

Figure 38 shows two TEM images of thin films (1-3 nanocrystals thick) created from a SiNC fraction. In the inset in Figure 38(b), a false color image can be seen that highlights a region of what appears to be either a face-centered cubic or hexagonal close-packed structure. Either scenario results in the highest packing volume fraction for spheres ($\sim$0.74). Although long-range ordered packing has not been observed (this will be a discussion for a future section), short-range order and high packing density are found to occur. This result should be sufficient to test the interactions associated

with close packing and enhanced PL.

5.1.1. Brightening

In the section on PL properties, it was shown that the PL stability of SiNCs could be improved by removing the detrimental effects of oxygen. This improvement was based on the slower decrease in PL intensity with time or a reduced PL bleaching. The intensity of the SiNC ensemble was never greater than its initial intensity. What was observed after exciting a SiNC cluster created though the slow-drying method given above resulted in something quite surprising; the intensity of the SiNC ensemble increased in time.

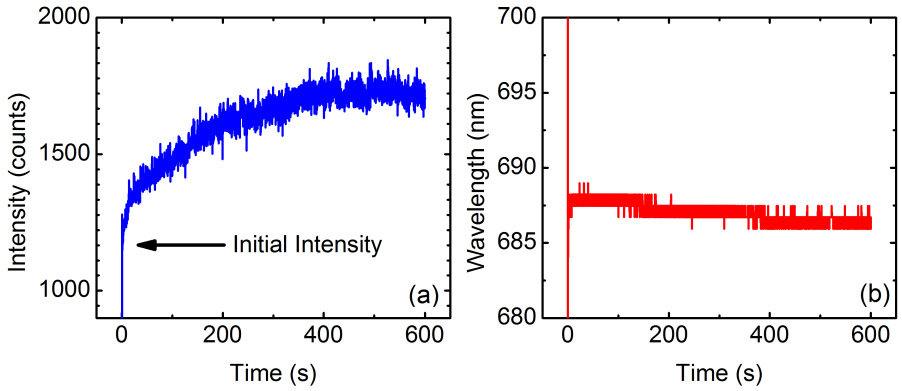

Figure 39: (a) The peak intensity trace of a fraction dried on a cleaned coverslip in a nitrogen atmosphere. The initial PL intensity is near 1200 counts and then begins to increase. (b) The peak wavelength of (a) plotted versus time. The wavelength is very stable over the 10 minute interval.

Figure 39 shows the peak PL intensity emitted over a 10 minute interval. The sample was made from a SiNC fraction. A droplet of $\sim$5 μL was placed on a treated (SAM) 1 x 1.5 inch glass slide which was inside the nitrogen flow chamber described earlier. As the solvent evaporated, the fractions formed large, dense clusters. One such cluster can be seen in the bright field image of Figure 40. This 'brightening' under continuous illumination is reminiscent of the photobrightening that has been well documented for the metal chalcogenides [69, 71, 72]. Here, the change in PL stability correlates with a difference in film morphology; less dense regions bleach,

while densely packed regions brighten. The increase of cluster intensity with time was observed to last from seconds to over an hour depending on the sample.

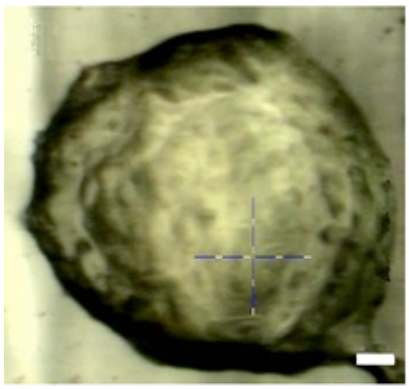

Figure 40: Fraction formed by slow evaporation on SAM slide. Scale bar is 10 μm.

Although particle-particle interactions appeared to be the cause behind this improved stability, PL activation and the finite extinction length of silicon need to be considered as well.

5.1.2. PL Activation

The first alternative is PL activation. According to Osborne et al. [73], a portion of CdSe nanocrystals in solution take time to 'activate' or go from a 'dark' state to an 'on' emitting state. The population of fluorescing nanocrystals within the colloidal suspension increases with time leading to ensemble 'brightening.' This continues until the trap state mechanism starts to dominate. At this point, the number of emitting nanocrystals begins to decrease and the characteristic 'bleaching' is observed.

If this PL activation is the source of the enhancement observed from the dense SiNC fractions in nitrogen, this enhancement should be observed in any SiNC film, independent of the packing density and polydispersity. A simple experiment was designed where films were formed from both the AP and fractioned SiNCs with varying densities. The density of the film was controlled though a combination of solvent choice and vapor saturation. Choosing a high-vapor-pressure solvent and

allowing it to dry under atmosphere created a thin, sparse film f_s. Choosing a low-vapor-pressure solvent and allowing it to evaporate under a PTFE cap created a thick, dense film f_d.

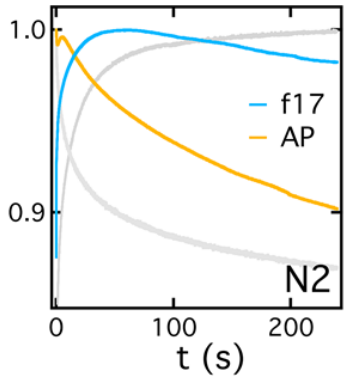

Figure 41: Typical PL intensity versus time curves for the AP (orange) and fraction (blue) f_d films in nitrogen. The fraction shows a superposition of the two distinct curves shown in gray.

It was immediately evident that PL activation could not be the reason for the enhancement. The f_s films were noticeably different from the f_d films. Both of the f_s films showed a rapid decrease in intensity with time. However, both of the f_d films displayed improved PL stability compared to the f_s films. The intensity of the light emitted from the AP f_d film was more stable and had a longer half-life than either of the f_s films but typically did not brighten. The intensity from the fraction f_d film showed even greater stability than the AP f_d film and nearly always demonstrated brightening (Figure 41).

5.1.3. Finite Extinction Length of Excitation in Silicon

The coupling of excitation light extinction and the onset of delayed PL in thick films may produce the effect of SiNC cluster PL enhancement. The finite optical extinction length of silicon is 10 nm using a 365 nm excitation source [74]. To test this, Monte Carlo simulations were performed on ordered clusters of noninteracting SiNCs based on previous work done by Cichos et al. [75].

There were two scenarios that could occur. In the first scenario, the absorption cross section of the 'dark' state is substantially reduced. This would result in more excitation light reaching SiNCs deeper in the sample beyond the 10 nm extinction length. However, upon evaluation and discussion with a chemist specializing in photochemistry, this scenario is unlikely [76]. A dark SiNC's absorption instead remains constant and the absorbed energy is lost through Auger recombination or other nonradiative recombination routes.

The second scenario is where the absorption cross sections of the 'dark' and 'bright' states are assumed to be equivalent, with a power that decays exponentially with depth and an initial PL proportional to power. For PL intermittency under CW excitation, the temporal distribution of 'on' and 'off' states follows decaying power-law statistics with exponents α_{on} and α_{off}. The PL intensity decays as $I(t) \propto t^{-\beta}$ with $\beta = 2-\alpha_{off}$. Measurements of the decay from sparse ensemble films f_s under N_2 suggest $\beta \approx 0.03 + 0.00926\ln(x)$, where $0.049 < x = P/P_{max} \leq 1$ is a dimensionless power ($P_{max} = 1$ mW) [34]. For this range of excitation, we established experimentally that the initial PL intensity, $I(0)$, is proportional to x. The excitation intensity decays with depth in the sample as $I(z) = I(0)\exp(-z/l)$, where we measure z and the extinction length (l) in units of nanocrystal diameter. Layer number is defined by an integer index that ranges from 0 to N, where 0 defines the top and $N + 1$ is the total number of layers. We consider $l = 2$ (with $N = 6$) and $l = 3$ (with $N = 10$). We model both simple cubic packing and FCC pyramidal packing, with the excitation incident on the base in accordance with the epi-illumination scheme. For cubic packing, the total intensity of a stack of j layers is

$$I_j(t) = \sum_{i=0}^{j-1} x_i A_i I_i(l,t) \tag{5.1}$$

where x_i is the local excitation power. We take $x_0 = 1$ with $x_i = \exp(i/l)$ for $i > 0$

and $I(l,0) = 1$ for all i. For an FCC crystallite, layer number i (from the bottom) has area $A_i = (j-i)(j-i+1)/2$ for a tetrahedron of j layers. The time dependent intensity for a j-layer stacking is then similarly

$$I_j(t) = \sum_{i=0}^{j-1} x_i A_i I_i(l,t). \tag{5.2}$$

Following Chicos et al. [75], the time evolution of 'on' and 'off' states for a single quantum dot follows the 2 x 2 set of first-order coupled rate equations

$$\begin{aligned} \frac{dn_{on}}{dt} &= -k_{on} n_{on} + k_{off} n_{off} \\ \frac{dn_{off}}{dt} &= -k_{off} n_{off} + k_{on} n_{on} \end{aligned} \tag{5.3}$$

where k_{on} and k_{off} are rate constants. The variables n_{on} and n_{off} represent the density of the two states and we assume there is no activation time, as stated earlier. For nanocrystals, the rate constants are time dependent, which necessitates a Monte Carlo (MC) scheme. Specifically,

$$k_{on} = \frac{\alpha_{on} - 1}{\bar{t}}; \quad k_{off} = \frac{\alpha_{off} - 1}{\hat{t}} \tag{5.4}$$

where $\bar{t}$ ($\hat{t}$) is the amount of time a particle has been in the 'on' ('off') state and must be distinguished from the actual time t. For $\alpha_{on} > 2$ and $\alpha_{off} < 2$, the intensity decays as $t^{-(2-\alpha_{off})}$. For $x = 1$ and $\alpha_{off} = 1.97$, the simulations were performed using $\alpha_{on} = 2.08$, while for smaller values of x, α_{on} was assumed to decrease in a weakly linear fashion with β in order to broaden the region of asymptotic scaling. To eliminate short time divergences in the MC algorithm, we used

$$k_{on} = \frac{\alpha_{on} - 1}{\sqrt{0.01 + \bar{t}^2}}; \quad k_{off} = \frac{\alpha_{off} - 1}{\sqrt{0.01 + \hat{t}^2}}. \tag{5.5}$$

The equations were solved numerically using a discrete-time MC procedure with a time step of $\Delta t = 0.02$.

The results for simple cubic and face-centered cubic (FCC) packing in Figure 42 suggest enhanced PL stability with increasing film thickness, but there is no indication of brightening.

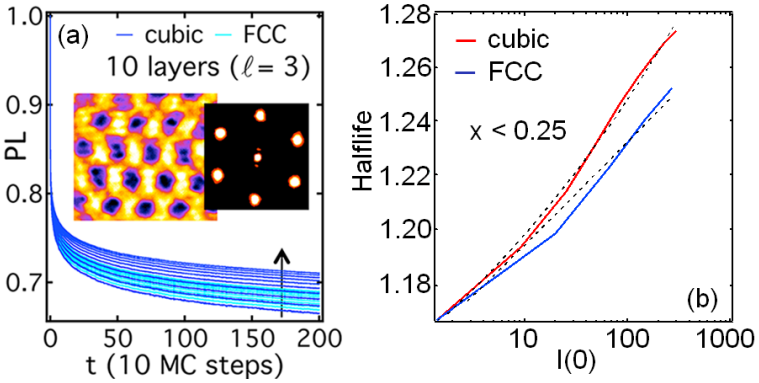

Figure 42: (a) MC simulation of photobleaching for 1-10 layers in simple cubic and FCC pyramidal packing with an extinction length of 3 layers. Each trace corresponds to an additional layer, and the arrow indicates increasing thickness. The inset shows a filtered TEM image of locally ordered close packing and the corresponding FFT. The width of the real-space image is 50 nm. (b) Increase in PL half-life with initial cluster intensity for both cubic and fcc type packing structures. The results are for power $x = P/P_{max} < 0.25$ where $P_{max} = 1$ mW.

5.1.4. Particle-Particle Interactions

Based on the lack of PL activation and the finite extinction length of silicon to describe the brightening behavior observed, reasoning again pointed to the initial suggestion of particle-particle interactions. To further explore this possibility, an investigation to quantify the impact of cluster size and excitation power on the PL enhancement was done.

We define a brightening interval as the duration over which the PL increases under continuous illumination. Figure 43 shows the measured brightening interval in the plane of excitation power and cluster size for a fraction. At fixed power, the interval increases with increasing size. For fixed size, the interval decreases with

increasing excitation power. For sufficiently large clusters excited at sufficiently low power, the increase can continue on for many minutes (up to over an hour). The brightening can also persist without excitation, as previously observed for CdSe [77].

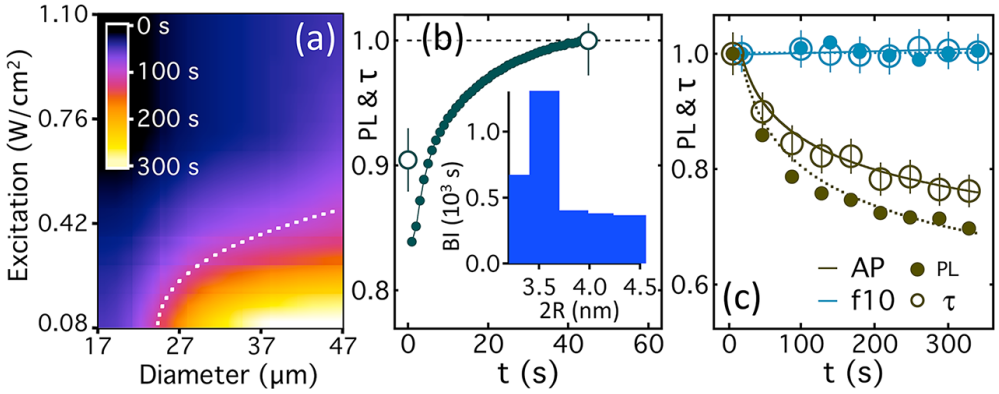

Figure 43: (a) Brightening interval in the plane of excitation power (375 nm) and cluster size with the fit as described in the text. (b) Brightening under continuous illumination at 365 nm (115 mW/cm^2), where the open circles denote τ (normalized by final value) before and after the illumination interval. Data represent an ensemble average of multiple spots under N_2. The inset shows brightening interval (BI) in units of 10^3 s as a function of nanocrystal diameter for fractions at comparable cluster size and excitation power (50 μm and 80 mW/cm^2). (c) PL and τ (normalized by initial values) during a bleach for the parent and for a photostable cluster. PL and τ were measured simultaneously under N_2 with modulated pulsed excitation (375 nm, 1 kHz, 30 ps pulsewidth, 67 mW/cm^2 mean excitation power).

These data support the findings that there is a particle-particle interaction effect that becomes stronger for thicker, larger clusters. This suggests that electronic interactions between surface trap states in packed arrays of monodisperse SiNCs increase the likelihood of radiative recombination, thereby enhancing the QY of the cluster. A similar mechanism has been proposed for the metal chalcogenides [69,77–79]. In terms of kinetics, the QY is $k_r/(k_r + k_{nr})$, where k_r and k_{nr} are rate constants associated with radiative and nonradiative relaxation, respectively. These equilibrium constants define both the lifetime, $\tau = (k_r + k_{nr})^{-1}$, and the radiative lifetime, $\tau_r = k_r^{-1}$, with QY $\propto \tau$ for a specific fraction in a given morphology. By simultaneously measuring PL and τ during brightening/bleaching [Figure 43(b,c)], we tested the link between

brightening and QY. Figure 43(b) shows brightening under continuous excitation, with lifetime both before and after the interval of illumination, for a film assembled from a fraction. There is a significant increase in τ, consistent with an increase in QY. Conversely, continuous excitation with a modulated pulsed laser confirms a drop in τ during bleaching for a film assembled from the parent [Figure 43(c)]. A significant implication of this is photostable luminescence in response to an appropriately pulsed excitation, as we demonstrate in Figure 43(c) for a film assembled from a fraction.

How reduced polydispersity promotes brightening is an intriguing question. Previous studies of CdSe films suggest that 'dark' surface trap states can be passivated by slowly diffusing photoelectrons, thereby increasing the QY of the ensemble [77]. We propose a similar mechanism. The quasi-static rate of change of the QY is $-\tau^2(dk_{nr}/dt)/\tau_r$, with bleaching for $dk_{nr}/dt > 0$ and brightening for $dk_{nr}/dt < 0$. For a cubic ensemble of size L, the power density is $PL^2/L^3 = P/L$, where P is the excitation power per unit area. We assume there are two competing terms in dk_{nr}/dt, with

$$\frac{dk_{nr}}{dt} = \frac{aP}{L} - \frac{bP}{L}L^{\delta} \tag{5.6}$$

where the first term models the rate of trap (dark state) production and the second, also proportional to power density, models the rate of trap annihilation. The factor of L^{δ} ($\delta > 0$) models the measured positive correlation between cluster size and brightening interval. At large power and small size, equation (5.6) is dominated by the positive (bleaching) term, while the negative (brightening) term dominates for small power and large size. Setting $dk_{nr}/dt = 0$ gives the transition, with brightening above a critical size, $L_c = (a/b)^{1/\delta}$, independent of power. Well into the brightening regime, the brightening interval is $L^{1-\delta}(bP)^{-1}$. The data in Figure 43(a) are in good qualitative agreement with this simple model. The onset of brightening coincides with a critical length scale ($L_c \approx 18 - 25\ \mu m$) that depends only weakly on power,

the brightening interval increases as $1/P$ at large L, and the data are consistent with $\delta = 0.70$ [dashed curve, Figure 43(a), with the contour of the constant brightening interval defined by $P \propto (L - L_c)^{1-\delta}$].

Interactions are paramount, being the source of the second term in equation (5.6). The rate at which trap states interact and annihilate depends on how fast they move through the cluster, which the data suggest increases with increasing cluster size. At comparable cluster size and excitation power, the data also suggest that the brightening is more pronounced for smaller nanocrystals [inset, Figure 43(b)], although the trend might be limited here by the rapid drop in QY at small diameters. A significant consequence of size purification will be 'band alignment', and when the energy states of individual SiNCs are well matched, there will be fewer inhomogeneities to impede the motion of electrons. The length of the ligand is also critical, as it dictates nanocrystal separation. Samples prepared from the same fractions but with varied drying times (25 s up to 225 s) showed a direct correlation between longer drying time, longer brightening interval, and increased localized tendencies for colloidal crystallization. To help verify the effects of crystallinity, an experiment was designed where polystyrene was used as a 'depletant' to induce phase separation into disordered (amorphous) SiNC and polymer phases. We chose polystyrene (PS, M_w = 18,000) with a chain size (radius of gyration) of 3.5 nm as a depletant, which is comparable in size to the nanocrystals. In a good solvent for both components, the phase diagram of such mixtures differs from that of a monodisperse colloidal suspension because the polymer induces a richer phase behavior, with coexisting solid, fluid and gas phases [80]. We chose a ratio of PS to SiNC (1:3 by mass) that forces dilute SiNC-PS-toluene solutions to pass through a viscous 'fluid-gas' coexistence region as they dry. By controlling the drying rate, we promote phase separation over crystallization and trap the mixture in a disordered packing arrangement (Figure 44). The absence

of any crystallinity in the SiNC phase was also inferred from a lack of birefringence. This was able to simultaneously suppress entropic crystallization and brightening,

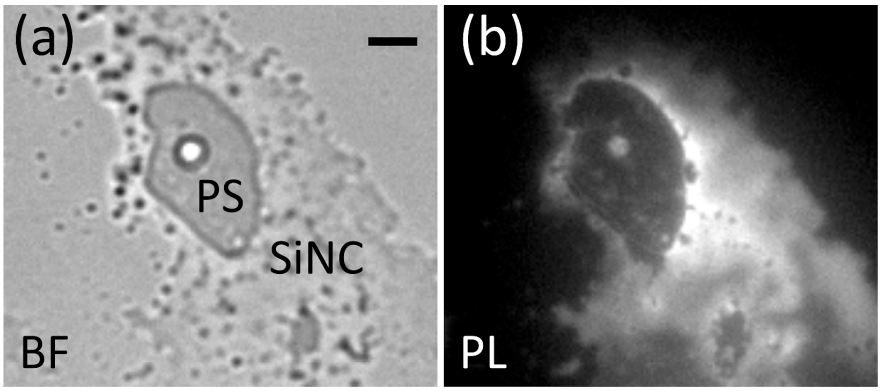

Figure 44: (a) Bright-field image (left, scale = 5 μm) and (b) PL image (right) of disordered polymer (PS) and nanocrystal phases formed through fluid-fluid phase separation in a dried toluene solution of polystyrene and a size purified SiNC fraction of comparable size.

suggesting that ordered nanocrystal packing might make a significant contribution to the L^{δ} term in equation (5.6). Although further study is warranted, it is conceivable that structural order could enhance the transport properties of the ensemble. Another possibility, however, is residual polymer between the nanocrystals.

5.2. Conclusion

In conclusion, the effects of particle packing on SiNC cluster PL have been studied. A significant PL enhancement is observed in films assembled from the fractions, which we attribute to an increase in quantum yield mediated by particle interactions in dense and possibly ordered clusters of monodisperse SiNCs. Brightening was observed independent of nanocrystal size, being most dramatic for smaller fractions that still exhibited high QY. Size uniformity ensures that the individual energy bands are well aligned, which will optimize electronic overlap in the wavefunction of neighboring nanocrystals. Our measurements further suggest that entropic order may play a significant role in this enhancement, although more work on this question is needed.

The measurements we present here suggest that brightening and bleaching in SiNC ensembles are directly linked to a dynamic increase and decrease, respectively, in the quantum yield of the ensemble. The latter effect is obvious, since the accumulation of long-lived dark states under continuous illumination will by definition lead to a reduced QY, particularly if the absorption cross section changes little between the 'on' and 'off' states (which would presumably be the case for Auger-like quenching and transport of any subsequently generated excitons). The time dependence of brightening, in contrast, is more complex. Almost immediately after the excitation is introduced, the rate constant k_{nr} must start to decrease. A 'fresh' ensemble must therefore respond instantaneously as a superposition of independent nanocrystals, but very shortly thereafter the influence of interactions emerges and the density of extended 'on' states increases accordingly. Evidence for this simple picture can be found in the photoresponse of clusters that have been briefly exposed to air, which show a short (1-10 s) interval of bleaching before the onset of brightening. The implications are potentially significant, however, since we demonstrate that the photostability and quantum yield of SiNC clusters can be controlled through self-assembly in monodisperse SiNC suspensions.

CHAPTER 6. BLINKING

Blinking, the cyclic on/off process exhibited by nearly all fluorophores, is a complicated subject of study and the dynamics are still not completely understood. Organic fluorophores such as conjugated dyes and fluorescent proteins have been studied since before the 1950s. However, nanocrystals have not been in the spotlight until relatively recently with their discovery in 1981. The discovery of SiNCs came even later at the beginning of the 1990s, and the interest and publications have been growing strongly ever since (Figure 3). Intense investigations into SiNC blinking didn't begin until the mid-2000s. Since then, there have been a variety of studies characterizing the statistics and dynamics that are at the source of this blinking [81–83].

Cichos et al. [75] performed measurements on single SiNCs and an ensemble of individuals under two illumination powers (1.3 μW, 4.6 μW). They found that the single SiNC blinking statistics match the ensemble's as long as enough events are collected. Both the on/off times are determined to follow statistical probabilities given by

$$p(t_{on/off}) = p_0 t^{-\alpha_{on/off}}, \tag{6.1}$$

where p_0 is a constant to normalize the first bin to one. The probability of the number of on-times is best fitted with $\alpha_{on} = 2.2$ (± 0.1) and is independent of the excitation power. However, the off-time distribution is found to bend from $\alpha_{off} = 1.3$ (± 0.05) for short off-times to $\alpha_{off} = 1.7$ (± 0.1) for long off-times at low excitation power. This bending is removed for the high excitation power where again $\alpha_{off} = 1.3$ (± 0.05).

The average on and off-times of the distribution can be calulated though the

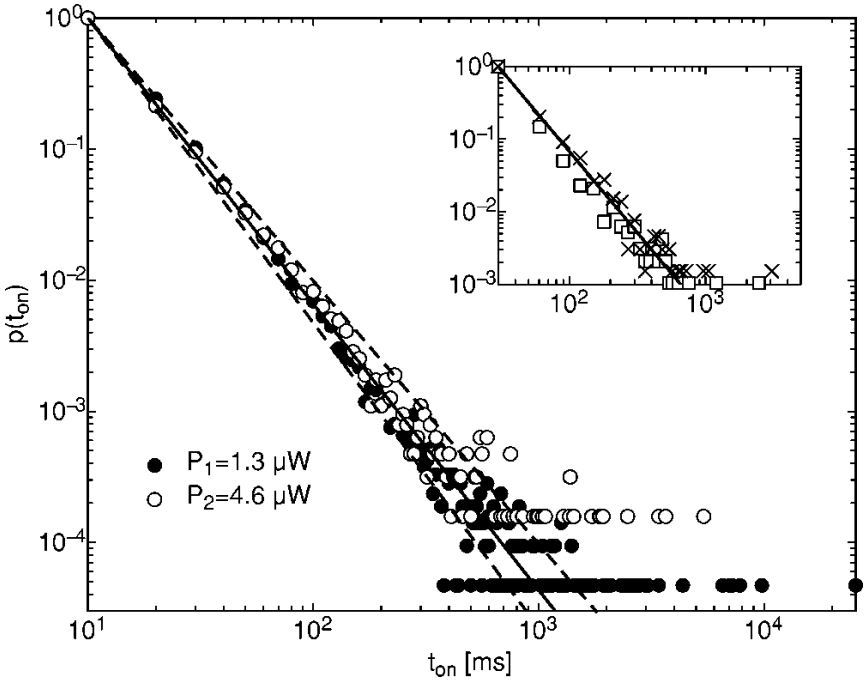

Figure 45: The probability curves of the on-time statistics for 100 silicon nanoparticles. The solid circle data points were excited at 1.3 μW; the open circles data points were excited at 4.6 μW. The solid line is a fit with $\alpha_{on} = 2.2$ and the dashed line with $\alpha_{on} = 2.1$ and $\alpha_{on} = 2.3$, respectively [equation (6.1)]. The inset displays data from two individual SiNCs which appear to follow the same power-law statistics as the ensemble. Reprinted figure with permission from [75]. Copyright (2004) by the American Physical Society.

integral

$$< \tau >= \int_{t_0}^{\infty} tp(t)dt \tag{6.2}$$

which diverges for $p(t)$ if $\alpha < 2$. This divergence suggests a mean off-time that increases with observation time and thus a long observation time will produce an average off-time ($< \tau_{off} >$) that goes to infinity. This is often what has been observed in the bleaching behavior of SiNC ensembles.

The number of studies on nanocrystals or quantum dots have been strongly weighted in favor of direct band gap materials such as cadmium selenide (CdSe), indium arsenide (InAs), indium phosphide (InP) and gallium arsenide (GaAs) to name a few. It is thus not accurate to quote results from a direct band gap study

and relate them to indirect results. However, in some studies, experimental data on different direct and indirect nanocrystals produce the same conclusion. For instance, the study on CdSe nanocrystals conducted by Peterson et al. [84] and the study on SiNCs conducted by Sychugov et al. [82] both show a quadratic dependence on power of the probability distribution which is theorized to come from biexciton formation and Auger ionization. It should be noted that these results are produced under much higher excitation power ($\sim$500 mW/cm^2) than that of Cichos ($\sim$3 μW/cm^2). Although external factors such as excitation power, composition, passivation and environment play a critical role in the blinking behavior, there appears to be a universality in the power-law statistical behavior. This power-law behavior suggests that the stepping between 'on' and 'off' states is not purely random.

The vast majority of nanocrystal studies, as well as the ones just mentioned, tend to focus on the PL statistics, dynamics and properties of single nanocrytals and large nanocrystal ensembles. There are considerably fewer studies on the development of PL behavior from one single nanocrystal to thousands of nanocrystals. Under normal isolated circumstances, it would not be expected that there would be changes, but one can imagine a system of nanocrystals brought together at distances where dipole interactions become important.

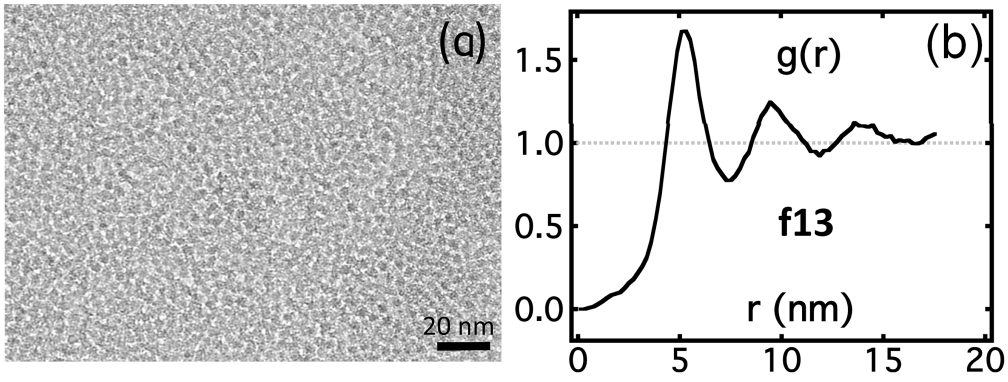

Figure 46: (a) Raw TEM image of a densely packed SiNC monolayer over air. (b) Typical pair-correlation function from such an image.

The pair-correlation function of a SiNC film produced from a fraction shows an average radial separation of 5 nm. This is the combined radii of two SiNCs ($d = 4$ nm) plus 1 nm. Since the stretched 1-dodecene passivating ligand is slightly over 1 nm, it can be said that the ligands from both nanocrystal are strongly overlapped. In this packing regime, dipole interactions should be important. Electron migration, tunneling or hopping is also proposed to occur. It only seems natural that the PL of the SiNC depicted in Figure 46(a) will be affected and the blinking statistics will become altered.

6.1. Experimental Procedure

Dilute SiNC fractions ∼0.01 mg/mL (SiNC/solvent) were spun cast on top of a cleaned high-quality quartz slide. Atomic force microscopy (AFM) (Agilent Technologies Model 5500) was used to confirm slide cleanliness. Fluorescence microscopy data were collected on a customized inverted Olympus IX71 microscope coupled to a ProEMB camera (LowNoise, 100ms bin time) (Figure 18). The sample was enclosed in a continuous flow nitrogen chamber on an optical table that was floated on an air hydraulic system to eliminate external noise (Figure 47).

For each sample, background fluorescence of the substrate was subtracted using the rolling ball background subtractor from ImageJ and the average standard deviation was calculated using 3 nonblinking areas. Fluorescence blinking was measured with the setup in Figure 47 for ten minute intervals. A bright field image was taken with reference clusters [see large cluster in Figure 48(a)] to map fluorescence to specific SiNC clusters of varied size by performing AFM.

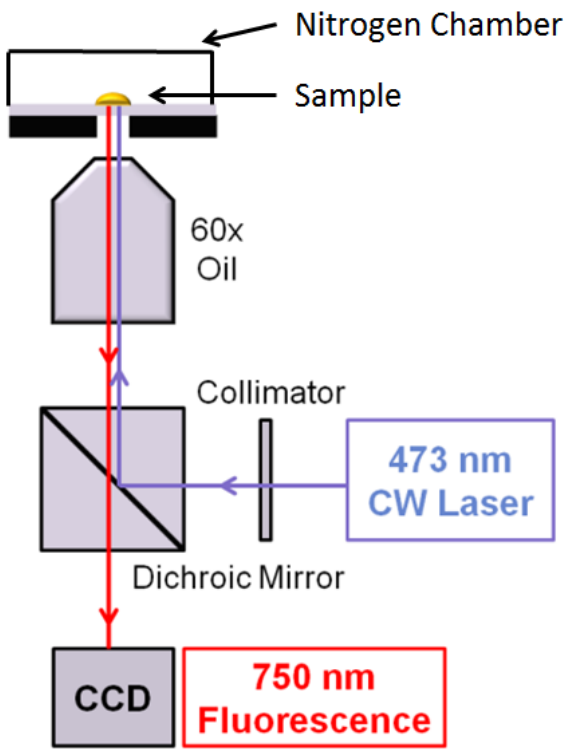

Figure 47: Optical setup used to collect blinking data.

Size determination was done by calculating the volume of each cluster (after tip radius and scan correction) and dividing by the volume of an average silicon nanocrystals with ligand (5nm) and then multiplying by the close-packing volume fraction of 0.74 for FCC and HCP geometries. After adequate fluorescence/AFM data have been collected, a linear correlation between SiNC cluster size and average intensity was found for low and high excitation powers (140 and 5000 W/cm^2) for both pure and AP SiNC samples (Appendix A) (Note: both powers are much larger than those used in the Finite Extinction Length of Excitation in Silicon Subsection).

Using this calculated linear relationship between average intensity and number of SiNCs, analysis began by collecting blinking videos. Multiple Matlab programs were edited and written to simultaneously analyze fluorescence blinking and autocorrelation, and the results were matched to SiNC cluster size. This large and exhaustive

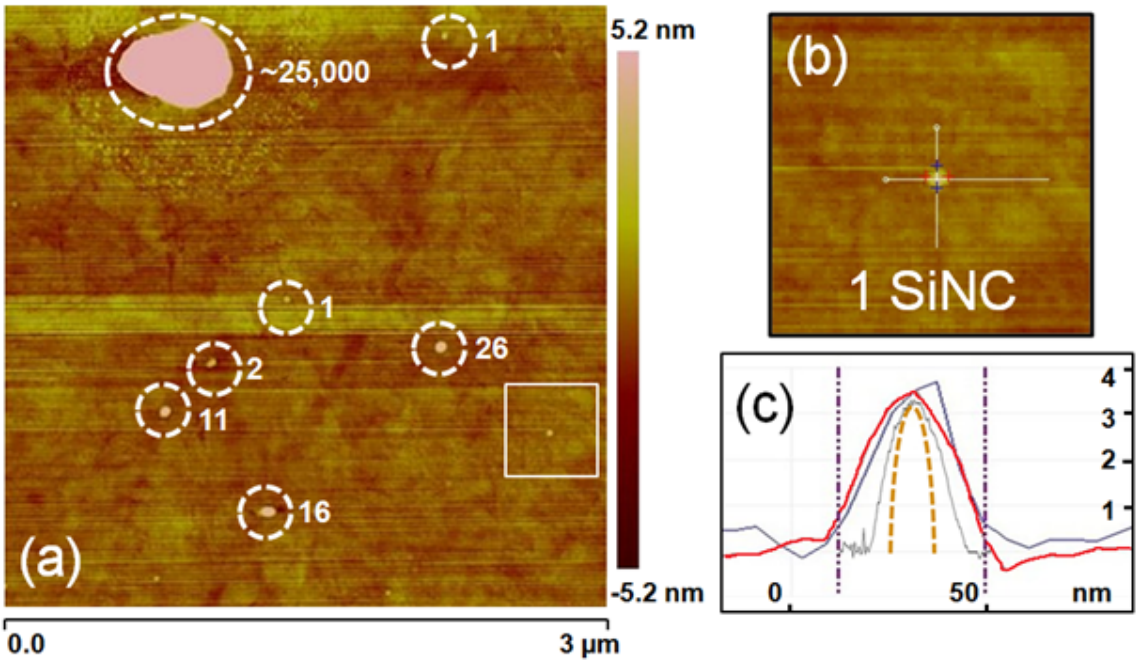

Figure 48: (a) AFM scan of SiNCs clusters with a large reference cluster of $N \sim$ 25,000. (b) Enlarged view of white square window in (a). (c) Height profile of perpendicular x (red) and y (blue) scans shown in (b). The expanded lateral dimension is due to the large area scanned and AFM tip radius and becomes diminutive with nanometer size scans (gray curve). With corrections, the SiNC profile is given by the dashed brown line.

program can be viewed in Appendix B.

6.2. On-Time Statistics

As of yet there is still no clear physical picture on the blinking mechanism and the universal power law (Lévy statistics) that is observed. It is believed that either the photoexcited electron or hole becomes trapped in a nanocrystal surface state or tunnels into a nearby environment. The charged core leads to rapid nonradiative recombination of subsequent excitons though Auger processes [70].

The signal from a variety of SiNC cluster sizes is shown in Figure 49(a). As the SiNC cluster size increases, the PL intensity improves dramatically until $N = 300$ where the cluster is large enough to visually see a transition from collective blinking

behavior to ensemble bleaching. Figure 49(b) shows the intensity time trace of a cluster with 132 SiNCs. The red lines demonstrates the threshold used to determine the difference between 'on' and 'off' states: $I_{threshold} = b_{dark} + 1.3\sigma_{dark}$ where b_{dark} is the background collected in the absence of light and σ_{dark} is the standard deviation of background fluctuations. The sigma prefactor of 1.3 was chosen after scrutinizing numerous videos to verify that the coded Matlab computer program's collected data match the blinking data visually recognized. Though the specific value of α_{on} [equation (6.1)] is known to slightly depend on the binning time and threshold [85], the overall trends appear the same. In Figure 49(c), the intensity traces of (a) have been digitalized according to the threshold. The digitalized traces were used to calculate the on and off-times for all data.

Figure 50 shows the calculated on-time probabilities for varied cluster sizes and powers for both the AP and fractioned material. The on-times have been normalized by the first bin. Focusing on Figure 50(a), the on-time probability for monodisperse fractioned SiNC samples with N = 1, 16, 300 cluster size is shown. These samples were excited at low power ($\sim$140 W/cm^2) with 473 nm laser light. The fits are given by solid lines which are (truncated) power laws. As with graph (b) and (c), there is a clear trend as the SiNC cluster increases in size. As the clusters become larger, the probability of longer on-times increases. There is no surprise in this result until we consider looking at the results of adding 16 and 300 individual blinking data sets together and then plotting these probabilities. The light red (N = Summed 16) and light blue (N = summed 300) curves show distinctly different trends than the clusters given by the corresponding dark red and blue lines. This means that the blinking dynamics and on-times of summed individual SiNCs differ from those of clustered SiNCs. In the case of (a), this difference is a higher probability of longer on-times for the clusters and strongly suggest that this enhanced average on-time is a result of

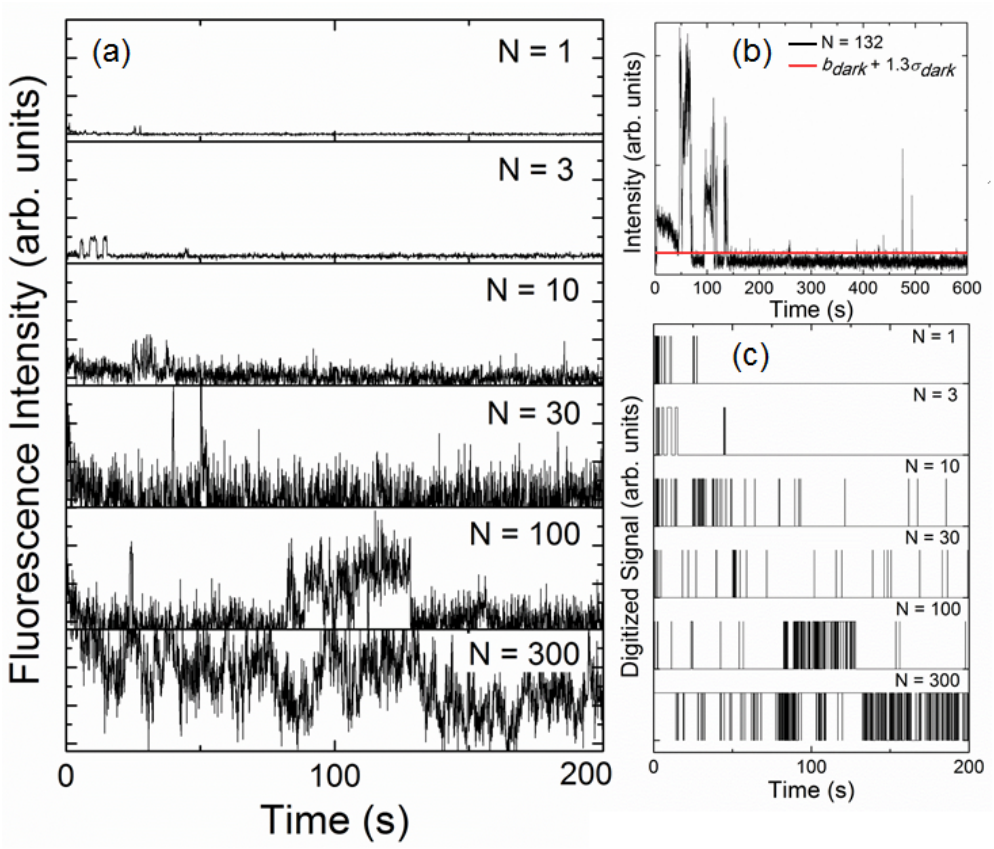

Figure 49: (a) Typical time-dependent PL traces at varied cluster size N. (b) Intensity time trace of an $N = 132$ cluster and the corresponding PL threshold used to bin on-times. (c) The binned fluorescence signals based on this threshold.

particle-particle interactions.

As evident from the curved lines, some of the data fits are truncated power laws which occur predominately for summed individual data. A truncated power law given by

$$p(t_{on/off}) = p_0 t^{-\alpha_{on/off}} e^{\frac{-t}{\tau_{on/off}}} \tag{6.3}$$

has been observed in recent examinations of CdSe nanocrystals [70, 84]. The data appear to follow the power law initially but then drop off at longer times, most noticeably for individual SiNCs and those excited at high power. This modified power law is not well understood. The data here show an increase in dropoff with

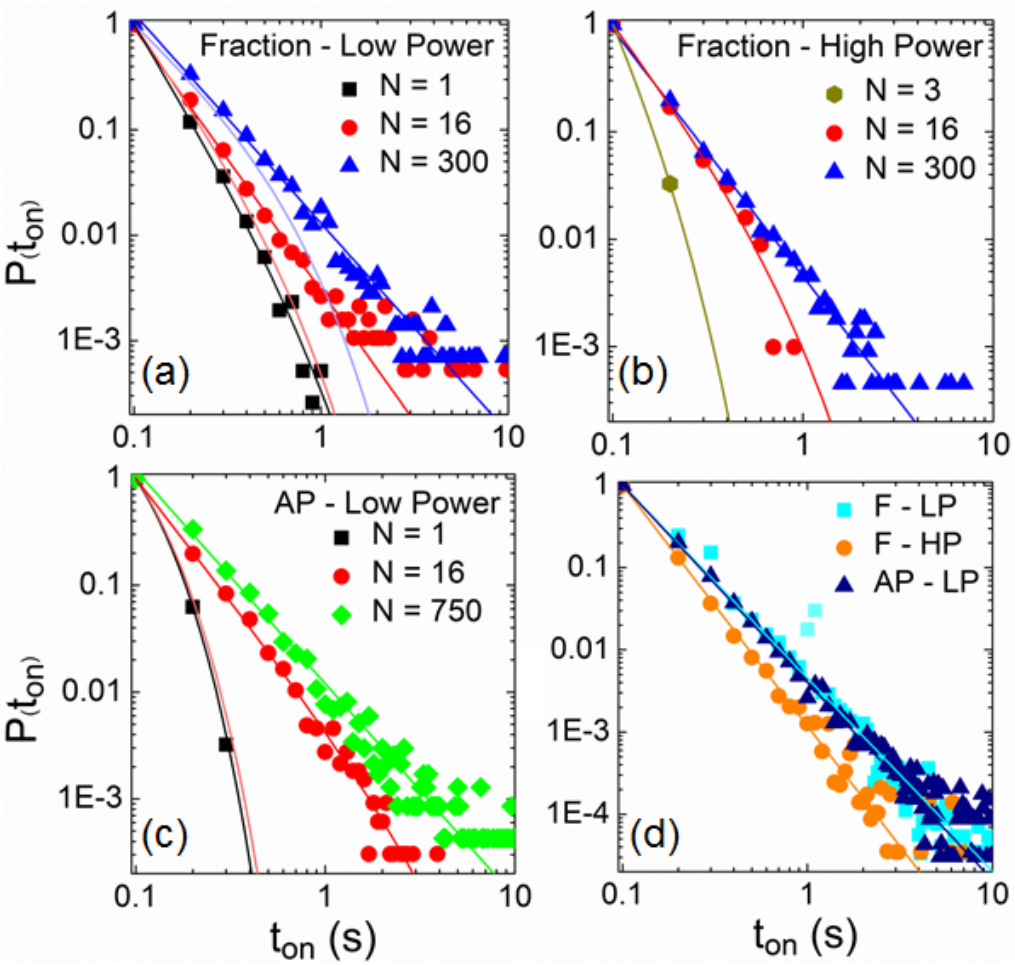

Figure 50: On-time statistics compiled from a collection of clusters from a fraction with average size $N = 1$, $N = 16$ and $N = 300$ at low (a) and high (b) power. The data transition from a pure power law to a truncated power law with increasing power. (c) On-time statistics for a collection of AP clusters with average size $N = 1$, $N = 16$ and $N = 750$ at low power. (d) A comparison of the on-times for fractions at low and high power and AP at low power. These data include all cluster sizes.

an increase in power. This suggests that there may be a saturation effect due to multiple exciton generation or SiNC surface modification and trap state creation at high fluence. These data are quite recent, and ongoing investigations will try to ascertain the true reason behind this effect. However, the probability falloff and truncated power law are reduced as the clusters become larger. A return to a pure power law for large clusters bolsters the idea that clusters with close-packed SiNCs

produce interparticle interactions that affect PL.

In graph (d), the blinking probability distribution for all collected samples is plotted. There is a noticeable decrease in the average length of on-times for the high power (~5000 W/cm^2).

Table 1 gives the values of the on-time power exponent (α_{on}) and truncation time (τ_{on}) for Figure 50. From these data we can conclude an increase in the probablility for longer on-times for clusters and lower excitation power.

Table 1: On-time Probability Values

Conditions	Population Type	Population Number	α_{on}	τ_{on} (s)
F-LP	Cluster	1	2.806	0.580
		16	2.490	
		300	1.990	
		Combined	2.300	
	Individual	16	2.346	0.400
		300	1.475	0.400
		Combined	2.300	
F-HP	Cluster	3	2.875	0.070
		16	2.250	0.500
		300	2.300	
		Combined	3.930	
AP-LP	Cluster	1	0.042	0.037
		16	2.250	3.000
		750	2.000	
		Combined	2.260	
	Individual	16	0.430	0.043

6.3. Mean and Max Times

More insight into nanocrystal blinking can be gained by studying the average on and off-times. Figure 51(a) and (c) give the mean times for our three samples including the summed individual results. For all samples, the mean on-time increases with cluster size while the mean off-time decreases with size. This correlation is very

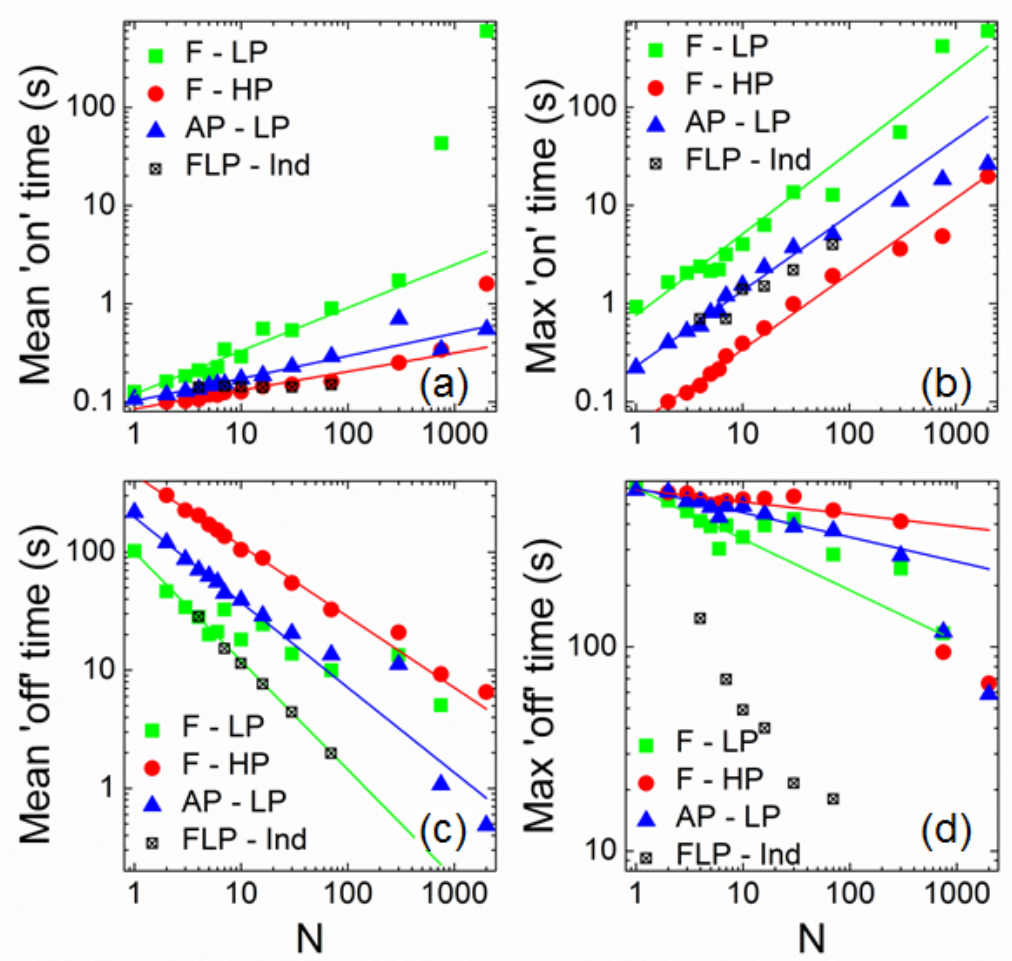

Figure 51: The mean and max on-times (a,b) and off-times (c,d) versus cluster size N for three scenarios; F-LP, F-HP and AP-LP. Best fit power law curves are given to aid the eye.

intuitive and expected. However, it appears these results do not correlate with the probability curves [Figure 50(d)] in that the low-power fraction (F-LP) and low-power AP (AP-LP) mean on-times are clearly different here. The F-LP shows a longer average on-time with increasing cluster size than the AP-LP sample. It was recently found that the data collection process may create a slight cluster size bias. Preliminary results that correct for this bias show an increase in the probability of on-time for the F-LP sample which coincides with the longer mean on-time observed. This resulting increase in mean on-time is even greater when compared to the summed

individual SiNC sample. Also, the max on-time for the F-LP is substantially larger than all other samples.

Even though there is substantial noise for graph (c) and (d), the off-times are smallest for the F-LP and the trends agree with the on-time graphs. Physically, these data tell a story. An illustration of a scenario of the blinking of each sample is given in Figure 52. A F-LP blinking cycle is shown where the mean and maximum on-times are longer than those of the F-HP and AP-LP samples.

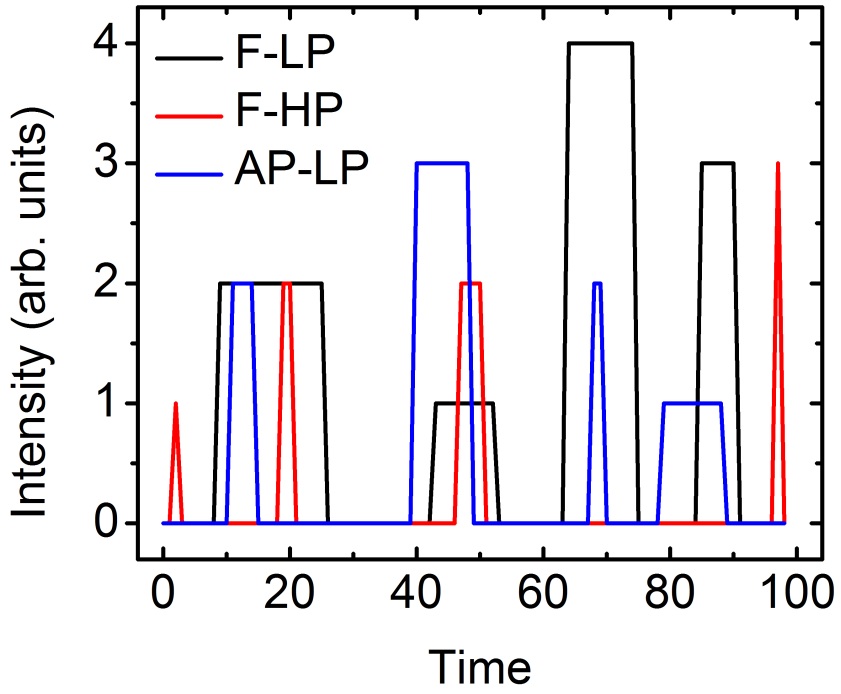

Figure 52: Example blinking time traces of the three samples F-LP, F-HP and AP-LP following the data given in Figure 51.

Unlike the average intensity which shows a linear increase with cluster size, the average total on-time and integrated intensity show a power law increase with cluster size. This is true for all samples as well as the summed individual samples. Not only is there an improvement in the average on-time for the F-LP sample, but there is a substantial increase in average total on-time. This is probably the most

important result as it demonstrates an increased PL stability as a result of using centrifuged, monodisperse SiNC fractions. The stability further increases under low-power excitation.

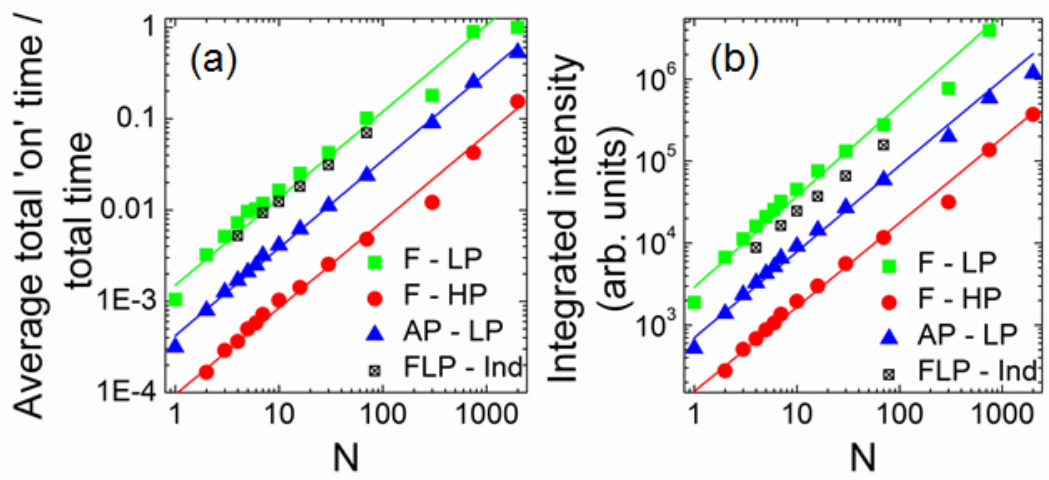

Figure 53: (a) The fraction of total observation time spent in the 'on' state as a function of cluster size for the three scenarios. (b) The average integrated intensity versus cluster size. Best fit power-law curves are given to aid the eye.

A possible explanation for the F-LP sample's longer on-times lies in its ability to have higher packing density. According to a dynamic trap model [54], trapping may be turned off by making the traps energetically inaccessible: the trap state's energy becomes higher than the excited state's energy. The nearby or surface potential of a SiNC emitter becomes charged as a result of an excited neighboring SiNC. This potential prohibits the stimulation of a second electron (hole) and the SiNC remains in a bright state. The trapping can resume when the SiNC emitter returns to a neutral state. It is this reduction in trapping from close, interacting SiNCs that might enhance the PL for the F-LP sample.

6.4. Autocorrelation

The fluorescence was also scrutinized through analysis of its correlation properties. The autocorrelation function is defined as

$$c(\tau) = \frac{< I(t)I(t+\tau) >}{< I^2(t) >} \tag{6.4}$$

where $I(t)$ is the fluorescence intensity at time t. The averages are performed over the entire observation time and the 'lag' time is given by τ. The autocorrelation function gives a measure of the interactions involved in the fluorescence of the SiNCs. A completely random process will quickly evolve to $c(\tau) = 0$. Fluorescence should naturally evolve as a random process but often there are outside influences which increase the self correlation. In the case of high self correlation, a fluorescing particle will be much more likely to exhibit fluorescence at the next time step. These outside influences are assumed to be related to nearest neighbor particles in the case of our SiNC clusters. Therefore, a highly interacting cluster will be strongly correlated and the autocorrelation function will be not vary much from one [$c(\tau) \approx 1$].

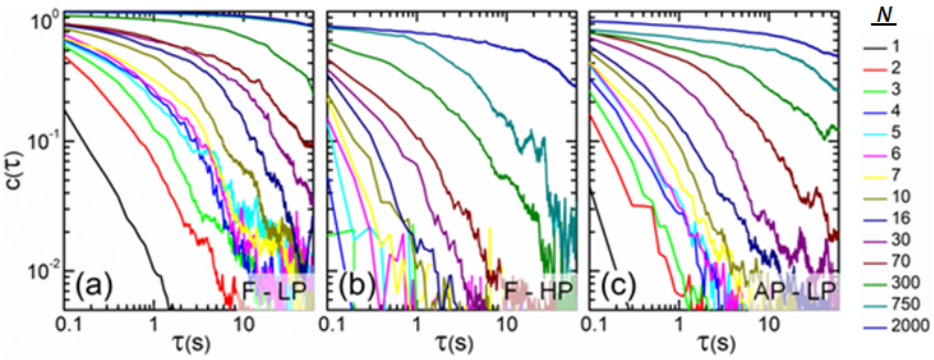

Figure 54: Autocorrelation function versus time for clusters of varied N. The data are for fractions at (a) low and (b) high power, and (c) shows the AP material under low excitation power.

The autocorrelation graphs above confirm the previous trends. The F-LP

sample shows the highest autocorrelation for the longest time with increasing cluster size followed by the AP-LP and then by the F-HP. The normalized autocorrelation values at $\tau = 1$ are given in Figure 55. One can see an obvious jump in blinking correlation as the cluster size increases. Again, it is the F-LP data that exhibit the largest autocorrelation values. This resonates the increased correlation and interactions promoted by the self-assembly of clusters from monodisperse fractions. We are currently working on developing a theory and model which can help us understand the true nature behind this modified PL response.

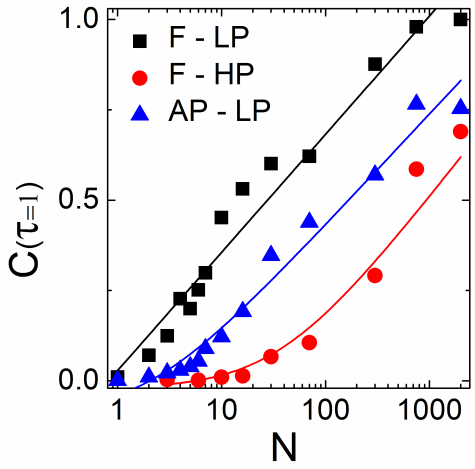

Figure 55: Values of the autocorrelation function at $\tau = 1\ s$ for the three different scenarios. Solid lines are logarithmic fits to guide the eye.

6.5. Conclusion

Our data show an increase in on-time probability with increasing SiNC cluster size for all three scenarios: F-LP, F-HP and AP-LP. We see a substantial improvement in cluster on-time versus the summed individual on-time. When we combine data from all cluster sizes, we see that the fraction and AP on-time probability are similar at low power, but there is a dramatic decrease in longer on-times with an increase in power. This is consistent with our previous findings, where cluster 'brightening'

interval increased with decreasing power and 'bleaching' increased with increasing power. The mean and maximum on-times as well as the percent of total on-time and integrated intensity all increased with SiNC cluster size for all samples. However, we see a more substantial increase with the fraction clusters compared to the AP clusters. Combining the results from all collected data paints an overall picture of how the blinking is affected by using monodisperse nanocrystals to form clusters. The close-packed clusters made from fractions interact strongly with each other. This interaction produces longer, brighter on-times which contribute to the overall increase in emitting time and intensity over the observation window. The autocorrelation function shows that the fluorescence trajectory of a cluster correlates with itself much longer for larger clusters, which is in agreement with the enhanced on-times of large clusters and substantiates this notion of SiNC-SiNC interdependence.

CHAPTER 7. TEMPERATURE DEPENDENCE OF SILICON NANOCRYSTAL FILMS AND POLYMER NANOCOMPOSITES

There has been a small but significant amount of recent work on the temperature dependent PL from SiNCs dispersed in a variety of environments [86–88]. There are numerous potential applications for polymer nanocomposites, especially biomedical applications in the case of SiNCs, and thus it is important to understand not only pure but composite films. In general, the intensity and lifetime both increase with decreasing temperature as the influence of nonradiative effects decreases, while the emission peak shifts because of thermal changes in the bandgap [86–88]. However, only a coarse picture of how the response varies with nanocrystal size has emerged and this has focused primarily on the influence of quantum confinement [86, 87]. As was previously described, there are also many-body effects in SiNC ensembles [34, 89] that can modify the collective optical response and temperature dependence though nanocrystal size and polydispersity [34, 89].

7.1. Experimental Procedure

As a polymer matrix, we use cross-linked polydimethylsiloxane (PDMS) because of its widely established biocompatibility and biodurability, and we focus on the temperature range relevant to cryomedical applications that employ liquid nitrogen (80 to 300 K).

For the PDMS, a 10:1 by mass ratio of monomer to hardener was used for the films. Resin and catalyst were combined in a vial and stirred for 5 min. A small amount ($\sim$100 mg) of mixed PDMS was placed in another vial and then combined with toluene to form a 2 % by weight PDMS/toluene solution. This parent solution was then used for all PDMS/SiNC samples. Composite and pure SiNC films were

drop cast from toluene or hexane, respectively, onto treated coverslips, and, in the case of PDMS, annealed under vacuum at 40 °C for 1 hour to promote cross-linking.

Optical measurements were generated on a setup similar to the one used previously but on an upright Olympus microscope. All optical measurements were thus performed in transmission. Measurements were done as a function of temperature between 80 and 300 K using a Linkham BCS196 CryoBiology stage integrated into the optical train.

7.2. Results

The peak PL energy response to changes in temperature and fraction number are graphed for pure and SiNC-PDMS films. As described earlier, SiNC fractions are the 200 μL aliquots separated from the parent material after DGU and represent monodisperse samples of varying sizes.

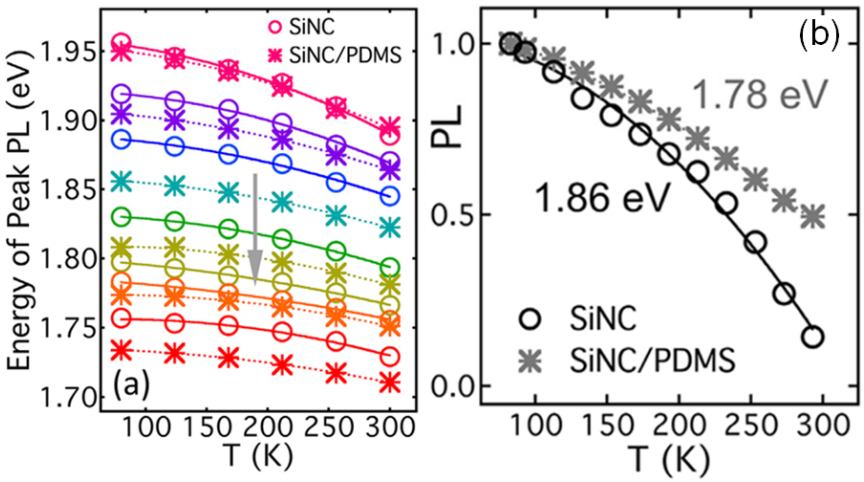

Figure 56: (a) Temperature dependence of the energy of peak PL for both pure SiNC fractions and PDMS nanocomposites, where the arrow indicates the direction of increasing size. (b) Temperature dependent PL for a pure SiNC fraction (1.86 eV peak emission) and a fraction in PDMS (1.78 eV peak emission), both normalized by the emission at 80 K.

Figure 56 shows how E, the energy of peak PL, evolves with T, where the excitation power was maintained below 50 mW/cm^2 to avoid low-T saturation effects

associated with PL lifetime [87]. The PL peak shifts to lower energy with increasing T because of thermally induced changes in the quantum-confined energy levels, where such changes can depend on lattice spacing, strain, and electron-phonon coupling [88, 90].

Thermal changes in the bulk silicon band gap occur predominantly through thermal expansion and electron-phonon interactions [88]. For quantum dots in general [90], thermal expansion can affect $E(T)$ through its dependence on lattice spacing a, with $(\partial E/\partial T)_a = (\partial E/\partial a)(\partial a/\partial T)$. However, such a contribution is typically weak for quantum confinement because of the magnitude of $(\partial E/\partial a)$ [90]. Thermal expansion of the quantum-confined envelope will likewise be a small effect [90], since the thermal expansion coefficient of silicon changes sign near 100 K but is otherwise small ($\sim 10^{-6}K^{-1}$) [58]. This leaves electron-phonon coupling as the dominant factor, similar to what occurs in the bulk [87, 88]. A rigorous expression for $E(T)$ does not exist for SiNCs, so we adopt the approach of Bludau et al. [91] and fit $E(T)$ to a second-order polynomial [curves, Figure 56(a)], where the constant term models the 0 K bandgap (E_0). In all cases, the PL intensity increased monotonically with decreasing temperature [Figure 56(b)]. This result is due to the increase in lifetime and proportional QY as the temperature decreases.

Turning to the the lifetime behavior, Figure 57(a) and (b) suggest that the dependence of the exponent (α) and lifetime (τ) on R and T are the same for for both the pure and polymer nanocomposite sample. In light of the monodisperse nature of the fractions and the insensitivity of α to sample type, the data presented here support an intrinsic origin as suggested by Delerue et al. [60], with the $\alpha \to 1$ trend at low T reflecting a decrease in the number of available phonon modes upon cooling. Figure 57(c) shows the τ trends with size at low and high temperature. Although otherwise similar, an increase in τ with decreasing R is clearly evident for

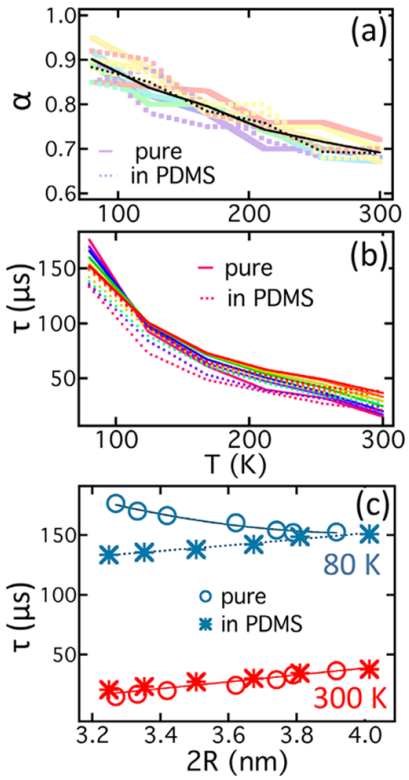

Figure 57: (a) Exponent α as a function of temperature for pure SiNCs (solid) and PDMS nanocomposites (dashed). The black trace is the fraction average. (b) Lifetime versus T for pure SiNCs (solid) and PDMS nanocomposites (dashed). The colors represent the different size fractions [found on horizontal axis of (c)] and the label for the horizontal axis in (a) is the same as that for (b). (c) Lifetime as a function of nanocrystal size for pure SiNCs and PDMS composites at 300 and 80 K. Error bars are the size of the markers.

the pure SiNC films at 80 K [Figure 57(c)].

A handful of recent studies have focused on the PL of size purified SiNCs [31, 34,56], and an increase in lifetime with increasing nanocrystal size can be anticipated up to the characteristic size corresponding to the optimum quantum yield. A striking exception to this trend is the low temperature behavior exhibited by the pure SiNCs, which show an increase in lifetime with decreasing size. A hint of this trend can also be seen in recent cryogenic measurements on size polydisperse solution-synthesized SiNCs [86], although only two nanocrystal sizes were examined in that study. In the simplest view, the quantum yield is $\Phi = k_r/(k_r + k_{nr})$, where again k_r and

k_{nr} are equilibrium constants associated with radiative and nonradiative relaxation, respectively. The lifetime, equation (4.4), is $\tau = (k_r + k_{nr})^{-1}$ and the radiative lifetime is $\tau_r = k_r^{-1}$, with $\tau_{pure}/\tau_{PDMS} = (k_r + k_{nr})_{PDMS}/(k_r + k_{nr})_{pure}$. The assumption that k_r is intrinsic to an individual nanocrystal implies

$$\frac{\tau_{pure}}{\tau_{PDMS}} = \frac{\Phi_{pure}}{\Phi_{PDMS}} = \frac{1 + (k_{nr}/k_r)_{PDMS}}{1 + (k_{nr}/k_r)_{PDMS}} \tag{7.1}$$

with the behavior in Figure 57(c) suggesting that there is a low-temperature decrease in the nonradiative rate constant $(k_{nr})_{pure}$ with decreasing size. For both sample types, a decrease in k_{nr} upon cooling leads to an increase in τ, but our data suggest that the low-T decrease in k_{nr} is more pronounced for the pure SiNC films at smaller nanocrystal diameters.

A feasible explanation for this difference is the influence of interactions, which appear to reduce nonradiative rates in SiNC clusters. A somewhat related but different trend has recently been predicted by many-body theory, where room-temperature exciton transport rates and PL relaxation rates both increase with decreasing nanoparticle separation and decreasing nanocrystal size [89]. Such computational schemes are better suited to smaller SiNCs [89], however, and are inconclusive at the close separations of interest here. They also use local field factors to approximate the screening of interdot Coulomb interactions and neglect any role for dark trap states. Here, insight into the origin of the effect comes from its notable absence in the PDMS nanocomposites. The important differences are the tendency for packing order in the pure SiNC films and the presence of residual interfacial polymer in the nanocomposite clusters. Although more research is clearly warranted, both of these have the potential to influence the collective optical response through interactions, particularly at low temperature. Also, the PDMS nanocomposites show significant phase separation between the nanocrystals and the polymer matrix (Figure 58), suggesting that the

same morphological factors that influence room-temperature PL 'brightening' might also influence the low-temperature PL relaxation behavior reported here.

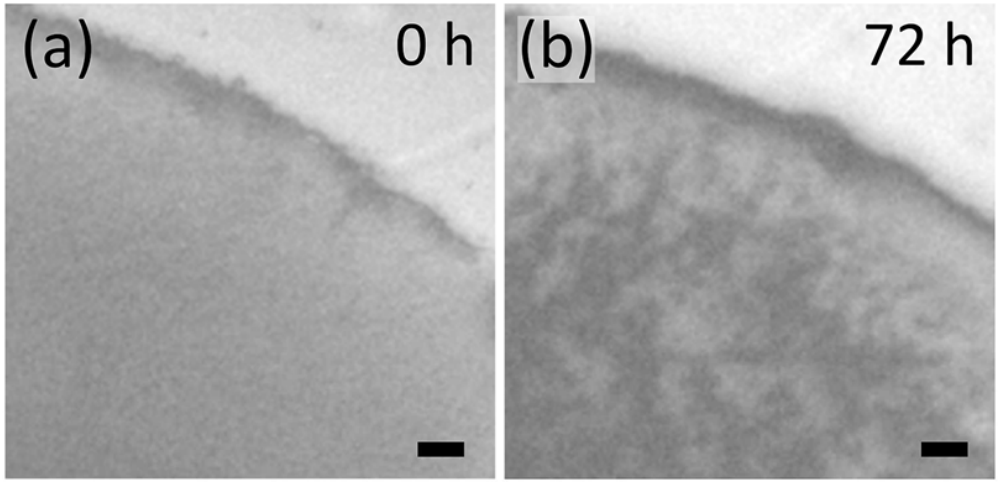

Figure 58: Reflection optical micrographs of the sample boundary at (a) 0 h and (b) 72 h after curing (50 μm scale).

7.3. Conclusion

We have characterized the temperature dependent PL of highly monodisperse size-purified SiNCs in pure nanocrystal films and PDMS nanocomposites from room temperature down to 80 K. We find behavior consistent with weaker interparticle/environmental coupling in the PDMS nanocomposites and stronger interparticle effects in the pure SiNC films, but the overall behavior is in agreement with the trends that would be expected based on the thermal behavior of bulk silicon and the influence of quantum confinement.

The lifetime for both samples increases with decreasing temperature, but an unanticipated low-T increase in τ with decreasing nanocrystal size in the pure SiNC films is suggestive of an increase in ensemble quantum yield mediated by nanocrystal interactions. A feasible explanation for the absence of this enhanced lifetime in the PDMS nanocomposites would then be the influence of intervening polymer on the interaction of neighboring nanocrystals.

CHAPTER 8. DRYING DYNAMICS OF POLYMER-SILICON NANOCRYSTAL MIXTURES

The physics that governs the drying of an isolated droplet is remarkably complex, and yet the practical implications of this everyday process can be technologically profound [92]. A contemporary example of particular relevance is inkjet printing, whereby fluid mixtures of particle, polymer and solvent are cast as droplets and subsequently dried for a range of coating and assembly applications [93]. A significant challenge associated with this process is the need to tame, or in some instances exploit, the familiar 'coffee-ring' effect [94]. This well-studied drying instability is governed by capillary flows that generate differential evaporation rates across the free surface of a droplet, resulting in an edge-directed flow that transports dispersed particulates, or even emulsions [95], toward the contact line in an irreversible fashion. A familiar example is the dark ring left behind when a drop of coffee dries on a hard surface, the namesake phenomenon of the effect.

'Pinning' or fixing of the contact line - the closed contour of liquid-solid-vapor coexistence that comprises the edge of a drying droplet on a wetting surface - is critical to the emergence and control of the coffee-ring effect [96]. Particle shape has also recently been shown to play an important role [97, 98], as has the fluid-solid contact angle and the overall affinity of the liquid droplet to the substrate [99,100]. For colloidal nanocrystals dispersed in organic solvents, enhanced or reduced substrate affinity can have a significant impact on the ability to cast homogeneous droplets and coatings from nanocrystal suspensions and ternary solvent-nanocrystal-polymer mixtures [34, 101], while the morphology of the nanocomposite can, in turn, impact the PL properties of the nanocrystal ensemble [34, 101, 102]. Texture, porosity and temperature have likewise been demonstrated to be important substrate parameters that can enhance or suppress the effect [103–105].

When the contact line is pinned, the rate of solvent removal [106], the size of the droplet [107], and the amount of surfactant [108] can further influence the nature of the instability, and it has been suggested that the onset of Marangoni flows acts to counter the edge-directed transport of particles, which in turn can lead to a more uniform distribution of particulates in the final dried state [108]. For microscopic polystyrene beads dispersed in water, the recent use of optical coherence tomography (OCT) to map the full 3D flow field supports the view that weak Marangoni stresses can, in some instances, generate eddies or secondary flow fields in aqueous colloidal suspensions [109]. In general, the instability can be suppressed for micron-sized particles if the solvent is removed faster than the rate of particle diffusion [107].

The situation can be even more complex when the solvent evaporates faster than water (e.g., toluene) or the suspension contains particles that are nanoscopic in size (e.g., polymers or nanocrystals). A systematic study of the inkjet printing of high-molecular-weight ($M_w \geq 80$k) polystyrene (PS) from a variety of solvents, for example, always produced films with a ring deposit, but the instability could be suppressed by using a mixture of solvents with disparate boiling points [93]. In contrast, another recent study concluded that the addition of a water-soluble polymer (polyethylene oxide) to an aqueous suspension of micron-sized silica beads can suppress the effect through a combination of elevated viscosity, which slows particle transport, and enhanced Marangoni flow [103]. Although we are not aware of a general rule, the potential for generating significant surface-tension gradients in drying droplets of volatile solvents could favor Marangoni effects with higher flow rates, while particle diffusion rates for nanoscale objects would also be higher. The overall change in Peclet number is what is significant, and the complexity of the effect implies that any given system has the potential to behave uniquely, making *a priori* generalizations difficult.

Nonetheless, the ability to tune or control the coffee-ring effect will be critical for applications that seek to print nanocomposite features from solution [110, 111] or exploit evaporative self-assembly as a route to engineering structured films and coatings [7, 112]. The tendency for nanoparticles to condense at the contact line, for example, offers a natural route to printing conductive 'lines' or wires from metallic nanoparticle solutions [113], but the geometry of the deposition needs to be controlled in a useful fashion. In this regard, the transient nature of the concentration and flow fields adds an additional layer of complexity, with one recent study demonstrating an order-disorder transition within the deposition layer [114].

The scenario for polydisperse suspensions and mixtures has particular relevance to contemporary applications, such as the blending and printing of polymers and nanocrystals, and the instability could potentially impact the processing of multiphase nanofluids [18]. Polydisperse colloids, for example, can exhibit size fractionation within the contact line [115–117] and viscous fingering within the ring [118], while one recent study examined the deposition profile during the spinodal decomposition of colloid-polymer mixtures [119]. The overall pattern was controlled by Marangoni eddies which have recently been linked to excess surfactant [120] with entropic phase separation into colloid-rich flow-aligned domains [119]. These observations are in remarkable agreement with simulations of spinodal decomposition in drying polymer-blend solutions, where lateral phase separation at the fluid-air interface 'templates' segregation within the bulk of the film [121]. Such simulation results are intimately linked to diffusive dynamics, and the regular patterns are a generic feature of diffusive phase-separation fronts, where the domains can orient either parallel or orthogonal to the front [122, 123].

The coupling between the coffee-ring effect and liquid-liquid phase separation is examined for ternary mixtures of volatile solvent, polymer and colloidal nanocrys-

tal. Specifically, we study mixtures of toluene, polystyrene and SiNCs using optical techniques to resolve the morphology of the drying front for varied molecular weight of the polymer. Our results demonstrate that the size of the PS has a significant impact on the phase behavior and character of the drying instability, and we relate our observations to lattice-Boltzmann simulations, a free-volume theory of the equilibrium phase behavior and the observed nature of the flow field at the contact line. Our findings inform a deposition process that reduces the influence of drying instabilities for low-molecular-weight polymers, while isolating the effects of phase separation for medium and high-molecular-weight polymers. This has significant implications for applications that seek to print homogeneous or textured patterns from multicomponent solutions of nanoscale objects, and our results set the stage for more detailed and predictive computational models of drying instabilities in multiphase complex fluids.

8.1. Results

8.1.1. Experiments

Polystyrene (PS) standards of weight-averaged molecular weight (M_w) 213,600 (denoted 200k, polydispersity index = 1.01), 18,100 (denoted 18k, polydispersity index = 1.01) and 2,400 (denoted 2.4k, polydispersity index = 1.07) were obtained from Sigma-Aldrich, and dilute PS suspensions were prepared in toluene, a good solvent, at varied PS:SiNC mass ratio at specific mass densities c_{PS} and c_{SiNC}. The radius of gyration, R_p, of each polymer in toluene is 1.3 nm (2.4k), 4.3 nm (18k) and 19 nm (200k), and the polymer overlap concentration, c^*, is 12 mg/ml (200k), 85 mg/ml (18k) and 425 mg/ml (2.4k) [123]. These mixtures were then cast as 5 μL droplets on clean untreated glass slides, and time-resolved bright-field, PL and phase-contrast optical microscopy and time-resolved PL spectroscopy were used to

monitor the drying front. Particle tracking was also used to map the flow field near the front.

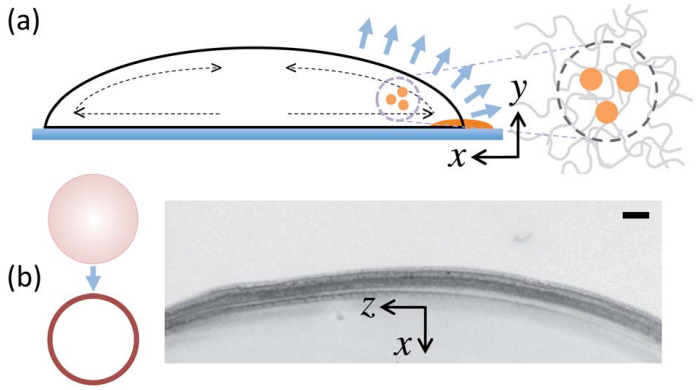

Figure 59: (a) Schematic side view of a droplet with the flow (x) and gradient (y) directions as indicated. We define the positive flow (x) direction as toward the droplet center. (b) Top view of the droplet, which leaves a ring when it dries if the contact line is pinned. The micrograph (right, 50 μm scale) indicates the positive flow (x) and vorticity (z) directions.

The geometry of the experiment is shown in Figure 59(a), with the flow (x), 'gradient' (y) and 'vorticity' (z) directions as indicated. Measurements were also performed on all of the pure components. Contact-line pinning always occurred in the presence of SiNCs, suggesting that the nanocrystals have a significant affinity for the glass substrate. Such pinning was never observed for the pure polymer solutions, however. The typical ring pattern of a dried deposit is shown in Figure 59(b), and the varied morphologies observed at the contact line are shown in Figures 61, 63 and 64. In the x-y plane, suspended solids typically travel out to the edge at the substrate and back toward the center at the free surface, although this can get obscured due to localized circulation or eddies.

Liquid-liquid phase separation has a significant impact on how the polymer-nanocrystal mixtures dry and we are primarily interested in how this thermodynamic instability couples to the hydrodynamic instability of the coffee-ring effect. To measure the equilibrium binodal curves, we developed a transient technique ideally suited

to the small sample volumes of interest. A rectangular microcapillary 520 μm by 250 μm in cross section, open at both ends, was filled with an initial PS/SiNC/toluene solution, and the average local PL immediately measured along the length of the tube. The capillary was then allowed to sit for several hours while the solvent slowly evaporated. Drying occurs through a pinning of the gas-liquid interface at one of the open ends, with a mobile liquid-gas interface at the other end that then moves down the capillary as the solvent evaporates. A particle concentration gradient develops and phase separation occurs in a narrow band at some point along the tube (left and middle inset, Figure 62). The ratio of the total PL at the point of phase separation to that of the initial mixture gives a measure of the SiNC concentration at the stability limit, and the known PS:SiNC ratio of the initial mixture then gives the corresponding PS concentration. While this approach is somewhat crude, it provides a consistent measure of the binodal for each molecular weight of the polymer.

8.1.2. Lattice-Boltzmann Simulations

The coffee-ring effect underlies all of the phenomena of interest here. As a simple starting point, we model the simultaneous deposition of nanocrystal and polymer at the edge of the drying drop using a lattice-Boltzmann (LB) approach. This provides us with a novel description of the effect while giving us a sense of the importance of Marangoni flows, which have a critical influence on the observed patterns. Details of the simulation are given in reference [124]. A two-component system of solvent and vapor was set up as a droplet on a locally wetting substrate, where the wetting surface was used to maintain a constant 2D shape for the base of the droplet. In the simulated images (Figure 60), the vapor phase is indicated in green and the fluid is white. A nearly uniform chemical potential gradient was then imposed through a nonequilibrium boundary condition on the top of the drop, which breaks the conservation law associated with solvent volume, allowing for evaporation.

Temperature variation within the drop and a temperature dependent surface tension were used to reproduce Marangoni effects. The nanoparticles (both PS and SiNC) were treated as massless tracer particles that can only reside inside the drop.

A gradient in chemical potential between the edge of the simulation and the surface of the drop develops and the drop begins to slowly shrink. For very small droplets that have dynamics dominated by diffusion, the effect of hydrodynamics can be neglected. Such droplets quickly evaporate and their shape deviates from a spherical cap. The evaporating interface collects the suspended nanoparticles and enriches their concentration at the free surface, leaving a higher particle concentration in the middle of the drop. The nonspherical shape of the interface implies that the pressure inside the droplet is not constant; the pressure at the edges is lower than at the top.

For macroscopic droplets with hydrodynamics, the pressure imbalance sets up a flow that restores the spherical shape. However, once the spherical shape has been restored, the maximum hydrodynamic effect has been achieved. Reducing the viscosity or increasing the droplet size will not induce a more pronounced hydrodynamic effect. The flow field established in this scenario will then sweep particles from the enriched regions near the free surface toward the edge of the drop where the contact line is pinned. This leads to the transport of the majority of particles to the contact line, consistent with the experiments.

An additional important feature of the drying process relates to the pinning strength of the contact line. As the droplet evaporates, the contact angle at the edge of the drop decreases, and (with the exception of the scenario of total wetting) the contact line will always become unpinned once the equilibrium contact angle of the wetting patch is reached. The resulting evaporation dynamics will then lead to a much reduced hydrodynamic effect and the remaining nanoparticles in the drop (those that

have not already been deposited at the contact line) will then be deposited more evenly. The two critical underlying phenomena in the pattern formation are thus contact-line pinning and solvent evaporation.

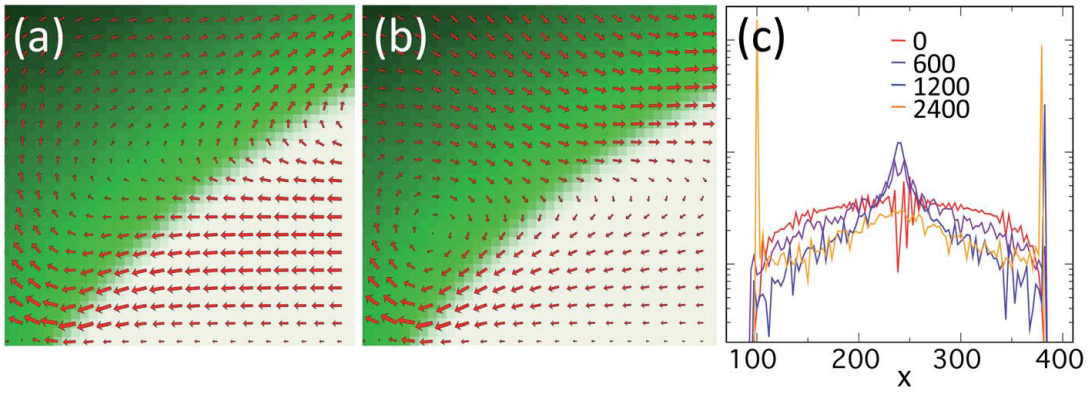

Figure 60: (a)-(b) Lattice-Boltzmann simulation [124] showing the velocity field of the solvent and vapor at two consecutive times during drying, where white denotes solvent, green denotes vapor, and different shades denote different values of the chemical potential. (c) Histograms of the distribution of nanoparticles across the basal diameter (x) of the simulated droplet at different times (in units of 10^2 lattice time steps).

When the effect of latent heat is included, the surface of the drop undergoes evaporative cooling. The simulations keep the substrate at a constant temperature such that heat is diffused from the substrate to the surface of the drop. The portion of the interface closest to the substrate receives this heat most efficiently, creating a temperature gradient along the interface that generates a gradient in surface tension. The surface tension gradient, in turn, induces a rotational flow, as shown in Figure 60. The overall flow field is a combination of the original edge-directed flow and a flow toward the region of lower surface tension. An additional effect is that the mechanical equilibrium of a drop with varying surface tension is no longer spherical, and our simulations suggest that an unsteady flow results. Two typical flow fields are shown in Figures 60(a) and (b). In Figure 60(a), there is a vortex at the right edge of the simulation section. This vortex then migrates left toward the edge and leaves

the drop, as shown in Figure 60(b). These dynamic vortices are reminiscent of the unsteady vortices observed in the experiments, although further study is needed to quantitatively link the two effects. The net local flow over several such oscillations is along the interface toward the center. Since the interface shows the highest concentration of particles, this leads to a migration of particles toward the center of the drop. The overall hydrodynamics, however, maintains a net flow toward the edge. As the drop evaporates, the Marangoni effect is diminished and particles migrate to the edge [Figure 60(c)].

8.1.3. Free-Volume Theory

As noted previously, what makes the fluid mixtures studied here especially interesting is PS/SiNC phase separation above a threshold concentration in the toluene solutions. Phase segregation occurs through both entropic (depletion) and enthalpic (van der Waals) effects. Since the drying instability concentrates the particles at the contact line, it can thus be anticipated that the mixtures will become immiscible there. This is shown in Figure 61 for low-molecular-weight (2.4k) PS. Although from a coarse perspective the ring deposit looks uniform, closer inspection reveals phase separation into nanocrystal-rich and polymer-rich domains. This texture can be seen in atomic-force microscopy (AFM) images [high and low regions, Figure 61(b)], bright-field images [Figure 61(c)], reflection optical images [different colors in Figure 61(d)] and PL-based images [different colors in Figure 61(e)].

The measurements of the binodal curves were therefore used to calibrate a free-volume theory of polymer-colloid mixtures, as detailed in reference [124] and as shown in Figure 62(b). Our model is an extension of the Asakura-Oosawa-Vrig model [125, 126]. Specifically, we adapt the theory of Schmidt et al. [127], extending the original theory of Lekkerkerker et al. [128] to mixtures of interacting colloids and polymers in a good solvent. The theory contains two free parameters – a van der

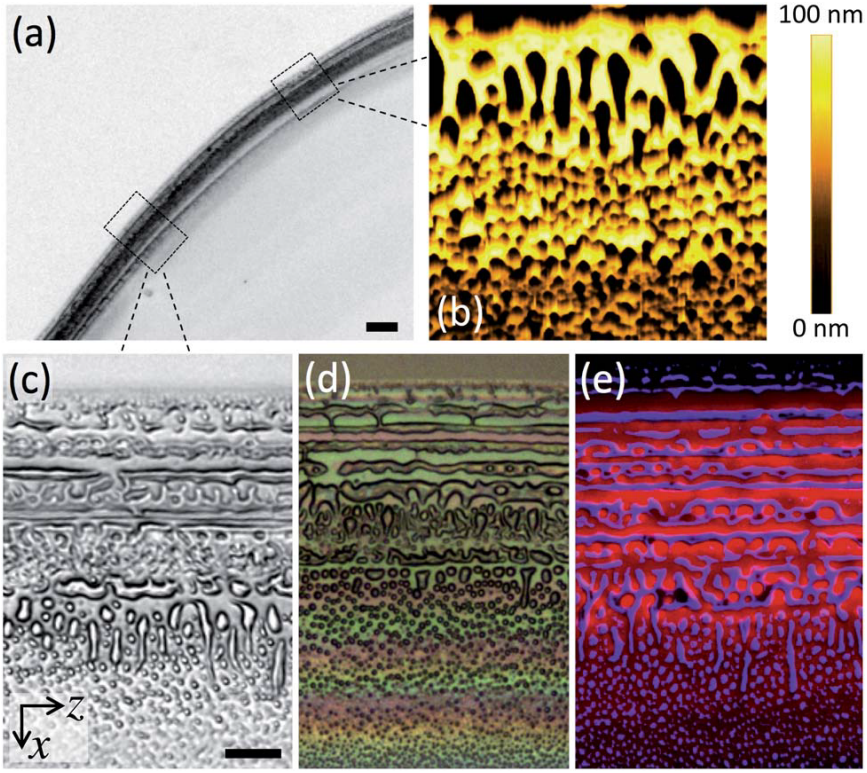

Figure 61: (a) Bright-field image of the edge of a dried droplet (50 μm scale, 0.01 % M_w = 2.4k PS and 0.1 % SiNC). (b) AFM image of the outer edge of the same dried droplet (width = 40 μm). (c) Bright-field image, (d) reflection optical image, and (e) PL-based composite optical image (red = SiNC, blue = PS) of the dried droplet edge, where the scale of 10 μm applies to each of the three panels. In (b)-(e), the contact line is at the top and the x direction is down.

Waals (vdW) parameter for the strength of vdW attraction between nanoparticles and a nanoparticle-polymer penetration parameter for the free energy cost incurred when a nanoparticle penetrates a polymer coil. We know that the latter effect is important because toluene solutions of the ligand (1-dodecene) and polymer (PS) phase separate upon drying. Figure 62(b) shows the predicted binodals for the three mixtures based on these two fitting parameters, where the critical point for 200k PS is indicated as a star. All of the drying experiments considered here occur along lines of constant SiNC:PS mass ratio between the two red lines in Figure 62(b).

8.2. Discussion

Although coupling between the coffee-ring instability and liquid-liquid phase separation is clearly a complex problem, a simple and intuitive picture emerges by considering the implications of the simulations and the equilibrium phase behavior independently. Since the drying process concentrates particles at the contact line independent of type (polymer versus nanocrystal), it can be anticipated that the mixtures will phase separate as the solvent is removed, or as the mixtures impinge on the contact line. The morphology of phase separation will then be influenced by the nature of the local flow field. As can be viewed from the online movies [124], the experiments are in quite reasonable agreement with this simple perspective.

Interestingly, the molecular weight of the polymer has a striking influence on the morphology of the drying ring, as shown in Figure 63. We observe three fundamental structures, as denoted in the state diagrams in Figure 63(a)-(c). The morphology sequence at fixed c_{PS} and increasing c_{SiNC} is the same as that for fixed c_{SiNC} and decreasing c_{PS}. The upper-left morphology is 'edge-deposited', or a microstructure of concentric stratified rings [Figure 63(d)]; the middle structure is spoke-like or 'radial' [Figure 63(e)-(g)], and the lower right morphology is inverted or continuous [Figure 63(h)-(i)]. The radial morphology has been observed in drying experiments on droplets of microscopic colloid/polymer mixtures [119], and it has been predicted for drying-induced spinodal decomposition [121]. Here, the radial morphology is further stratified into anisotropic droplets or domains, as shown in Figure 63(e). The dashed lines in the diagrams indicate approximate transitions, where the lower dashed line also corresponds to the anticipated inversion line of 50/50 volume fraction.

As the molecular weight of the polymer decreases, the width of the radial region shrinks until it becomes difficult to discern [dashed blue line, Figure 63(c)]. The other obvious M_w dependence is the domain size, which increases according to $R_z \propto M_w^{0.36}$

for 1:10 PS:SiNC by mass and $R_z \propto M_w^{0.42}$ for 50:50 PS:SiNC by mass, where R_z is the mean width of the domains along the z direction determined from optical micrographs. We suggest that these two effects are related; the shrinking middle pattern with decreasing M_w reflects a decrease in domain size that moves the edge-directed morphology to lower c_{PS} and higher c_{SiNC}. In general, the final size of the domains will be $R \propto \int_0^\infty \gamma[c(t)]/\eta[c(t)]dt$ for some local history $c(t)$, where $c(t)$ is the solvent concentration, γ is the interfacial tension between the two phases and η is the shear viscosity. If we assume that R_z scales as $\gamma/\eta_{\mathrm{PS}}$, the relation $\eta_{\mathrm{PS}} \propto M_w^{0.73}$ for PS in toluene [129] then suggests $\gamma \propto M_w^{1.1}$ or $M_w^{1.15}$, with an exponent close to unity. Physically, the domain size will be determined primarily by the competing effects of interfacial tension, which drives coarsening, and viscosity, which limits the time scale for growth. While both of these depend on M_w, the data suggest that the molecular-weight dependence of γ dominates. This is consistent with the state diagrams in Figure 62(b), which indicate that the quench depth (although somewhat ill-defined for a drying droplet) should increase with increasing M_w.

A critical feature of the experiments that the current version of the simulations accounts for is the presence of strong vorticity or circulation, presumably associated with Marangoni flows. Such flows would be anticipated, given the strong gradient in particle concentration near the contact line. These effects are most easily seen in the online movies [124]. Rotating flow is always observed at the edge of the front, primarily in the x-y plane but also in the x-z plane. This leads to a shear stress in the x-y plane that ruptures and distorts the domains, as shown in the lower panels of Figure 63. The process is depicted as a function of time in Figure 64. The crescent-like shape of the SiNC-rich domains in Figures 63 and 64 is due to vorticity in the x-z plane, which pulls the two ends of a domain back toward the center of the drying droplet. The observed trend of outward flow (toward the contact line) at the wetting

surface of the droplet is reproduced by the simulations, however. This is intuitive, since the solvent leaves through the top surface and the concentration of particles is thus highest there. The net flow of fluid toward the contact line becomes more pronounced in the latter part of the simulations.

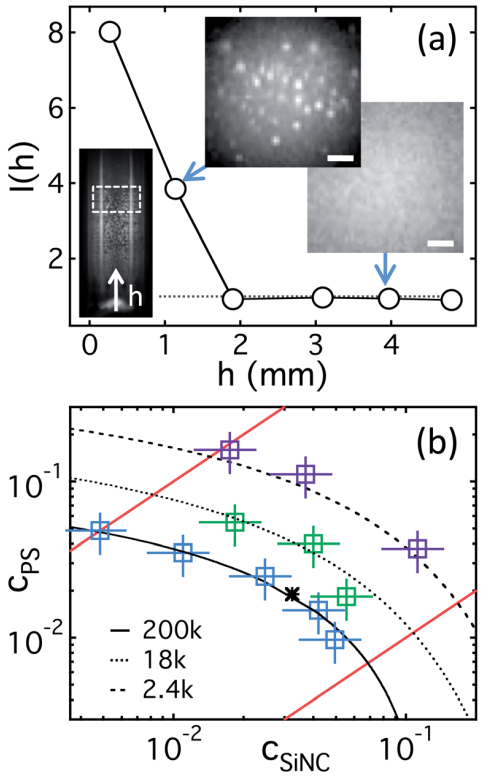

Figure 62: (a) Microcapillary method for measuring the equilibrium binodals, where $I(h)$ is the ratio of the final PL intensity (h is the distance along the tube from the pinned end) to the initial homogeneous PL intensity. The images are micrographs of the structure (scale = 10 μm). (b) Equilibrium binodal curves plotted as polymer mass fraction (c_{PS}) versus nanocrystal mass fraction (c_{SiNC}), where the markers represent measurements and the curves are computed. The two red lines are the drying lines that bound all of the nonequilbrium data presented in the paper. Blue markers are 200k PS, green markers are 18k PS and violet markers are 2.4k PS.

The instabilities we describe here will hinder the formation of homogeneous polymer/nanocrystal mixtures, which in turn will impact the ability to print nanocomposite features from complex fluids. Because of this rather important implication, we further explored a possible 'printing' scheme to stabilize the drying process. Our

approach is motivated by somewhat similar work on solutions of polymers and CdSe nanocrystals recently carried out by Kim *et al.* [130]. Figure 65(a) shows PL spectra of the ring deposits, with PL lifetime (τ) shown in the inset. Since PL quantum yield is proportional to lifetime [34, 101], the inset to Figure 65(a) suggests relatively little variation in quantum yield among the dried mixtures, although there is a weak redshift with decreasing M_w [Figure 65(b)]. During drying, the PL intensity increases most strongly with time for the pure SiNC suspensions, as would be anticipated [Figure 65(b)]. To control the shape and location of the contact line, an automated blade-printing technique was used to deposit a series of parallel lines or 'wires', as depicted in Figure 65(c). A pool of SiNC/PS/toluene solution is maintained behind the edge of a stationary angled blade while the substrate is periodically moved and then held in position for 120 s. At each blade location with respect to the moving substrate, solution seeps out from under the blade, where drying and edge-directed flow lead to the deposition of particulates at the substrate contact line [Figure 65(c)]. Since the small volume of mixture on the obtuse side of the blade is connected to the larger pool on the acute side, there is only one contact line on the printing side, which allows for the deposition of a single line. When the substrate is then translated to print the next line, the reservoir of liquid behind the blade is swept over the previous back contact line, redissolving any solids deposited on the acute side [left of the blade, Figure 65(c)].

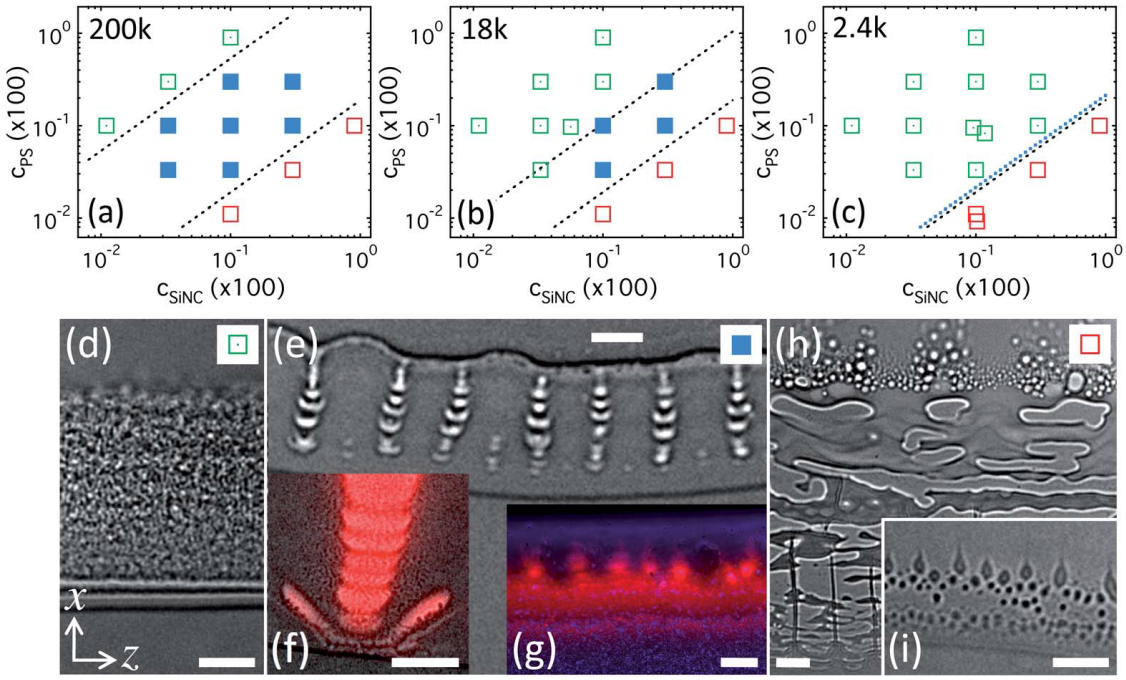

Figure 63: Morphology diagrams (initial c_{PS} versus initial c_{SiNC}) for PS molecular weights of (a) 200k (b) 18k and (c) 2.4k, where the dashed lines indicate the approximate locations of transitions. (d) A bright-field image of the edge-deposited morphology (green squares, 2.5 μm scale, 0.3 % M_w = 2.4k PS, 0.1 % SiNC). (e) A wide bright-field view of the 'radial' morphology (blue squares, 10 μm scale, 0.1 % M_w = 200k PS, 0.1 % SiNC), (f) a PL image of the same pattern (5 μm scale, 0.1 % M_w = 200k PS, 0.1 % SiNC), and (g) the pattern at higher polymer concentration (10 μm scale, 0.3 % M_w = 200k PS, 0.1 % SiNC). (h) Inverted morphology (red squares) for the high-molecular-weight polymer (10 μm scale, 0.03 % M_w = 200k PS, 0.3 % SiNC) and (i) the same inverted structure for the low-molecular-weight polymer (5 μm scale, 0.033 % M_w = 2.4k PS, 0.1 % SiNC). All images are in the x-z plane, where the positive flow (x) direction is perpendicular to the contact line and directed up.

The printing method is capable of systematically depositing homogeneous pure SiNC and PS-SiNC nanocomposite wires for the 2.4k PS, but mixtures of higher M_w are still hindered by phase separation, as shown in Figure 65(d)-(h). For 18k and 200k PS mixtures, the morphology of the phase-separation pattern in the printed nanocomposite lines is consistent with the state diagrams in Figure 63(a)-(c), but the 'crescent' droplet shape is suppressed. The M_w dependence of the structure is also evident in resistivity measurements of the printed wires, as shown in Figure 65(i).

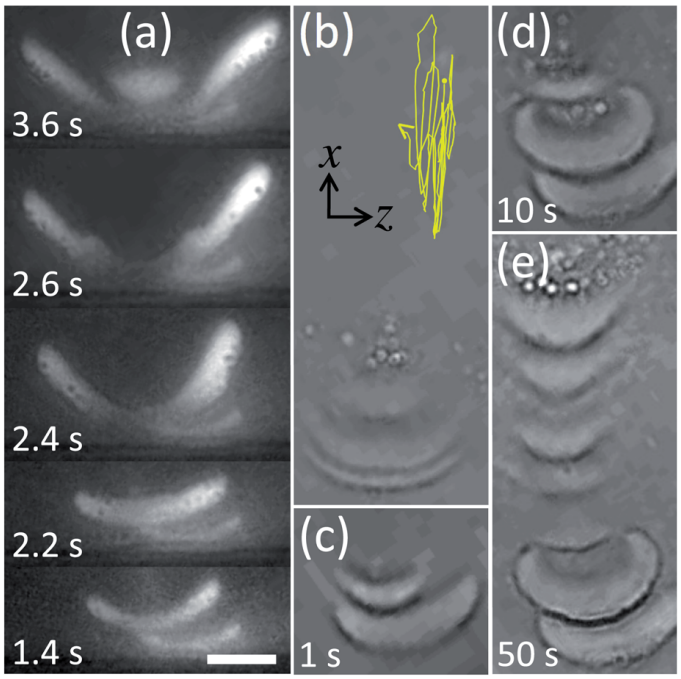

Figure 64: (a) Image sequence of coarsening for the 'radial' morphology (3.5 μm scale, 0.1 % M_w = 200k PS, 0.1 % SiNC), where time increases from bottom to top. (b) Rotating particle trajectory (yellow trace) in the region away from the front (width = 6 μm, 0.1 % M_w = 200k PS, 0.1 % SiNC), where the time step is 0.033 s. Bright-field images of the coarsening front at (c) t = 1 s, (d) t = 10 s and (e) t = 50 s (width = 6 μm, 0.1 % M_w = 200k PS, 0.1 % SiNC). The positive x direction is from bottom to top in all images.

While the transport characteristics of the 2.4k PS structures are nearly identical to those of the pure SiNCs, the two higher molecular weights (18k and 200k) show transport characteristics that begin to approach the response of the bare glass substrates [Figure 65(i)]. We suggest that the formation of isolated SiNC-rich domains, such as those shown in Figures 65(e) and (h), hinders the tendency for the nanocomposites to form percolation pathways suitable for charge 'hopping' and transport. These observations should provide useful insight for developing schemes that can print controlled and well-defined morphologies from volatile nanoparticle mixtures, ranging from homogeneously dispersed composites to periodically segregated structures.

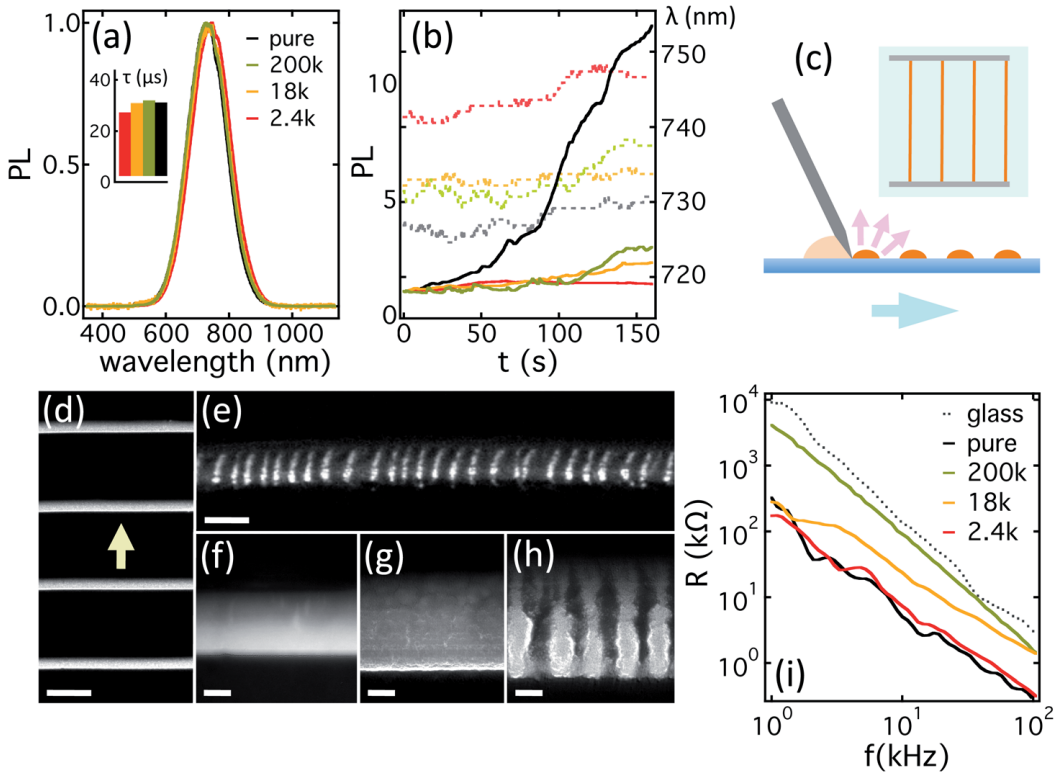

Figure 65: (a) PL spectra and lifetimes (inset) for nanocomposites and pure SiNCs. (b) Time-dependent PL (solid) and emission wavelength (dashed, right scale) at the droplet edge during drying. (c) Schematic of the blade-printing setup. (d) Printed nanocomposite 'lines' (250 μm scale, 0.3 % 2.4k PS, 0.3 % SiNC). (e) Nanocomposite line printed from 18k PS (120 μm scale, 0.3 % PS, 0.3 % SiNC). (f) Line morphology for pure SiNCs (20 μm scale), (g) a 2.4k PS nanocomposite (20 μm scale, 0.3 % PS, 0.3 % SiNC) and (h) an 18k PS nanocomposite (20 μm scale, 0.3 % PS, 0.3 % SiNC). (i) Line resistivities for nanocomposites and pure SiNCs. In (d)-(h), the slide moves in the direction indicated by the arrow in (c) and (d) while the blade is stationary.

8.3. Conclusion

The coupling between the coffee-ring effect and liquid-liquid phase separation has been examined for ternary mixtures of toluene, polymer and colloidal semiconductor nanocrystal. Simultaneous drying and phase separation have been studied for varied polymer molecular weight using PL-based optical techniques to resolve the domain morphology at the contact line. Our results demonstrate that the molecular weight of the PS has a significant impact on the phase behavior of the mixtures and

hence the character of the drying instability. We explain these observations with (i) a novel lattice-Boltzmann scheme that accounts for particle deposition at a pinned contact line and (ii) a free-volume theory of the equilibrium phase behavior that then accounts for phase separation at the front as the solvent is removed. Empirical observations of the shape of the flow field at the contact line offer a physical picture of the coupled instabilities.

These findings help us formulate a liquid printing process that reduces the influence of drying/mixing instabilities for low-molecular-weight polymers while isolating the effects of phase separation for medium and high-molecular-weight polymers. The morphology of printed nanocomposite wires is found to be dictated by details of the coupling between drying and phase separation, as further confirmed by conductivity measurements performed on printed arrays of parallel lines. This insight should have significant implications for applications that seek to print homogeneous patterns from multicomponent solutions of nanoscale objects, but it should also help guide efforts that seek to exploit phase separation as a way to engineer patterned microstructures from binary solutions of polymers and nanoparticles. In addition, our LB results lay a foundation for more detailed and predictive computational models and simulations of drying instabilities in multiphase complex fluids.

For PS:SiNC concentration ratios just above the inversion line in Figure 63, the phase separation morphology coarsely resembles the pattern predicted by simulations of phase separation in drying ternary mixtures [121]. Here, this morphology consists of flow-aligned SiNC-rich domains periodically spaced along the contact line. The spoke-like pattern is observed for the 18k and 200k PS but is suppressed for the 2.4k PS, which we suggest is due to the greater quench depth for phase separation at higher PS molecular weight and subsequent coarsening driven by stronger interfacial tension. At smaller length scales, details of the microstructure, such as stratification

of domains into crescent-shaped subdroplets, are dictated by the nature of circulatory Marangoni flows.

The blade printing method likely has an impact on the morphology because it suppresses Marangoni flow along the relevant direction (perpendicular to the blade). This can be seen by comparing the morphology in Figure 65(h) with that in Figure 63(e); the crescent domain shape and the stratification of domain structure along the flow (x) direction are suppressed in Figure 65, where the morphology more closely resembles that of the simulations in reference [121]. An additional factor is likely the rapid drying time of the blade printing approach, which relies on a limited subvolume of the initial mixtures with a large surface area. In the online movies [124] that support Figure 63, the structure at the contact line of a free droplet is seen to redissolve and reform as the concentration of the ternary solution fluctuates due to circulating flows. If the solvent is removed quickly, the PS/SiNC composite will vitrify without sufficient time to coarsen, particularly if the thermodynamic driving force for phase separation is weak, as the equilibrium theory suggests is the case for the 2.4k PS.

CHAPTER 9. OUTLOOK

9.1. Biological Implementation

As mentioned earlier, one of the largest benefits of using SiNCs compared to their heavy metal counterparts is their relative nontoxicity. Fujioka et al. [13] found SiNCs to be more than 10 times less toxic than CdSe nanocrystals under UV exposure. Biological applications are very promising, and there have been numerous recent studies showing the importance and potential use of SiNCs as nontoxic biological markers and therapeutic delivery vehicles [131–135].

9.1.1. Experimental Procedure and Preliminary Results

Preliminary experiments have recently been performed to gain insight into using monodisperse, stable SiNCs for biological applications. The first step involves further surface passivation to allow for the introduction of SiNCs into aqueous environments. This was done through PEGylation of SiNC clusters. Polyethyleneglycol (PEG) grafted phospholipids [1,2-dimyristoyl-sn-glycero-3-phosphoethanolamine-N-[methoxy(polyethylene glycol)-2000] (ammonium salt)], purchased through Avanti Lipids, were solvated in chloroform. A solution of 0.1 % SiNCs in chloroform was added to the solution of PEG to get 1 mL of mixture. This mixture was hand stirred for five minutes and then pipetted into a 50 mL round-bottom glass flask. The flask was attached to a rotary evaporator and submerged in a 37 °C water bath while rotating at 40 rpm. After 2 hours, a uniform thin film of PEG and SiNCs was deposited on the bottom of the flask. A vacuum (17 kPa) was pulled for 5 minutes to remove any excess solvent and then the flask was removed and hydrated with 4 mL of distilled water and allowed to incubate overnight. During this time, the encapsulation of the SiNCs took place. A TEM picture of one ∼220 nm micelle is shown in Figure 66(a).

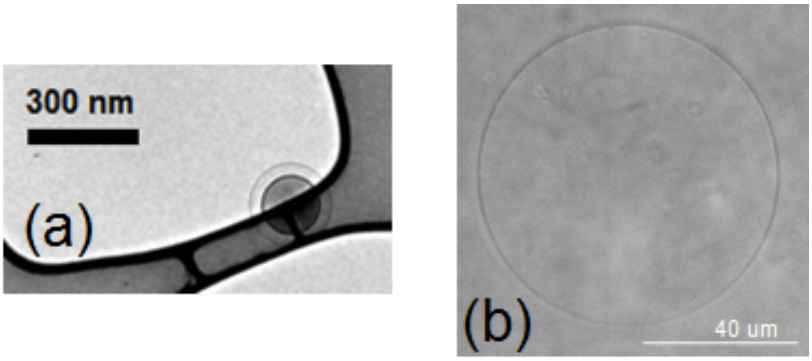

Figure 66: (a) TEM image of a SiNC micelle with outer PEGylated phospholipid layer (lipid boundary highlighted for visualization). (b) Lipid bilayer membrane created *in vitro* to simulate the membrane of a biological cell.

The next step was creating bilayer giant liposomes which model real biological cellular membranes. Liposomes were formed with a 9:1 (L-α-phosphatidylcholine:L-α-phosphatidylglycerol or PC:PG) lipid mixture in chloroform. Methanol was added to achieve a 2:1 (chloroform:methanol) solvent ratio for a total amount of 100 μL in a glass vial. This mixture was hand stirred for five minutes and then transferred to a round-bottom glass tube. It was then dried under a pure nitrogen flow while rotating at a 45 degree angle by hand. One to two milliliters of distilled water was then slowly pipetted into the tube. It was incubated overnight at 37 °C. The liposomes formed in sizes ranging from 5-200 μm. A large ($\sim$75 μm) liposome can be seen in the bright field image shown in Figure 66(b).

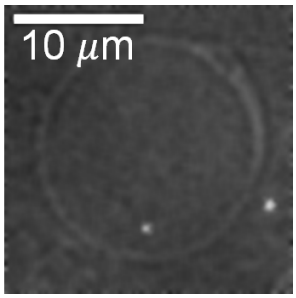

Figure 67: Liposome with an $\sim$300 nm SiNC micelle inside and $\sim$800 nm micelle outside.

After creating SiNC micelles and cellular vesicles, the two were combined and again incubated overnight at 37 °C. A typical system can be seen in Figure 67. We can see two micelles approximately 300 nm (inside) and 800 nm (outside). The smaller micelle underwent cellular uptake in the 24 hours of incubation. These results demonstrate the possibility of using the SiNCs under biological conditions and open windows for further investigations into cellular-nanocrystal interactions and applications.

9.2. Superlattice

Another unique opportunity involves using SiNCs in solid-state electronics and solar panels. For such devices, it may be advantageous to form periodic structures of long-range order or a 'superlattice'. A superlattice may be able to enhance electron mobility and can also act as a band gap manipulator in device manufacturing. For instance, Luque et al. [136] propose that the theoretical efficiency of solar cells can be improved to near 60 % due to the intermediate band gap created by interactions in SiNC superlattices. Recently, there have been numerous studies investigating the self-assembly of nanocrystals. Two such examples can be seen in Figures 68 and 69. Figure 68 is a binary superlattice created from gold (Au) and lead selenide (PbSe) nanoparticles. A mixture of nanoparticles and solvent was dried in a vial containing a TEM grid at a 30 ° angle. The superlattice spontaneously self-assembled into the pattern in Figure 68.

Figure 69 shows another binary superlattice formed from a mixture of CdTe and CdSe nanoparticles. These superlattices can self-assemble in a variety of configurations depending on diameter ratio and passivation scheme.

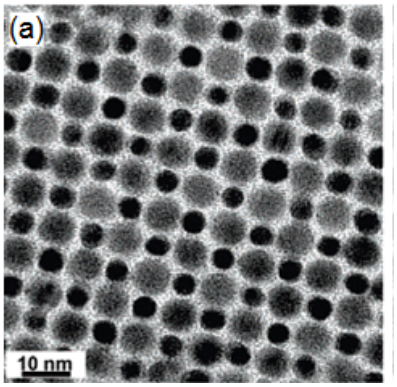

Figure 68: A binary superlattice structure formed by 7.6 nm PbSe and 5.0 nm Au nanoparticles: (a) high magnification TEM image of the (001) projection. "Adapted with permission from [137]. Copyright (2006) American Chemical Society."

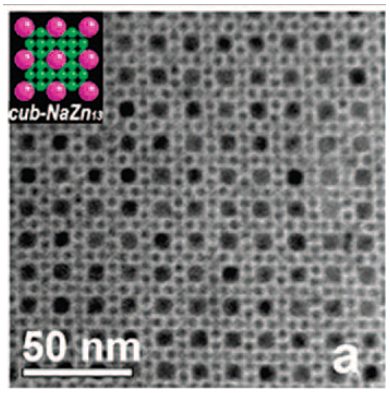

Figure 69: A binary superlattice structure that self-assembled from 9.1 nm CdTe and 4.4 nm CdSe nanoparticles: (a) TEM micrograph along the $(001)_{sl}$ zone axis with corresponding modeled structure (inset). "Reprinted with permission from [138]. Copyright (2008) American Chemical Society."

Although we have not yet achieved the long-range order defined by a superlattice, we can see from Figure 70 that this goal may not be far off. The problem associated with superlattice formation from SiNCs is their relatively strong van der Waals forces (the Hamaker constant of silicon is found to be three to four times larger than that of CdSe [139–141]) which tend to promote small, tightly-bound ordered or disordered domains rather than long-range crystalline order. We are currently trying to overcome this by synthesizing our own SiNCs (Synthesis section). Adding surface

charge or longer, stiffer ligands could help mitigate these strong van de Waals forces and allow for superlattice self-assembly.

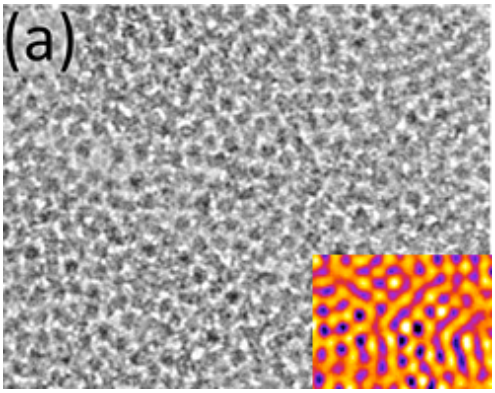

Figure 70: (a) TEM images of Si NC thin film with inset (false color) highlighting the domains of short-range order.

REFERENCES

[1] M. A. Reed, J. N. Randall, R. J. Aggarwal, R. J. Matyi, T. M. Moore, and A. E. Wetsel. Observation of discrete electronic states in a zero-dimensional semiconductor nanostructure. *Physical Review Letters*, 60(6):535–537, 1988.

[2] A. I. Ekimov and A. A. Onushchenko. Quantum size effect in 3-dimensional microscopic semiconductor crystals. *JETP Letters*, 34(6):345–349, 1981.

[3] M. G. Bawendi, M. L. Steigerwald, and L. E. Brus. The quantum-mechanics of larger semiconductor clusters (quantum dots). *Annual Review of Physical Chemistry*, 41:477–496, 1990.

[4] G. H. Wei, B. Bhushan, and P. M. Torgerson. Nanomechanical characterization of human hair using nanoindentation and SEM. *Ultramicroscopy*, 105(1-4):248–266, 2005.

[5] Nishit Doshi, Alisar S. Zahr, Srijanani Bhaskar, Joerg Lahann, and Samir Mitragotri. Red blood cell-mimicking synthetic biomaterial particles. *Proceedings of the National Academy of Sciences of the United States of America*, 106(51):21495–21499, 2009.

[6] Brocken Inaglory. "Water droplet at DWR-coated surface" licenced under CC BY - SA 3.0. Accessed: March 10, 2014.

[7] C. L. Choi and A. P. Alivisatos. From artificial atoms to nanocrystal molecules: preparation and properties of more complex nanostructures. *Annual Review of Physical Chemistry*, 61:369–389, 2010.

[8] A. Y. Koposov, P. Szymanski, T. Cardolaccia, T. J. Meyer, V. I. Klimov, and M. Sykora. Electronic properties and structure of assemblies of CdSe

nanocrystal quantum dots and ru-polypyridine complexes probed by steady state and time-resolved photoluminescence. *Advanced Functional Materials*, 21(16):3159–3168, 2011.

[9] I. Kriegel, C. Y. Jiang, J. Rodriguez-Fernandez, R. D. Schaller, D. V. Talapin, E. da Como, and J. Feldmann. Tuning the excitonic and plasmonic properties of copper chalcogenide nanocrystals. *Journal of the American Chemical Society*, 134(3):1583–1590, 2012.

[10] M. Law, J. M. Luther, Q. Song, B. K. Hughes, C. L. Perkins, and A.J. Nozik. Structural, optical, and electrical properties of PbSe nanocrystals solids treated thermally or with simple amines. *Journal of American Chemical Society*, 130(18):5974–5985, 2008.

[11] L. Mangolini. Synthesis, properties, and applications of silicon nanocrystals. *Journal of Vacuum Science & Technology B*, 31(2):020801, 2013.

[12] L. Pavesi and R. Turan. *Silicon Nanocrystals: Fundamentals, Synthesis, and Applications*. Wiley-VCH Verlag GmbH & Co. KGaA, Weinheim, Germany, 2010.

[13] K. Fujioka, M. Hiruoka, K. Sato, N. Manabe, R. Miyasaka, S. Hanada, A. Hoshino, R. D. Tilley, Y. Manome, K. Hirakuri, and K. Yamamoto. Luminescent passive-oxidized silicon quantum dots as biological staining labels and their cytotoxicity effects at high concentration. *Nanotechnology*, 19(41):415102, 2008.

[14] Z. F. Ding, B. M. Quinn, S. K. Haram, L. E. Pell, B. A. Korgel, and A. J. Bard. Electrochemistry and electrogenerated chemiluminescence from silicon nanocrystal quantum dots. *Science*, 296(5571):1293–1297, 2002.

[15] C. H. Lee, A. Sazonov, and A. Nathan. High-mobility nanocrystalline silicon thin-film transistors fabricated by plasma-enhanced chemical vapor deposition. *Applied Physics Letters*, 86(22):222106, 2005.

[16] L. Mangolini and U. Kortshagen. Plasma-assisted synthesis of silicon nanocrystal inks. *Advanced Materials*, 19(18):25132519.

[17] J. H. Warner, A. Hoshino, K. Yamamoto, and R. D. Tilley. Water-soluble photoluminescent silicon quantum dots. *Angewandte Chemie-International Edition*, 44(29):4550–4554, 2005.

[18] J. B. Miller and E. K. Hobbie. Nanoparticles as macromolecules. *Journal of Polymer Science Part B-Polymer Physics*, 51(16):1195–1208, 2013.

[19] C. L. Amiot, S. P. Xu, S. Liang, L. Y. Pan, and J. X. J. Zhao. Near-infrared fluorescent materials for sensing of biological targets. *Sensors*, 8(5):3082–3105, 2008.

[20] Z. Cheng, Y. Wu, Z. M. Xiong, S. S. Gambhir, and X. Y. Chen. Near-infrared fluorescent RGD peptides for optical imaging of integrin alpha(v)beta 3 expression in living mice. *Bioconjugate Chemistry*, 16(6):1433–1441, 2005.

[21] H. Kobayashi, Y. Hama, Y. Koyama, T. Barrett, C. A. S. Regino, Y. Urano, and P. L. Choyke. Simultaneous multicolor imaging of five different lymphatic basins using quantum dots. *Nano Letters*, 7(6):1711–1716, 2007.

[22] L. Gu, D. J. Hall, Z. T. Qin, E. Anglin, J. Joo, D. J. Mooney, S. B. Howell, and M. J. Sailor. In vivo time-gated fluorescence imaging with biodegradable luminescent porous silicon nanoparticles. *Nature Communications*, 4:2326, 2013.

[23] S. F. Lee and M. A. Osborne. Brightening, blinking, bluing and bleaching in the life of a quantum dot: friend or foe? *Chemphyschem*, 10(13):2174–2191, 2009.

[24] L. T. Canham. Silicon quantum wire array fabrication by electrochemical and chemical dissolution of wafers. *Applied Physics Letters*, 57(10):1046–1048, 1990.

[25] Bernard Gelloz. *Silicon Nanocrystals in Porous Silicon and Applications*, pages 349–381. WILEY-VCH, 2010.

[26] Fabio Iacona, Giorgia Franzo, Alessia Irrera, Simona Boninelli, and Francesco Priolo. *Structural and Optical Properties of Silicon Nanocrystals*, pages 247–272. WILEY-VCH, 2010.

[27] Robert Elliman. *The Synthesis of Silicon Nanocrystals by Ion Implantation*, pages 223–244. WILEY-VCH, 2010.

[28] Aylin Karakuscu and Gian Domenico Soraru. *Si and SiC Nanocrystals by Pyrolysis of Sol-Gel-Derived Precursors*, pages 297–305. WILEY-VCH, 2010.

[29] Margit Zacharias. *Size-Controlled Si Nanocrystals using the SiO/SiO2 Superlattice Approach: Crystallization, Defects, and Optical Properties*, pages 195–219. WILEY-VCH, 2010.

[30] M. Ehbrecht, B. Kohn, F. Huisken, M. A. Laguna, and V. Paillard. Photoluminescence and resonant Raman spectra of silicon films produced by size-selected cluster beam deposition. *Physical Review B*, 56(11):6958–6964, 1997.

[31] Colin M. Hessel, Dariya Reid, Matthew G. Panthani, Michael R. Rasch, Brian W. Goodfellow, Junwei Wei, Hiromasa Fujii, Vahid Akhavan, and

Brian A. Korgel. Synthesis of ligand-stabilized silicon nanocrystals with size-dependent photoluminescence spanning visible to near-infrared wavelengths. *Chemistry of Materials*, 24(2):393–401, 2012.

[32] L. Mangolini, D. Jurbergs, E. Rogojina, and U. Kortshagen. Plasma synthesis and liquid-phase surface passivation of brightly luminescent Si nanocrystals. *Journal of Luminescence*, 121(2):327–334, 2006.

[33] X. D. Pi, R. W. Liptak, J. Deneen Nowak, N. Pwells, C. B. Carter, S. A. Campbell, and U. Kortshagen. Air-stable full-visible-spectrum emission from silicon nanocrystals synthesized by an all-gas-phase plasma approach. *Nanotechnology*, 19(24):245603, 2008.

[34] Joseph B. Miller, Austin R. Van Sickle, Rebecca J. Anthony, Daniel M. Kroll, Uwe R. Kortshagen, and Erik K. Hobbie. Ensemble brightening and enhanced quantum yield in size-purified silicon nanocrystals. *ACS Nano*, 6(8):7389–7396, 2012.

[35] A. P. Alivisatos. Semiconductor clusters, nanocrystals, and quantum dots. *Science*, 271(5251):933–937, 1996.

[36] Filikhin I., Matinyan S. G., and Vlahovic B. Quantum mechanics of semiconductor quantum dots and rings, 2012.

[37] Siegfried Flügge. *Practical Quantum Mechanics*, volume 1. Springer, Berlin, 1971.

[38] J. Jortner and M. Ratner. Molecular electronics - a 'chemistry for the 21st century' monograph - introduction. *Molecular Electronics*, pages 1–4, 1997.

[39] Neil W. Ashcroft and N. David Mermin. *Solid State Physics*. Brooks/Cole, 1976.

[40] W. E. Pickett. "Tight binding" method: linear combination of atomic orbitals (LCAO), 2006.

[41] C. Delerue, G. Allan, and M. Lannoo. Theoretical aspects of the luminescence of porous silicon. *Physical Review B*, 48(15):11024–11036, 1993.

[42] Daniel Bellet, Grard Dolino, Mireille Ligeon, Pierre Blanc, and Michel Krisch. Studies of coherent and diffuse X-ray scattering by porous silicon. *Journal of Applied Physics*, 71(145):145–149, 1992.

[43] IBM Corporation. Silicon bandstructure and density of states. `http://www.research.ibm.com/DAMOCLES/html_files/phys.html`. Accessed: March 15, 2014.

[44] MIT lectures: physics for solid state applicatons. `http://web.mit.edu/6.730/www/ST04/Lectures/Lecture16.pdf`. Accessed: March 16, 2014.

[45] C. B. Murray, C. R. Kagan, and M. G. Bawendi. Self-organization of cdse nanocrystallites into 3-dimensional quantum-dot superlattices. *Science*, 270(5240):1335–1338, 1995.

[46] S. Auer and D. Frenkel. Suppression of crystal nucleation in polydisperse colloids due to increase of the surface free energy. *Nature*, 413(6857):711–713, 2001.

[47] E. Generalic. Centrifugation. `http://glossary.periodni.com/glossary.php?en=centrifugation`. Accessed: March 3, 2014.

[48] G. K. Batchelor. *An Introduction to Fluid Dynamics*. Cambridge University Press, 1st edition, 1967.

[49] Huda A. Jerri, William P. Sheehan, Charles E. Snyder, and Darrell Velegol. Prolonging density gradient stability. *Langmuir*, 26(7):4725–4731, 2010.

[50] C. A. Price. *Centrifugation in Density Gradients*. Academic Press, 1982.

[51] Henry Mühlpfordt and Krzysztof Blachnicki. Structure of a fluorescent microscope. `http://en.wikipedia.org/wiki/File:FluorescenceFilters_2008-09-28.svg`, 2008. Accessed: March 4, 2014.

[52] M. L. Brongersma, A. Polman, K. S. Min, E. Boer, T. Tambo, and H. A. Atwater. Tuning the emission wavelength of Si nanocrystals in SiO2 by oxidation. *Applied Physics Letters*, 72(20):2577–2579, 1998.

[53] D. Kovalev, E. Gross, N. Kunzner, F. Koch, V. Y. Timoshenko, and M. Fujii. Resonant electronic energy transfer from excitons confined in silicon nanocrystals to oxygen molecules. *Physical Review Letters*, 89(13):137401, 2002.

[54] F. Cichos, C. von Borczyskowski, and M. Orrit. Power-law intermittency of single emitters. *Current Opinion in Colloid & Interface Science*, 12(6):272–284, 2007.

[55] David Jurbergs, Elena Rogojina, Lorenzo Mangolini, and Uwe Kortshagen. Silicon nanocrystals with ensemble quantum yields exceeding 60%. *Applied Physics Letters*, 88(23):272–284, 2006.

[56] Melanie L. Mastronardi, Florian Maier-Flaig, Daniel Faulkner, Eric J. Henderson, Christian Kuebel, Uli Lemmer, and Geoffrey A. Ozin. Size-dependent absolute quantum yields for size-separated colloidally-stable silicon nanocrystals. *Nano Letters*, 12(1):337–342, 2012.

[57] B. E. A. Saleh and M. C. Teich. *Fundamentals of Photonics*. Wiley, 2nd edition, 2007.

[58] K. G. Lyon, G. L. Salinger, C. A. Swenson, and G. K. White. Linear thermal-expansion measurements on silicon from 6 to 340 K. *Journal of Applied Physics*, 48(3):865–868, 1977.

[59] J. Linnros, N. Lalic, A. Galeckas, and V. Grivickas. Analysis of the stretched exponential photoluminescence decay from nanometer-sized silicon crystals in SiO2. *Journal of Applied Physics*, 86(11):6128–6134, 1999.

[60] C. Delerue, G. Allan, C. Reynaud, O. Guillois, G. Ledoux, and F. Huisken. Multiexponential photoluminescence decay in indirect-gap semiconductor nanocrystals. *Physical Review B*, 73(23):235318, 2006.

[61] J. C. Phillips. Stretched exponential relaxation in molecular and electronic glasses. *Reports on Progress in Physics*, 59(9):1133–1207, 1996.

[62] K. C. B. Lee, J. Siegel, S. E. D. Webb, S. Leveque-Fort, M. J. Cole, R. Jones, K. Dowling, M. J. Lever, and P. M. W. French. Application of the stretched exponential function to fluorescence lifetime imaging. *Biophysical Journal*, 81(3):1265–1274, 2001.

[63] G. Zatryb, A. Podhorodecki, J. Misiewicz, J. Cardin, and F. Gourbilleau. On the nature of the stretched exponential photoluminescence decay for silicon nanocrystals. *Nanoscale Research Letters*, 6:106, 2011.

[64] M. Dovrat, Y. Goshen, J. Jedrzejewski, I. Balberg, and A. Sa'ar. Radiative versus nonradiative decay processes in silicon nanocrystals probed by time-resolved photoluminescence spectroscopy. *Physical Review B*, 69(15):155311, 2004.

[65] Milan Sykora, Lorenzo Mangolini, Richard D. Schaller, Uwe Kortshagen, David Jurbergs, and Victor I. Klimov. Size-dependent intrinsic radiative decay rates

of silicon nanocrystals at large confinement energies. *Physical Review Letters*, 100(6):067401, 2008.

[66] D. S. English, L. E. Pell, Z. H. Yu, P. F. Barbara, and B. A. Korgel. Size tunable visible luminescence from individual organic monolayer stabilized silicon nanocrystal quantum dots. *Nano Letters*, 2(7):681–685, 2002.

[67] A. A. Prokofiev, A. S. Moskalenko, I. N. Yassievich, W. D. A. M. de Boer, D. Timmerman, H. Zhang, W. J. Buma, and T. Gregorkiewicz. Direct bandgap optical transitions in Si nanocrystals. *Jetp Letters*, 90(12):758–762, 2009.

[68] Dolf Timmerman and Tom Gregorkiewicz. Power-dependent spectral shift of photoluminescence from ensembles of silicon nanocrystals. *Nanoscale Research Letters*, 7:389, 2012.

[69] J. D. Lee and S. Maenosono. Intensified blinking, continuous memory loss, and fluorescence enhancement of interacting light-emission quantum dots. *Physical Review B*, 80(20):205327, 2009.

[70] Siying Wang, Claudia Querner, Tali Dadosh, Catherine H. Crouch, Dmitry S. Novikov, and Marija Drndic. Collective fluorescence enhancement in nanoparticle clusters. *Nature Communications*, 2:364, 2011.

[71] Takafumi Uematsu, Shinya Maenosono, and Yukio Yamaguchi. Photoinduced fluorescence enhancement in CdSe/ZnS quantum dot monolayers: influence of substrate. *Applied Physics Letters*, 89(3):031910, 2006.

[72] Ming Yu and Alan Van Orden. Enhanced fluorescence intermittency of CdSe-ZnS quantum-dot clusters. *Physical Review Letters*, 97(23):237402, 2006.

[73] Mark A. Osborne and Steven F. Lees. Quantum dot photoluminescence activation and decay: dark, bright, and reversible populations in ZnS-capped CdSe nanocrystals. *ACS Nano*, 5(10):8295–8304, 2011.

[74] C. M. Herzinger, B. Johs, W. A. McGahan, J. A. Woollam, and W. Paulson. Ellipsometric determination of optical constants for silicon and thermally grown silicon dioxide via a multi-sample, multi-wavelength, multi-angle investigation. *Journal of Applied Physics*, 83(6):3323–3336, 1998.

[75] F. Cichos, J. Martin, and C. von Borczyskowski. Emission intermittency in silicon nanocrystals. *Physical Review B*, 70(11):115314, 2004.

[76] Svetlana Kilina. Assistant professor of chemistry. North Dakota State University.

[77] Daniel B. Tice, Matthew T. Frederick, Robert P. H. Chang, and Emily A. Weiss. Electron migration limits the rate of photobrightening in thin films of CdSe quantum dots in a dry N2 (g) atmosphere. *Journal of Physical Chemistry C*, 115(9):3654–3662, 2011.

[78] S. Maenosono. Monte-Carlo simulations of photoinduced fluorescence enhancement in semiconductor quantum dot arrays. *Chemical Physics Letters*, 405(1-3):182–186, 2005.

[79] C. G. Christova, J. W. Stouwdam, T. J. Eijkemans, A. Yu Silov, R. W. van der Heijden, M. Kemerink, R. A. J. Janssen, and H. W. M. Salemink. Photoluminescence enhancement in thin films of PbSe nanocrystals. *Applied Physics Letters*, 93(12):121906, 2008.

[80] R. Tuinier, P. A. Smith, W. C. K. Poon, S. U. Egelhaaf, D. G. A. L. Aarts, H. N. W. Lekkerkerker, and G. J. Fleer. Phase diagram for a mixture of colloids and polymers with equal size. *Europhysics Letters*, 82(6):68002, 2008.

[81] Benjamin Bruhn, Jan Valenta, Fatemeh Sangghaleh, and Jan Linnros. Blinking statistics of silicon quantum dots. *Nano Letters*, 11(12):5574–5580, 2011.

[82] I. Sychugov, R. Juhasz, J. Linnros, and J. Valenta. Luminescence blinking of a Si quantum dot in a SiO2 shell. *Physical Review B*, 71(11):115331, 2005.

[83] Jan Valenta, Anna Fucikova, Frantisek Vacha, Frantisek Adamec, Jana Humpolickova, Martin Hof, Ivan Pelant, Katerina Kusova, Katerina Dohnalova, and Jan Linnros. Light-emission performance of silicon nanocrystals deduced from single quantum dot spectroscopy. *Advanced Functional Materials*, 18(18):2666–2672, 2008.

[84] Jeffrey J. Peterson and David J. Nesbitt. Modified power law behavior in quantum dot blinking: a novel role for biexcitons and auger ionization. *Nano Letters*, 9(1):338–345, 2009.

[85] M. Kuno, D. P. Fromm, H. F. Hamann, A. Gallagher, and D. J. Nesbitt. "On"/"off" fluorescence intermittency of single semiconductor quantum dots. *Journal of Chemical Physics*, 115(2):1028–1040, 2001.

[86] Florian Maier-Flaig, Eric J. Henderson, Sebastian Valouch, Soenke Klinkhammer, Christian Kuebel, Geoffrey A. Ozin, and Uli Lemmer. Photophysics of organically-capped silicon nanocrystals - a closer look into silicon nanocrystal luminescence using low temperature transient spectroscopy. *Chemical Physics*, 405:175–180, 2012.

[87] A. M. Hartel, S. Gutsch, D. Hiller, and M. Zacharias. Fundamental temperature-dependent properties of the Si nanocrystal band gap. *Physical Review B*, 85(16):165306, 2012.

[88] X. X. Wang, J. G. Zhang, L. Ding, B. W. Cheng, W. K. Ge, J. Z. Yu, and Q. M. Wang. Origin and evolution of photoluminescence from Si nanocrystals embedded in a SiO2 matrix. *Physical Review B*, 72(19):195313, 2005.

[89] Zhibin Lin, Huashan Li, Alberto Franceschetti, and Mark T. Lusk. Efficient exciton transport between strongly quantum-confined silicon quantum dots. *ACS Nano*, 6(5):4029–4038, 2012.

[90] A. Olkhovets, R. C. Hsu, A. Lipovskii, and F. W. Wise. Size-dependent temperature variation of the energy gap in lead-salt quantum dots. *Physical Review Letters*, 81(16):3539–3542, 1998.

[91] W. Bludau, A. Onton, and W. Heinke. Temperature dependence of the band gap of silicon. *Journal of Applied Physics*, 45(4):1846–1848, 1974.

[92] H. Yildirim Erbil. Evaporation of pure liquid sessile and spherical suspended drops: a review. *Advances in Colloid and Interface Science*, 170(1-2):67–86, 2012.

[93] Emine Tekin, Patrick J. Smith, and Ulrich S. Schubert. Inkjet printing as a deposition and patterning tool for polymers and inorganic particles. *Soft Matter*, 4(4):703–713, 2008.

[94] R. D. Deegan, O. Bakajin, T. F. Dupont, G. Huber, S. R. Nagel, and T. A. Witten. Capillary flow as the cause of ring stains from dried liquid drops. *Nature*, 389(6653):827–829, 1997.

[95] Siddhartha Das, Prashant R. Waghmare, Meng Fan, Naga Siva Kumar Gunda, Susanta Sinha Roy, and Sushanta K. Mitra. Dynamics of liquid droplets in an evaporating drop: liquid droplet "coffee stain" effect. *RSC Advances*, 2(22):8390–8401, 2012.

[96] Byung Mook Weon and Jung Ho Je. Self-pinning by colloids confined at a contact line. *Physical Review Letters*, 110(2):028303, 2013.

[97] Peter J. Yunker, Tim Still, Matthew A. Lohr, and A. G. Yodh. Suppression of the coffee-ring effect by shape-dependent capillary interactions. *Nature*, 476(7360):308–311, 2011.

[98] Peter J. Yunker, Matthew A. Lohr, Tim Still, Alexei Borodin, D. J. Durian, and A. G. Yodh. Effects of particle shape on growth dynamics at edges of evaporating drops of colloidal suspensions. *Physical Review Letters*, 110(3):035501, 2013.

[99] Yueh-Feng Li, Yu-Jane Sheng, and Heng-Kwong Tsao. Evaporation stains: suppressing the coffee-ring effect by contact angle hysteresis. *Langmuir*, 29(25):7802–7811, 2013.

[100] H. B. Eral, D. Mampallil Augustine, M. H. G. Duits, and F. Mugele. Suppressing the coffee stain effect: how to control colloidal self-assembly in evaporating drops using electrowetting. *Soft Matter*, 7(10):4954–4958, 2011.

[101] Austin R. Van Sickle, Joseph B. Miller, Christopher Moore, Rebecca J. Anthony, Uwe R. Kortshagen, and Erik K. Hobbie. Temperature dependent photoluminescence of size-purified silicon nanocrystals. *ACS Applied Materials & Interfaces*, 5(10):4233–4238, 2013.

[102] Beatriz Martin-Garcia, Pedro M. R. Paulo, Silvia M. B. Costa, and M. Mercedes Velazquez. Photoluminescence dynamics of CdSe QD/polymer Langmuir-Blodgett thin films: morphology effects. *Journal of Physical Chemistry C*, 117(28):14787–14795, 2013.

[103] Liying Cui, Junhu Zhang, Xuemin Zhang, Yunfeng Li, Zhanhua Wang, Hainan Gao, Tieqiang Wang, Shoujun Zhu, Hailing Yu, and Bai Yang. Avoiding coffee ring structure based on hydrophobic silicon pillar arrays during single-drop evaporation. *Soft Matter*, 8(40):10448–10456, 2012.

[104] Rui Dou and Brian Derby. Formation of coffee stains on porous surfaces. *Langmuir*, 28(12):5331–5338, 2012.

[105] Dan Soltman and Vivek Subramanian. Inkjet-printed line morphologies and temperature control of the coffee ring effect. *Langmuir*, 24(5):2224–2231, 2008.

[106] Kara L. Maki and Satish Kumar. Fast evaporation of spreading droplets of colloidal suspensions. *Langmuir*, 27(18):11347–11363, 2011.

[107] Xiaoying Shen, Chih-Ming Ho, and Tak-Sing Wong. Minimal size of coffee ring structure. *Journal of Physical Chemistry B*, 114(16):5269–5274, 2010.

[108] H. Hu and R. G. Larson. Marangoni effect reverses coffee-ring depositions. *Journal of Physical Chemistry B*, 110(14):7090–7094, 2006.

[109] Joshua R. Trantum, Zachary E. Eagleton, Chetan A. Patil, Jason M. Tucker-Schwartz, Mark L. Baglia, Melissa C. Skala, and Frederick R. Haselton. Cross-sectional tracking of particle motion in evaporating drops: flow fields and interfacial accumulation. *Langmuir*, 29(21):6221–6231, 2013.

[110] Andrew C. Ihnen, Anne M. Petrock, Tsengming Chou, Brian E. Fuchs, and Woo Y. Lee. Organic nanocomposite structure tailored by controlling droplet

coalescence during inkjet printing. *ACS Applied Materials & Interfaces*, 4(9):4691–4699, 2012.

[111] Michael Layani, Michael Grouchko, Shai Shemesh, and Shlomo Magdassi. Conductive patterns on plastic substrates by sequential inkjet printing of silver nanoparticles and electrolyte sintering solutions. *Journal of Materials Chemistry*, 22(29):14349–14352, 2012.

[112] Venkateshwar Rao Dugyala, Santosh V. Daware, and Madivala G. Basavaraj. Shape anisotropic colloids: synthesis, packing behavior, evaporation driven assembly, and their application in emulsion stabilization. *Soft Matter*, 9(29):6711–6725, 2013.

[113] S. Magdassi, M. Grouchko, D. Toker, A. Kamyshny, I. Balberg, and O. Millo. Ring stain effect at room temperature in silver nanoparticles yields high electrical conductivity. *Langmuir*, 21(23):10264–10267, 2005.

[114] Alvaro G. Marin, Hanneke Gelderblom, Detlef Lohse, and Jacco H. Snoeijer. Order-to-disorder transition in ring-shaped colloidal stains. *Physical Review Letters*, 107(8):085502, 2011.

[115] Tak-Sing Wong, Ting-Hsuan Chen, Xiaoying Shen, and Chih-Ming Ho. Nanochromatography driven by the coffee ring effect. *Analytical Chemistry*, 83(6):1871–1873, 2011.

[116] Viral H. Chhasatia and Ying Sun. Interaction of bi-dispersed particles with contact line in an evaporating colloidal drop. *Soft Matter*, 7(21):10135–10143, 2011.

[117] Jayakrishna Khatei and K. S. R. Koteswara Rao. Hydrothermal synthesis of CdTe QDs: their luminescence quenching in the presence of bio-molecules and

observation of bistable memory effect in CdTe QD/PEDOT:PSS heterostructure. *Materials Chemistry and Physics*, 130(1-2):159–164, 2011.

[118] Erkan Senses, Matthew Black, Thomas Cunningham, Svetlana A. Sukhishvili, and Pinar Akcora. Spatial ordering of colloids in a drying aqueous polymer droplet. *Langmuir*, 29(8):2588–2594, 2013.

[119] G. A. Buxton and N. Clarke. Ordering polymer blend morphologies via solvent evaporation. *Europhysics Letters*, 78(5):56006, 2007.

[120] E. M. Foard and A. J. Wagner. Enslaved phase-separation fronts in one-dimensional binary mixtures. *Physical Review E*, 79(5):056710, 2009.

[121] E. M. Foard and A. J. Wagner. Enslaved phase-separation fronts and Liesegang pattern formation. *Communications in Computational Physics*, 9(5):1081–1093, 2011.

[122] E. M. Foard and A. J. Wagner. Survey of morphologies formed in the wake of an enslaved phase-separation front in two dimensions. *Physical Review E*, 85(1):011501, 2012.

[123] S. Ramakrishnan, M. Fuchs, K. S. Schweizer, and C. F. Zukoski. Concentration fluctuations in a model colloid-polymer suspension: experimental tests of depletion theories. *Langmuir*, 18(4):1082–1090, 2002.

[124] J. B. Miller and E. K. Hobbie. Phase separation and the 'coffee-ring' effect in polymer-nanocrystal mixtures. *Soft Matter*, 10(11):1665–1675, 2014.

[125] Sho Asakura and Fumio Oosawa. On interaction between two bodies immersed in a solution of macromolecules. *Journal of Chemical Physics*, 22:1255–1256, 1954.

[126] A. Vrig. Polymers at interfaces and the interactions in colloidal dispersions. *Pure and Applied Chemistry*, 48(4):471–483, 1976.

[127] M. Schmidt and M. Fuchs. Penetrability in model colloid-polymer mixtures. *Journal of Chemical Physics*, 117(13):6308–6312, 2002.

[128] H. N. W. Lekkerkerker, W. C. K. Poon, P. N. Pusey, A. Stroobants, and P. B. Warren. Phase-behavior of colloid plus polymer mixtures. *Europhysics Letters*, 20(6):559–564, 1992.

[129] L. Mangolini, E. Thimsen, and U. Kortshagen. High-yield plasma synthesis of luminescent silicon nanocrystals. *Nano Letters*, 5(4):655–659, 2005.

[130] Hyun Suk Kim, Cheol Hee Lee, P. K. Sudeep, Todd Emrick, and Alfred J. Crosby. Nanoparticle stripes, grids, and ribbons produced by flow coating. *Advanced Materials*, 22(41):4600–4604, 2010.

[131] Folarin Erogbogbo, Ken-Tye Yong, Indrajit Roy, Rui Hu, Wing-Cheung Law, Weiwei Zhao, Hong Ding, Fang Wu, Rajiv Kumar, Mark T. Swihart, and Paras N. Prasad. In vivo targeted cancer imaging, sentinel lymph node mapping and multi-channel imaging with biocompatible silicon nanocrystals. *ACS Nano*, 5(1):413–423, 2011.

[132] Folarin Erogbogbo, Ken-Tye Yong, Indrajit Roy, GaiXia Xu, Paras N. Prasad, and Mark T. Swihart. Biocompatible luminescent silicon quantum dots for imaging of cancer cells. *ACS Nano*, 2(5):873–878, 2008.

[133] P. Alivisatos. The use of nanocrystals in biological detection. *Nature Biotechnology*, 22(1):47–52, 2004.

[134] Norah O'Farrell, Andrew Houlton, and Benjamin R. Horrocks. Silicon nanoparticles: applications in cell biology and medicine. *International Journal of Nanomedicine*, 1(4):451–472, 2006.

[135] Ji-Ho Park, Luo Gu, Geoffrey von Maltzahn, Erkki Ruoslahti, Sangeeta N. Bhatia, and Michael J. Sailor. Biodegradable luminescent porous silicon nanoparticles for in vivo applications. *Nature Materials*, 8(4):331–336, 2009.

[136] A. Luque and A. Marti. Increasing the efficiency of ideal solar cells by photon induced transitions at intermediate levels. *Physical Review Letters*, 78(26):5014–5017, 1997.

[137] E. V. Shevchenko, D. V. Talapin, C. B. Murray, and S. O'Brien. Structural characterization of self-assembled multifunctional binary nanoparticle superlattices. *Journal of the American Chemical Society*, 128(11):3620–3637, 2006.

[138] Zhuoying Chen and Stephen O'Brien. Structure direction of II-VI semiconductor quantum dot binary nanoparticle superlattices by tuning radius ratio. *ACS Nano*, 2(6):1219–1229, 2008.

[139] Wiel H. Evers, Bart De Nijs, Laura Filion, Sonja Castillo, Marjolein Dijkstra, and Daniel Vanmaekelbergh. Entropy-driven formation of binary semiconductor-nanocrystal superlattices. *Nano Letters*, 10(10):4235–4241, 2010.

[140] E. Rabani. An interatomic pair potential for cadmium selenide. *Journal of Chemical Physics*, 116(1):258–262, 2002.

[141] Niels Tas, Tonny Sonnenberg, Henri Jansen, Rob Legtenberg, and Miko Elwenspoek. Stiction in surface micromachining. *Journal of Micromechanics and Microengineering*, 6(4):385–397, 1996.

[142] Eric R. Dufresne. pkfnd, cntrd, 2005.

[143] John C. Crocker. track.pro, 1999.

APPENDIX A. LINEAR CORRELATION FITS

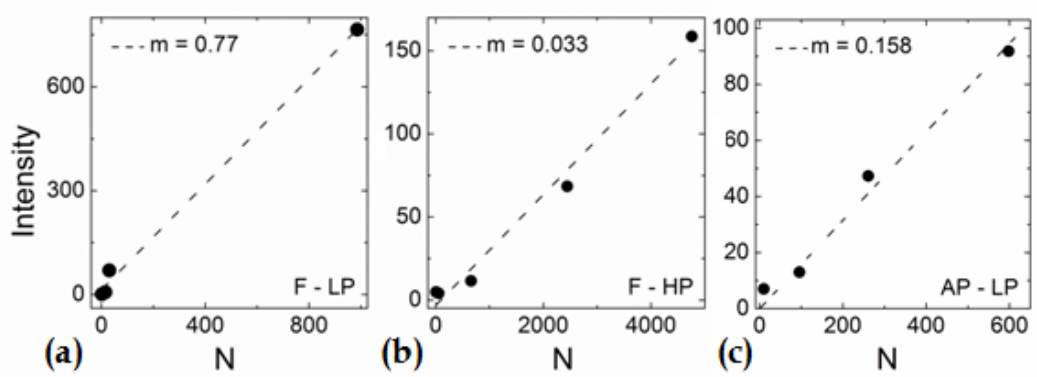

Calibration curves for calculation of cluster size for (a) the fraction at low power, (b) the fraction at high power, and (c) the AP material at low power.

APPENDIX B. MATLAB BLINKING CODE

Some of this Matlab code contains modified programs from [142, 143].

```
PARTICLE TRACKING


fname = '2012 November 21 spot1Corrected.tif';
%info = iminfo(fname);
out = 0;
time = 0.0;
dt = 0.1;
counter = 1;
num_images = 6000;
stdev = 19.932;%17.4,18.5,18.2
for k = 1:num_images
    A = imread(fname, k);
    aa = double(A);
    pk = pkfnd2(aa,stdev*1.3*9,2);%*9 & 2 for small
    cnt=cntrd(aa,pk,2.3333);%2.3333 for small
    nop=size(cnt);
    numberofparticles=nop(1);
    for l = 1:numberofparticles
    out(counter,4) = time;
    out(counter,1) = cnt(l,1);
    out(counter,2) = cnt(l,2);
    out(counter,3) = cnt(l,3);
    counter = counter + 1;
    end
    time = time + dt;
```

```
end


param.mem=6000;

param.dim=2;

param.good=1;

param.quiet=1;

particles=track2(out,1.5,param);%1.5 for small



BLINKS


fitmult = 0.1576;

clusterbins = [1,2,3,4,5,6,8,12,20,40,100,500,1000];

clusterbinsnumber = length(clusterbins);

blinking=particles();

clustersid=blinking(:,5);

clusterstime=blinking(:,4);

clustersint=blinking(:,3);

clusternumber=max(clustersid);

data=length(clustersid);

numberimages = num_images;

ontimes=[];

offtimes=[];

intavemax=[];

bintime=dt;

maxtime = numberimages*bintime-bintime;

maxtime2 = maxtime + bintime;

counter=0;
```

```
totalontime = [];


for s = 1:clusternumber
    idtimes=[];
    maxint = 0;
    totalint = 0;
    clustint = [];
    counter=0;
    intensityave = 0;
    calcclustsize = 0;
    totontime = 0;
    ontimecounter = bintime;
    for i = 1:data
        if clustersid(i)== s
            counter = counter +1;
            totontime = totontime + 0.1;
            idtimes = [idtimes,clusterstime(i)];
            clustint = [clustint,clustersint(i)];
        end
    end
    maxint = max(clustint);
    intensityave = sum(clustint)/numberimages;
    calcclustsize = intensityave/fitmult;
    if counter == 1
        ontimes = [ontimes,[bintime,calcclustsize]'];
        if idtimes(1) < bintime*.9 || idtimes(1) > maxtime-bintime*.1
            offtimes = [offtimes,[maxtime,calcclustsize]'];
        else
```

```
        time2 = maxtime - idtimes(1);
        offtimes = [offtimes,[time2,calcclustsize]'];
        offtimes = [offtimes,[idtimes(1),calcclustsize]'];
    end
else
    for q = counter:-1:2
        if idtimes(q)-idtimes(q-1) < bintime*1.1
            ontimecounter = ontimecounter + bintime;
            if q == counter && idtimes(q) < maxtime - bintime*.1
                offtimes = [offtimes,[maxtime-idtimes(q),calcclustsize
                    ]'];
            end
            if q == 2
                ontimes = [ontimes,[ontimecounter,calcclustsize]'];
                if idtimes(q-1) > bintime*.9
                    offtimes = [offtimes,[idtimes(q-1),calcclustsize]'];
                end
            end
        else
            if q == 2
                ontimes = [ontimes,[bintime,calcclustsize]'];
                if idtimes(q-1) > bintime*.9
                    offtimes = [offtimes,[idtimes(q-1),calcclustsize]'];
                end
            end
            if q == counter && idtimes(q) < maxtime - bintime*.1
                offtimes = [offtimes,[maxtime-idtimes(q),calcclustsize
                    ]'];
```

```
                end
                offtimes = [offtimes,[idtimes(q)-idtimes(q-1)-bintime,
                    calcclustsize]'];
                ontimes = [ontimes,[ontimecounter,calcclustsize]'];
                ontimecounter = bintime;
            end
        end
    end
    intavemax = [intavemax,[intensityave,maxint,s]'];
    totalontime = [totalontime,[calcclustsize,totontime,s]'];
end

totalontime = totalontime';
intavemax = intavemax';
averageintensities = intavemax(:,1);
clustersize = averageintensities/fitmult;
clusterSizeIntMaxId = [clustersize,intavemax];

ontimes = ontimes';
offtimes = offtimes';
maxontime = max(ontimes(:,1));
maxofftime = max(offtimes(:,1));
BinnedOnTimes = [];
BinnedOffTimes = [];
spreadsheetcounter = 0;

for i = 1:clusterbinsnumber+1
    marker = 0;
```

```
    for l = 1:length(clusterSizeIntMaxId)
        if i == 1
            if clusterSizeIntMaxId(l,1) < clusterbins(1)
                marker = marker + 1;
                ClusterSizeBinId(marker,i) = clusterSizeIntMaxId(l,4);
            end
        elseif i == clusterbinsnumber+1
            if clusterSizeIntMaxId(l,1) >= clusterbins(i-1)
                marker = marker + 1;
                ClusterSizeBinId(marker,i) = clusterSizeIntMaxId(l,4);
            end
        else
            if clusterSizeIntMaxId(l,1) < clusterbins(i) &
                clusterSizeIntMaxId(l,1) >= clusterbins(i-1)
                marker = marker + 1;
                ClusterSizeBinId(marker,i) = clusterSizeIntMaxId(l,4);
            end
        end
    end
end

ClusterSizeBinACF = zeros(6000,clusternumber,length(ClusterSizeBinId(1,:)))
    ;

for i = 1:length(ClusterSizeBinId(1,:))
    if length(nonzeros(ClusterSizeBinId(:,i))) == 0
    else
    for j = 1:length(nonzeros(ClusterSizeBinId(:,i)))
```

```
            for m = 1:length(blinking)
                if ClusterSizeBinId(j,i) == blinking(m,5)
                    blinktime = blinking(m,4)*10 + 1;
                    blinkingtime = round(blinktime);
                    ClusterSizeBinACF(blinkingtime,j,i)= blinking(m,3);
                end
            end
            %for n = 1:6000
            %    if ClusterSizeBinACF(n,j,i) == 0
            %        ClusterSizeBinACF(n,j,i) = normrnd(0,15);
            %    end
            %end

            BinnedACF(:,j,i) = acf2(ClusterSizeBinACF(:,j,i),5990);
    end
    for p = 1:length(BinnedACF(:,j,i))
         AveClusterSizeBinACF(p,i) = mean(BinnedACF(p,1:j,i));
    end
%     for p = 1:length(BinnedACF(:,j,i))
%          AveClusterSizeBinBeforeACF(p,i) = mean(ClusterSizeBinACF(p,1:j,i)
    );
%     end
    end
end



for i = 1:clusterbinsnumber+1
    marker = 0;
```

```
    for l = 1:length(clusterSizeIntMaxId)
        if i == 1
            if clusterSizeIntMaxId(l,2) < clusterbins(1)
                marker = marker + 1;
                clustSizeIntMaxId(marker,i) = clusterSizeIntMaxId(l,1);
            end
        elseif i == clusterbinsnumber+1
            if clusterSizeIntMaxId(l,2) >= clusterbins(i-1)
                marker = marker + 1;
                on(marker,i) = clusterSizeIntMaxId(l,1);
            end
        else
            if clusterSizeIntMaxId(l,2) < clusterbins(i) &
                clusterSizeIntMaxId(l,2) >= clusterbins(i-1)
                marker = marker + 1;
                on(marker,i) = clusterSizeIntMaxId(l,1);
            end
        end
    end
end


on = [];
off = [];
for i = 1:clusterbinsnumber+1
    marker = 0;
    for l = 1:length(ontimes)
        if i == 1
            if ontimes(l,2) < clusterbins(1)
```

```
                marker = marker + 1;
                on(marker,i) = ontimes(l,1);
            end
        elseif i == clusterbinsnumber+1
            if ontimes(l,2) >= clusterbins(i-1)
                marker = marker + 1;
                on(marker,i) = ontimes(l,1);
            end
        else
            if ontimes(l,2) < clusterbins(i) & ontimes(l,2) >= clusterbins(i
                -1)
                marker = marker + 1;
                on(marker,i) = ontimes(l,1);
            end
        end
    end
end

for i = 1:clusterbinsnumber+1
    marker = 0;
    for l = 1:length(offtimes)
        if i == 1
            if offtimes(l,2) < clusterbins(1)
                marker = marker + 1;
                off(marker,i) = offtimes(l,1);
            end
        elseif i == clusterbinsnumber+1
            if offtimes(l,2) >= clusterbins(i-1)
```

```
                marker = marker + 1;
                off(marker,i) = offtimes(l,1);
            end
        else
            if offtimes(l,2) < clusterbins(i) & offtimes(l,2) >= clusterbins
                (i-1)
                marker = marker + 1;
                off(marker,i) = offtimes(l,1);
            end
        end
    end
end
%}


BLINKS2

for i = 1:clusterbinsnumber+1
    marker = 0;
    for l = 1:length(clusterSizeIntMaxId)
        if i == 1
            if clusterSizeIntMaxId(l,1) < clusterbins(1)
                marker = marker + 1;
                ClusterSizeBinInt(marker,i) = clusterSizeIntMaxId(l,2);
            end
        elseif i == clusterbinsnumber+1
            if clusterSizeIntMaxId(l,1) >= clusterbins(i-1)
                marker = marker + 1;
```

```
                ClusterSizeBinInt(marker,i) = clusterSizeIntMaxId(l,2);
            end
        else
            if clusterSizeIntMaxId(l,1) < clusterbins(i) &&
                clusterSizeIntMaxId(l,1) >= clusterbins(i-1)
                marker = marker + 1;
                ClusterSizeBinInt(marker,i) = clusterSizeIntMaxId(l,2);
            end
        end
    end
end


for i = 1:clusterbinsnumber+1
    marker = 0;
    for l = 1:length(ontimes)
        if i == 1
            if ontimes(l,2) < clusterbins(1)
                marker = marker + 1;
                ClusterSizeBinOn(marker,i) = ontimes(l,1);
            end
        elseif i == clusterbinsnumber+1
            if ontimes(l,2) >= clusterbins(i-1)
                marker = marker + 1;
                ClusterSizeBinOn(marker,i) = ontimes(l,1);
            end
        else
            if ontimes(l,2) < clusterbins(i) & ontimes(l,2) >= clusterbins(i
                -1)
```

```
                marker = marker + 1;
                ClusterSizeBinOn(marker,i) = ontimes(l,1);
            end
        end
    end
end

for i = 1:clusterbinsnumber+1
    marker = 0;
    for l = 1:length(offtimes)
        if i == 1
            if offtimes(l,2) < clusterbins(1)
                marker = marker + 1;
                ClusterSizeBinOff(marker,i) = offtimes(l,1);
            end
        elseif i == clusterbinsnumber+1
            if offtimes(l,2) >= clusterbins(i-1)
                marker = marker + 1;
                ClusterSizeBinOff(marker,i) = offtimes(l,1);
            end
        else
            if offtimes(l,2) < clusterbins(i) & offtimes(l,2) >= clusterbins
                (i-1)
                marker = marker + 1;
                ClusterSizeBinOff(marker,i) = offtimes(l,1);
            end
        end
    end
```

```
end


for ff = 1:length(ClusterSizeBinOn(1,:))
    spreadsheetcounter = 0;
    for i = 0.1:0.1:maxontime
        spreadsheetcounter = spreadsheetcounter + 1;
        bincounter = 0;
        for k = 1:length(ClusterSizeBinOn)
            if ClusterSizeBinOn(k,ff)>i-.001 & ClusterSizeBinOn(k,ff)<i+.001
            bincounter = bincounter + 1;
            end
        end
        BinnedOnTimes(spreadsheetcounter,1,ff) = i;
        BinnedOnTimes(spreadsheetcounter,2,ff) = bincounter;
    end
    spreadsheetcounter = 0;
    for i = 0.1:0.1:maxontime
        spreadsheetcounter = spreadsheetcounter + 1;
        BinnedOnTimes(spreadsheetcounter,3,ff) = BinnedOnTimes(
            spreadsheetcounter,2,ff)/max(BinnedOnTimes(:,2,ff));
    end
    BinnedOnTimes(1,4,ff)=sum(ClusterSizeBinOn(:,ff))/length(nonzeros(
        ClusterSizeBinOn(:,ff)));
    BinnedOnTimes(1,5,ff)=max(ClusterSizeBinOn(:,ff));
    BinnedOnTimes(1,6,ff)=sum(ClusterSizeBinOn(:,ff))/(length(nonzeros(
        ClusterSizeBinId(:,ff)))*maxtime2);
end
```

```
for ff = 1:length(ClusterSizeBinOff(1,:))
    spreadsheetcounter = 0;
    for i = 0.1:0.1:maxofftime
        spreadsheetcounter = spreadsheetcounter + 1;
        bincounter = 0;
        for k = 1:length(ClusterSizeBinOff)
            if ClusterSizeBinOff(k,ff)>i-.001 & ClusterSizeBinOff(k,ff)<i
                +.001
            bincounter = bincounter + 1;
            end
        end
        BinnedOffTimes(spreadsheetcounter,1,ff) = i;
        BinnedOffTimes(spreadsheetcounter,2,ff) = bincounter;
    end
    spreadsheetcounter = 0;
    for i = 0.1:0.1:maxofftime
        spreadsheetcounter = spreadsheetcounter + 1;
        BinnedOffTimes(spreadsheetcounter,3,ff) = BinnedOffTimes(
            spreadsheetcounter,2,ff)/max(BinnedOffTimes(:,2,ff));
    end
    BinnedOffTimes(1,4,ff)=sum(ClusterSizeBinOff(:,ff))/length(nonzeros(
        ClusterSizeBinOff(:,ff)));
    BinnedOffTimes(1,5,ff)=max(ClusterSizeBinOff(:,ff));
    BinnedOffTimes(1,6,ff)=sum(ClusterSizeBinOff(:,ff))/(length(nonzeros(
        ClusterSizeBinId(:,ff)))*maxtime2);
end


spreadsheetcounter=0;
```

```
spreadsheetcounter2=0;


for i = 0.1:0.1:maxontime
    spreadsheetcounter = spreadsheetcounter + 1;
    bincounter = 0;
    for k = 1:length(ontimes)
        if ontimes(k,1)>i-.001 & ontimes(k,1)<i+.001
            bincounter = bincounter + 1;
        end
    end
    AllOnTimes(spreadsheetcounter,1) = i;
    AllOnTimes(spreadsheetcounter,2) = bincounter;
    AllOnTimes(spreadsheetcounter,3) = AllOnTimes(spreadsheetcounter,2)/
        AllOnTimes(1,2);
end


for i = 0.1:0.1:maxofftime
    spreadsheetcounter2 = spreadsheetcounter2 + 1;
    bincounter = 0;
    for k = 1:length(offtimes)
        if offtimes(k,1)>i-.001 & offtimes(k,1)<i+.001
            bincounter = bincounter + 1;
        end
    end
    AllOffTimes(spreadsheetcounter2,1) = i;
    AllOffTimes(spreadsheetcounter2,2) = bincounter;
    AllOffTimes(spreadsheetcounter2,3) = AllOffTimes(spreadsheetcounter2,2)
        /AllOffTimes(1,2);
```

```
end



bboff=[];
bboffprob=[];
bbonprob=[];
bbon=[];
for i = 1:length(BinnedOffTimes(1,1,:))
    bboff(:,i)=BinnedOffTimes(:,2,i);
end
for i = 1:length(BinnedOffTimes(1,1,:))
    bboffprob(:,i)=BinnedOffTimes(:,3,i);
end
for i = 1:length(BinnedOnTimes(1,1,:))
    bbon(:,i)=BinnedOnTimes(:,2,i);
end
for i = 1:length(BinnedOnTimes(1,1,:))
    bbonprob(:,i)=BinnedOnTimes(:,3,i);
end



bbbon=[];
bbboff=[];
for i = 1: length(BinnedOffTimes(1,1,:))
    bbboff(:,i)=BinnedOffTimes(1,4:6,i);
end
bbboff=bbboff';
for i = 1: length(BinnedOnTimes(1,1,:))
```

```
    bbbon(:,i)=BinnedOnTimes(1,4:6,i);
end
bbbon=bbbon';



for i = 1: length(BinnedOnTimes(1,1,:))
    AveIntegratedInt(i)=numberimages*(sum(ClusterSizeBinInt(:,i)))/length(
        nonzeros(ClusterSizeBinInt(:,i)));
end
AveIntegratedInt=AveIntegratedInt';
```